Exploration of Metal 3-D Printing Technologies for the Microfabrication of Freeform, Finely Featured, Mesoscaled Structures

by

Zhumei Sun

M. E., Optical Engineering, Shanghai Institute of Optics and Fine Mechanics, Chinese Academy of Sciences, China (2016)

B.E., Test Control Technique and Instrument, Beijing Institute of Technology, China (2013)

SUBMITTED TO THE DEPARTMENT OF MECHANICAL ENGINEERING IN PARTIAL FULFILLMENT OF THE REQUIREMENTS FOR THE DEGREE OF

MASTER OF SCIENCE IN MECHANICAL ENGINEERING

AT THE

MASSACHUSETTS INSTITUTE OF TECHNOLOGY

JUNE 2018

Signature of Author: **Signature redacted**

Department of Mechanical Engineering
May 10, 2018

Certified by: **Signature redacted**

Luis Fernando Velásquez-García
Principal Research Scientist, Microsystems Technology Laboratories
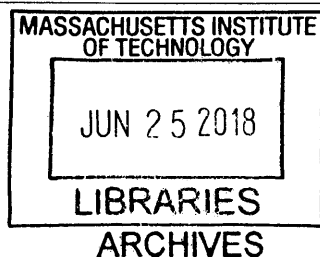Thesis Supervisor

Certified by: **Signature redacted**

Anastasios John Hart
Associate Professor, Department of Mechanical Engineering
Thesis Reader

Accepted by: **Signature redacted**

Rohan Abeyaratne
Quentin Berg Professor of Mechanics
Chairman, Committee on Graduate Students

Exploration of Metal 3-D Printing Technologies for the Microfabrication of Freeform, Finely Featured, Mesoscaled Structures

by

Zhumei Sun

Abstract

This thesis investigates a mainstream metal 3-D printing technique (i.e., direct metal laser sintering of stainless steel {SS} 316L) and two relatively new metal additive manufacturing methods (i.e., lost-wax casting of sterling silver using stereolithography-printed wax masters, and binder inkjet printing of SS 316L) for the fabrication, using tens-of-microns sized voxels, of freeform, finely featured, mesoscaled metal structures part of compact systems. Characterization of the 3-D printing methods includes the assessment of dimensional accuracy and in-plane minimum feature size, measurement of vacuum outgassing and porosity, and estimation of thermal and electrical properties of the printed parts. The data demonstrate that binder inkjet printing of SS 316L has associated the smallest in-plane offset, out-of-plane offset, and eccentricity of nominally symmetric features, while showing ultra-high-vacuum compatibility and intrinsic electrical and thermal properties close to those of bulk metal. Characterization of binder inkjet-printed SS 316L MEMS cantilevers shows repeatable micron-level linear actuation and a near-isotropic Young's modulus of the printed material close to the bulk value. Also, current-voltage characteristics in air of binder inkjet-printed SS 316L MEMS corona discharge ionizers with high aspect-ratio tips are presented. In addition, high-resolution microscopy of binder inkjet-printed SS 316L electrodes part of a novel, compact, multi-electrode harmonized Kingdon mass trap estimates at ~15 μm the maximum height difference between the printed part and the digital model.

Acknowledgements

Contents

List of Figures

List of tables

1. Introduction

Additive manufacturing (AM) is a relatively new set of bottom-up fabrication techniques for layer-by-layer buildup of three-dimensional (3D) solid objects of virtually any geometry described by a computer-aided design (CAD) model [1]–[3]. AM has recently received great attention because of its unique advantages over traditional manufacturing. In contrast to traditional fabrication methods that feature the removal of material by cutting or drilling, AM is a bottom-up approach that builds up objects by adding material in a layer-by-layer manner [2], bringing with it an array of desirable features including fast design iteration, compatibility with freeform geometries impossible or challenging to build by conventional methods, print-to-print design customization, and substantial reduction of cost and waste. An example of this is the Advanced Turboprop engine (ATP) GE currently in development: 855 parts were reduced to 12 and the new process eliminated structural castings (though some casting is still required); the ATP has 20% less fuel consumption, 5% weight reduction, and the test schedule was reduced from 12 to 6 months [4].

For microsystems, AM benefits include the realization of designs that are difficult, impractical, or unfeasible to make with standard microfabrication methods, e.g., monolithic multilevel microfluidics [5]–[7]. The research on metal AM for microsystems has focused on electrical interconnects; explored approaches include nanoparticle ink coating [8], laser-assisted electrophoretic deposition [9], meniscus confined electroplating [10], electrohydrodynamic printing [11], focused electron/ion beam-induced deposition [12], and microplasma sputtering [13]. Although these methods can print layers with electrical conductivity within an order of magnitude of bulk values [14], they have not been shown to reproduce freeform three-dimensional objects with high fidelity, or be practical for implementing mesoscaled [15] components of interest to microsystems, e.g., structures of arbitrary shape with tens-of-microns to sub-millimeter characteristic dimensions and total dimensions between hundreds of microns to centimeters. Examples of these structures include packages [16], mm-wave vacuum amplifiers and THz wave generators [17], [18], mass filter electrodes [19], high-temperature microfluidics [20], needles for tissue interaction [21], [22], ionic wind pumps [23], and low-frequency vibration energy harvesters [24]. These metal structures are typically microfabricated via LIGA [25] (a low-throughput fabrication technique based on electroplating molds patterned with x-ray lithography), electrical discharge machining (EDM, a low-throughput, power-intensive etch process based on microdischarges), wafer bonding [26], or are not microfabricated (e.g., dowel pins have been used as electrodes in MEMS quadrupole mass filters [19], [27]).

The AM processes capable of creating freeform, mesoscaled metal components are commonly classified into powder bed fusion (PBF) [28]–[32], direct energy deposition (DED) [33]–[35], binder jetting [36], [37] and sheet lamination [38], [39] as stated in ASTM ISO/ASTM 52900 [40]; among these methods,

PBF and DED are the most widely implemented [41]. In PBF, layers of metal powders are fused by raster scanning a heat source, laser (named as direct metal laser sintering {DMLS}) or electron beam (referred to as electron beam melting {EBM}) [42], [43]; re-melting of previous layers during the melting of the current layer is necessitated to fuse a solid part, potentially altering the geometry being printed compared to the CAD model. DED relies on melting the substrate and simultaneously the feedstock being deposited into the substrate melt pool with a focused heat source, typically laser or electron beam; the typical layer thickness employed in DED is in the range of 0.25-1mm [44], [45], which implies that this method is incapable of directly producing mesoscale components with high precision. Building 3D components via sheet lamination involves precisely stacking machined metal sheets followed by joining them with adhesives or via metal bonding [46]. Requirement of massive fine feature machining and anisotropic properties of final parts are inherent limiting factors, besides, complex overhangs are unfeasible to manufacture [2].

In this thesis, we investigate a mainstream metal printing technique (i.e., DMLS of stainless steel {SS} 316L) and two relatively new metal AM methods (i.e., lost-wax casting of sterling silver using stereolithography {SLA}-printed masters [47], and binder inkjet-printing of SS 316L [48]) for the fabrication, using tens-of-microns-sized voxels, of freeform, finely featured, mesoscaled metal structures. Chapter 2 describes the different 3D printing technologies and the fabrication of the samples used in this investigation. Chapter 3 summarizes the characterization methods used in this work. Chapter 4 reports the characterization of the printed samples including (i) resolution, repeatability, and minimum feature size, (ii) vacuum outgassing, (iii) thermal conductivity and electrical resistance, (iv) microstructure morphology, surface roughness, and porosity, and (v) elastic properties. The data demonstrate that binder inkjet-printing of SS 316L outperforms the other two printing technologies in most of the metrics analyzed, generating printed material with intrinsic physical properties close to those of the bulk metal. Chapter 5, reports the fabrication and characterization of two examples of binder inkjet-printed SS 316L mesoscaled structures: MEMS corona discharge ionizer arrays, and electrodes part of a novel, compact, multielectrode harmonized Kingdon ion trap for mass spectrometry applications. Finally, Chapter 6 summarizes the work, and Chapter 7 proposes directions for future work.

2. 3D Printing Technologies and Specimen Fabrication

In this study, three metal AM methods were investigated: DMLS of SS 316L, lost-wax casting of sterling silver using SLA-printed masters, and binder inkjet-printing of SS 316L. In this chapter, we first explain in detail the AM methods, and then describe the fabrication of the specimens used in this research.

2.1. Direct metal laser sintering

The DMLS process creates objects from a variety of powder materials by locally heating particles with a laser, followed by fusing or melting them together near the surface, layer by layer, in an inert-gas protective chamber [40]. The first DMLS system was developed by Carl Deckard in 1986 and commercialized by DTM Corporation in 1992 [49]. Introduced in 1995 by company EOS GmbH from Germany, the machine EOSINT M250 was the first bronze-based metal powder printer that could print 100 μm-thick layers using a carbon dioxide laser [50]; an updated version in 1997 enabled printing with 50 μm-thick layers. In the late 1998 the first iron-based powder DMLS printer Directsteel 50-V1 was introduced, capable of printing objects using 50 μm-thick layers; this version was soon modified to the DirectSteel 20-V1 with 20 μm-thick layer capability. In 2004, EOS GmbH presented the EOSINT M 270 and a new series of powder named DirectSteel H20, which were claimed to print parts with properties comparable with commonly-used tool steels [51]. In addition, selective laser melting (SLM) systems that completely melt the powders and use pure metal feedstock were developed by Fockele and Schwarze (F&S) in cooperation with the Fraunhofer Institute of Laser Technology in 1999 [52]–[54] and commercialized as the MCP Realizer250 machine by MCP HEK GmbH (now SLM Solutions GmbH) in 2004 [55]. State-of-the-art DMLS systems are operated at power in the range of 100-1000W, sufficient to fully melt powders, and in practice SLM and DMLS denominations are currently used interchangeably [56].

Figure 1 shows a schematic diagram of a DMLS setup [37], in which mirrors are used to direct the laser beam on the powder bed and control the movement of the laser beam spot in planar directions (XY-direction) following the designed path. The printing process starts by spreading a thin layer of metal particles on the platform; then, a laser scans the surface of the platform while fusing/melting the metallic powder in certain areas of the powder bed; once solidified, the laser-treated areas become the newest layer of the build. Afterwards, the platform moves down, and a recoating blade or brush pushes another layer of fresh powder from the powder tank to the top of the previously built surface, and the laser scan process repeats. At the end of the build process, the un-melted powder is removed to reveal the workpiece and sieved back for reuse.
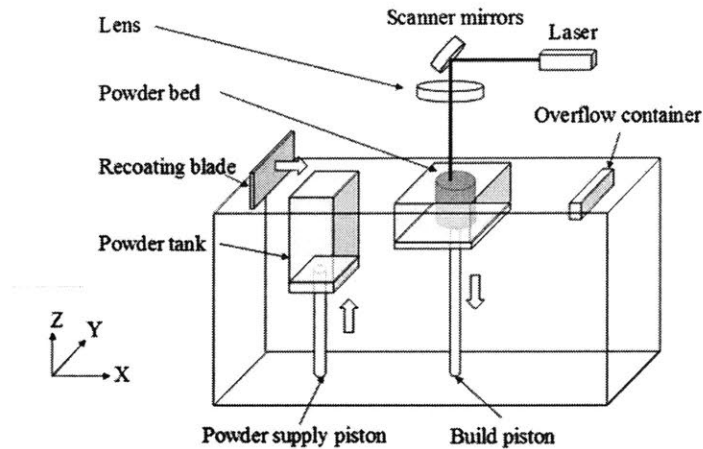
Figure 1 Schematic of a direct metal laser sintering setup [37].

In DMLS the building chamber is filled with inert gas, typically argon or nitrogen, to avoid oxidization of metallic powders at high temperatures. The complicated thermal history the material experiences during the printing process, i.e., the sequential consolidation of the material in small segments, induces a complex thermal cycle that includes directed heat input and heat extraction and repeated partial re-melting and cooling down, leading to accumulated residual stress –posing a detrimental effect on geometrical precision and mechanical strength. Therefore, a DMLS-fabricated part exhibits heterogeneous microstructure due to the preferred directional grain growth as the heat is extracted directionally [57], resulting in mechanical anisotropy in the out-of-plane direction (Z-direction) generally being the weakest. Regarding the roughness, DMLS parts are composed of a number of molten pools after solidification, and the surface morphology can be described as overlapping peaks and valleys [58]. Moreover, considering the capillary forces in the molten pool, the unmelted particles adsorbed on the surface during the cooling process are prone to create micro-porosity and generate rough surface finish, which limit the consistence of the produced parts. Furthermore, the absorption by the molten pool of N_2, O_2, and H_2, as well as the entrapment of the gas used in the inert atmosphere nucleate bubbles at the solid-liquid interface during solidification, leading to additional porosity in the DMLS parts [59]. Based on the description of the printing process, the main printing factors that affect the structural and mechanical properties of fabricated parts are (i) laser energy density, (ii) platform temperature [60], (iii) layer thickness [61], (iv) hatch distance [62], and (v) composition and pressure of the sintering atmosphere [63]. For example, a higher laser scan speed results in less energy being transferred to the materials, leading to insufficient sintering and more porosity [64]. Parts densification could be achieved by decreasing the laser scanning speed, lengthening the interaction time between the powder and the laser beam, boosting the amount of energy delivered to the powder bed.

As a result, the mechanical properties of the final parts could be strengthened in general, but the final dimensions of the printed part might be inaccurate [65]. Layer thickness, determined by the maximum particle size of the powder, is another factor influencing the pore size: a thinner powder layer allows sufficient fusion between particles, resulting in more densification and lower open porosity [66]; however, if a too-small layer thickness is chosen, the blade will drag non-melted large particles or chunks of melted particles, displacing the previous sintered layers from their position. As a matter of fact, the issues posed by the special and complex metallurgy conditions during the DMLS process (e.g. overlapping of the melt pools, layer-by-layer stacking, and extreme temperature gradients) are yet to be resolved, and understanding the DMLS printing process is still an ongoing research effort.

2.2. Lost-wax microcasting

Lost-wax casting –a sculpting technique dating back to the Chalcolithic period [67], is a method for producing high-quality metal components with excellent surface finish, dimensional accuracy and complex shapes. Lost-wax casting is especially useful for producing complicatedly metal parts with undercuts or geometry that could not be forged or machined (or machining would be material wasteful). Another advantage of the lost-wax casting process over other shaping processes is the low loss of materials as the runners and sprues (i.e., the solid pieces formed by solidification of molten material within the channels that connect different casted parts to a single feeding point) can be recycled after separation from the main components. Lost-wax casting is not fully automated, and in some cases is very arduous and time-consuming [68]; lost-wax is best-suited for production of small- and medium-sized batches, and for parts with highly complex shapes.

Lost-wax casting begins with the formation of a positive master in a sacrificial material, which is traditionally done via injection of liquid wax into a precision mold. Nowadays, with stereolithography (SLA), the wax copy of the part can be fabricated quickly and inexpensively without sacrificing its dimensional accuracy. In SLA, the wax part, i.e., master, is built layer by layer out of UV curable liquid resin [69] (Figure 2). One or more masters are then assembled with wax sprues and runners that serve as feedstock feeder system and that also facilitate handling (Figure 3). The wax superstructure (i.e., master(s), sprues, and runners) is then encased inside a ceramic matrix using a flask where liquid slurry is poured. After drying, the ceramic is sintered, resulting in a ceramic mold with high mechanical strength. During sintering of the ceramic, the wax melts and burns, leaving cavities inside the ceramic mold that closely follow the geometry of the wax superstructure (the cavities are a negative copy of the wax superstructure). After that, the molten metal is poured into the mold, filling-in the cavities by gravity or due to centrifugal force. After the melt solidifies and is cooled, the mold is destroyed to extract the metal superstructure [70].

15
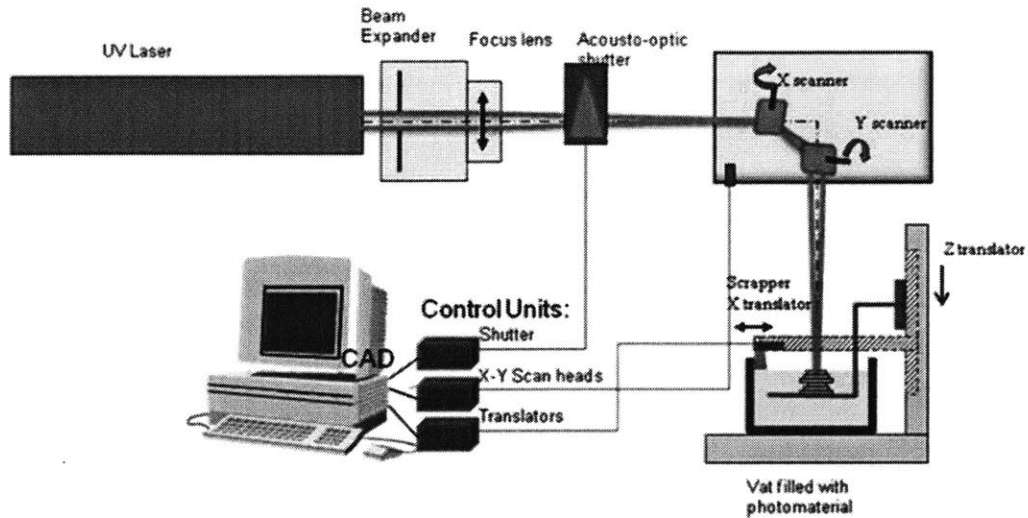
Figure 2 Schematic of stereolithography process [69].
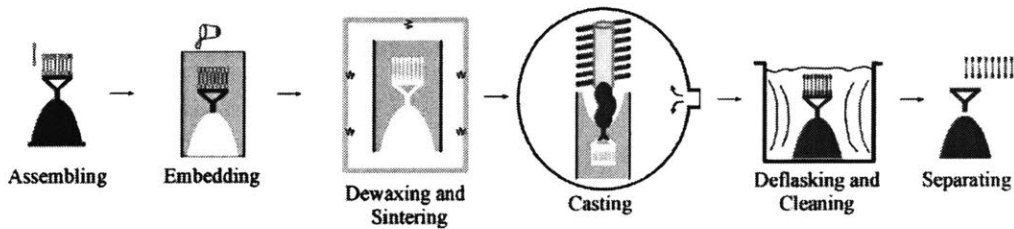
Figure 3 Diagram of investment casting process [174].

Finally, the individual parts (i.e., metal versions of the wax masters) are separated from the runner system; depending on the casting alloy and the investment material, chemical cleaning of the metal parts is sometimes necessary.

Due to the nature of the casting process, a high-precision master is required for successful replication of the part in metal; SLA can create accurately and quickly in a wax-like resin the part to be casted from its CAD file. In SLA, a ultraviolet (UV) light source (a laser or an array of LEDs) selectively photopolymerizes a liquid polymer vat, chemically bonding small molecules to create an infusible, insoluble, and highly cross-linked 3D polymer network [71], [72]. In an SLA-printed part, the amount of cross-linking is directly related to the amount of energy exposure received during its production [73]–[75]. Since the power of the laser/LED is not high enough to completely cross-link the resin, post-UV curing is required. It is possible to post-process SLA-printed parts with heat instead of UV, but it typically causes major warpage [76], [77], which is a major concern if the part has thin-walled sections. The layer thickness used to SLA-print the wax

16

master determines its surface roughness in the plane parallel to the build direction (i.e., the vertical sides of the print; the bottom surface is attached to the build platform, while the top surface is the last layer printed). When the vertical surface is parallel to the molded part's direction of ejection, it affects the force required to remove the part from the mold (the surface roughness and associated ejection forces are proportional to the build layer thickness). Therefore, to reduce the force needed to eject the part, the part can be reoriented, and/or the layer thickness can be reduced. However, present resin and machine technology have practical limits in the reduction of layer thickness considering the increase in build time associated with thinner layers. For example, a part printed with a Formlabs Form 2 using 200 μm layers takes 45 minutes, while the same machine printing the same object in 100 μm layers would take around 1.5 hours [78].

In a nutshell, in order to improve the overall dimensional accuracy, as well as reduce porosity and surface roughness of the casted part, it is essential to improve each of the individual stages of the manufacturing process for different material combinations of master, investment and metal parts. Important factors are summarized as follows:

- *Castability of the alloy:* flowability and form-filling ability, little contraction and shrinkage, reduced segregation, low porosity and shrinkage cavitation, little hot crack susceptibility, high surface quality, and good mechanical properties;
- *Properties of the ceramic investment:* the investment should be capable of achieving a very precise replication of the wax mold with low surface roughness, and its expansion properties should match those of the alloy used;
- *Casting conditions,* such as the preheating temperature of the mold and the casting pressure, greatly influence the grain size and mechanical properties of the casted part [79].

If the mold temperature is too low, or the overheating of the melt is not high enough, or the filling pressure is too low to overcome the surface tension of the melt, the metal feedstock will solidify before the cavities of the investment are filled-in completely, leading to incomplete casting. Porosity can appear in the casted part due to various reasons e.g., the master is improperly sprued (sprues may be too thin, too long or not attached in the proper location), the metal reservoir is too small to eliminate shrinkage porosity, there is gas contained in the metal, the mold and/or metal are too hot, there is too high moisture, poor mold burnout. Shrinkage holes would form if the solidification rate is not matched by feedstock feeding; surface shrinkage holes and surface pores are caused by an excessive casting temperature. High surface roughness is related to poor quality of the master, insufficiently cured ceramic investment before placing into the burnout oven, prolonged time the investment flask held in steam dewax, overheated metal and/or flask [80]. Continuing efforts are underway to improve the properties of SLA-printable waxes through the addition of additives and fillers to produce a blend that offers better surface finish, minimum shrinkage, and moderate hardness

17

[81]–[84]. Investigations on the modification of the investments have been conducted to reduce the surface roughness of the casted parts [85]. A complete optimization of the lost-wax process is yet to be attempted to thoroughly cover the physical variables associated with the thermochemical process.

2.3. Binder inkjet jetting 3D printing

Binder jetting printing is a two-step process for powder feedstock that decouples the printing of the part from its heat treatment, making possible to use a homogeneous sintering environment to consolidate the part with a uniform microstructure. In the first step of the process, components are created by injecting at room temperature binders into the areas of the powder layer that are intended to be consolidated. Specifically, as shown in Figure 4, a thin layer of powder is first distributed on the platform by a leveling roller and then and array of inkjet nozzles moves along the X and Y directions to locally distribute binders to adhere powders together. The binder is a polymer dissolved in water; during drying, water evaporates and the polymer remains –sticking the powder particles together [86]. After completing bonding of the powder of the current layer, the platform moves down (Z direction) for a distance equal to the layer thickness, another layer of powder is distributed, and the binder injection process repeats. When all the layers are built, the fragile binder–metal mix part is cured to gain mechanical strength, becoming a "green" part, which is then extracted from the powder box and transferred to a furnace to completely burn out the binder while sintering the print at a temperature of above 1000 °C for 24-36 hours [41]; the debinding process is carried out following a thermal profile specific to each binder and metal power combination. The green part becomes very brittle with binder decomposition and evaporation as temperature increases. A minimum temperature must be maintained to pre-sinter the part to allow it to be handled. The loosely packed metallic powder is bonded together through sintering and consolidation, inducing densification and conferring mechanical strength. Similar to the DMLS process, the unattached powder can be recycled, leading to significant gain of material utilization. Unlike traditional machining, binder jetting printing has more versatility to create free-form geometries; moreover, unlike SLA, binder jetting-printed parts don't require any auxiliary support structures because the power bed serves as support.

The major processing parameters that control the morphology and density of a binder jetting-printed part are (i) powder size, (ii) layer thickness, (iii) binder concentration, (iv) packing density, and (v) heat treatment conditions. Finer powder often increases the density of the product, and also helps achieve finer feature size; however, the efficiency of densification is decreased for a finer powder due to the powder spreading issue [86]. Larger layer thickness reduces the processing time but increases the porosity. In addition, parts are prone to failure during binder burnout if the binder concentration is high; therefore, the binder concentration must be minimized while still providing sufficient mechanical stability to the printed structure. Improving the packing density of the printed powder helps consolidate the powder better and

18
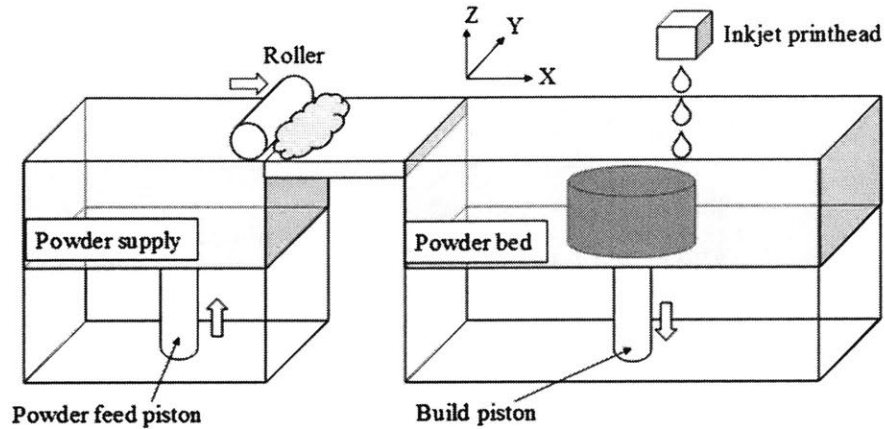
Figure 4 Schematic of binder jetting 3D printing technology [37].

reduce the shape distortion in the final parts. The heat treatment affects the microstructure, which determines the mechanical properties of binder jetting-printed metals. The binder burnout temperature must be compromised between the temperature beyond which the complete binder burnout is possible and the temperature under which the oxidation of SS powders is minimized. Moreover, the parts shrink during the sintering process, and, unfortunately, the shrinkage is not necessarily uniform, which would impair geometrical accuracy and, even worse, trigger cracking –leaving the parts useless. Research has shown that near-fully dense stainless steel parts with better surface finish are possible by using as feedstock powders of various sizes, and by adding a small amounts of boron as sintering additive to reduce the sintering time and temperature [87].

2.4. Specimen fabrication

2.4.1. DMLS-printed SS 316L specimens

The DMLS SS 316L samples were made with a Farsoon FS121M printer (Farsoon Technologies, Hunan, China), shown in Figure 5, using SS 316L powders with ~35 μm average diameter as printable feedstock. The main specifications of the printer are listed in Table 1 [88] and the features of the stainless steel power used is listed in Table 2 [89]. The powder melting and fusion was performed under nitrogen gas by a 200W, 1060 nm Yb-fiber laser featuring a 100 μm focus diameter, traveling at 700 mm/s with hatch spacing equal to 80 μm. The distance of two successive melting points along a scan line is set at 120 ± 5 μm (i.e., the pixels measured ~120 × 80 μm). Specimens were built with ~30 μm thick layers, each layer was scanned once, except for the first layer that is scanned twice. The first layer was built by double scanning along 67° from the X-direction, and for each subsequent layer, the scan vectors are perpendicular
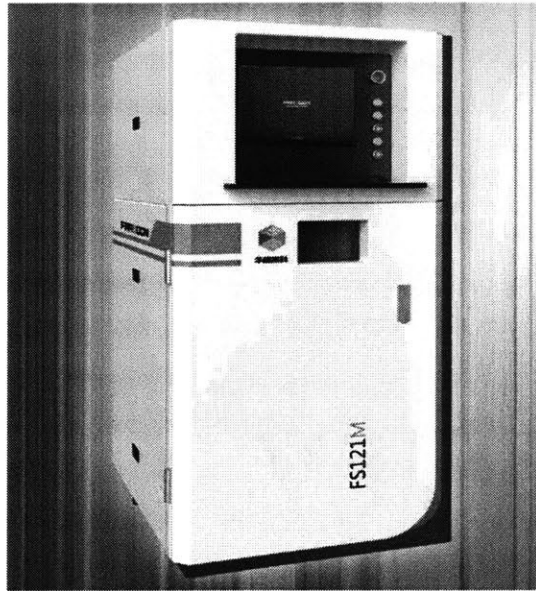
Figure 5 A Farsoon Metal Solutions FS121M [88].

Table 1 FS121M Specifications [88]

Effective Build Size (LxWxH)	120 × 120 × 100 mm
Layer Thickness (Typical)	Adjustable 0.02 - 0.08 mm
Volume Build Rate*	5 cm³/hr
Scanning Speed**	15.2 m/s
Laser Type	200W Yb-fibre laser
Spot Diameter	0.04 - 0.1 mm
Inert gas supply	Argon or Nitrogen

* Build quality degradation may occur outside the effective build size. ** Max build rate, material dependent.

Table 2 General Properties of FS316L Stainless Steel 316L

Average Particle Size (D50)	30 ~ 40 μm
Particle Size Range (D10~D90)	20 ~ 60 μm
Apparent Density	3.5 ~ 4.5 g/cm³
Tap Density	4.5 ~ 5.5 g/cm³

to the previously deposited layer (Figure 6). After furnace cooling down to room temperature, the parts were removed from the build plate via EDM wire cutting. Supporting structures are used to assist the
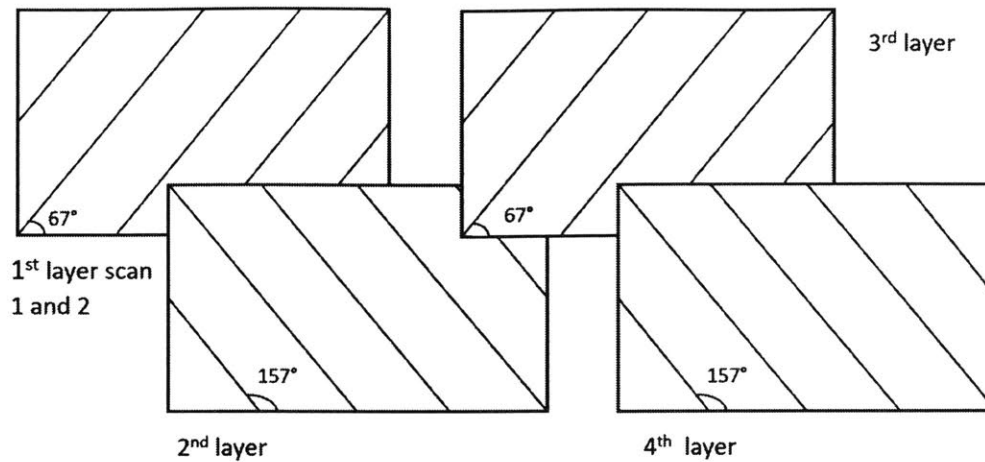
Figure 6 Schematic of the laser scanning pattern used to fabricate DMLS SS 316L specimens – double scan of the first layer along 67°, and for each subsequent new layer a single scan shifted 90° relative to the previous layer.

detachment of the part (the support structures provide material between the build platform and the part itself so neither of them are damaged during part removal). Support structures were removed by hand using hammer and chisel to avoid the temperature increase incurred during the tooling process.

2.4.2. Casted sterling silver specimens

The masters of the sterling silver micromolded samples used in this study were printed in B9 Creator Emerald resin (B9Creations, LLC, Rapid City, SD, USA) using CAD files in STL format with a Solus digital light projection (DLP)-SLA printer (Junction 3D, Santa Clarita, CA, USA), shown in Figure 7. The Solus is a DLP projector-based SLA printer that uses a peeling mechanism to eliminate the need for replacing or re-coating resin tanks with PDMS, while at the same time providing a non-stick surface for smooth peeling; the peeling mechanism allows printing objects with high surface quality and very fine details. The resin B9 Emerald provides clean burnout without staining the investment, enables casting of thicker objects, and is pigmented for 25 μm - 70 μm layer thickness for printing with fine features. Plasticast® BANDUST™ (Ransom & Randolph, Maumee, OH, USA) is employed for casting. The material is a gypsum-based jewelry investment which contains a refractory material, a bonding material, and controlling chemicals. The refractory material, silica, can withstand high temperatures without decomposing. Gypsum is the bonding material, which holds the refractory materials in place to form a
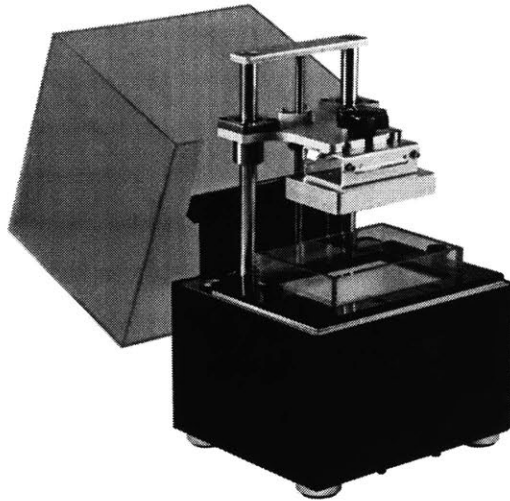
Figure 7 Solus DLP-SLA printer [175].

1. Weigh Investment

2. Measure Water

3. Always add investment to water

4. Mix 3-3½ Minutes

5. Vacuum for 20 seconds after starts to boil

6. Pour into flask

7. Vacuum up to 90 seconds.

8. Let flasks sit still for 2 hours

9. Preheat Furnace to 300° F / 149°C

10. Remove spruce base

11. Load into furnace

12. Follow burnout cycle
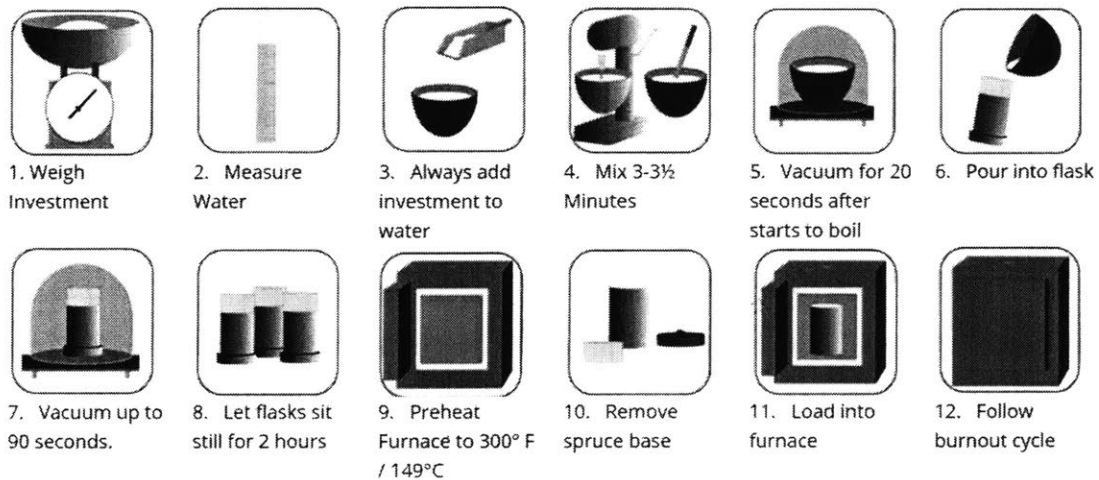
Figure 8 Investment Mixing and Burnout Instructions [91].

mold. The controlling chemicals are used to adjust and accentuate various investment properties. The Plasticast® BANDUST™ produces up to 99% less respirable dust exposure during the investing process compared to competing investments, while maintaining the same final casting quality. Besides, it is an extra high strength investment with isotropic expansion that can maintain smooth mold surface and dimensional integrity [90]. In addition, the Plasticast® BANDUST™ investment can easily be removed in water.

To print each master, the in-plane (XY) resolution is set at 25 μm × 25 μm pixels and the layer thickness is set at 30 μm. In some cases, support structures were included to assist the creation of the part. After
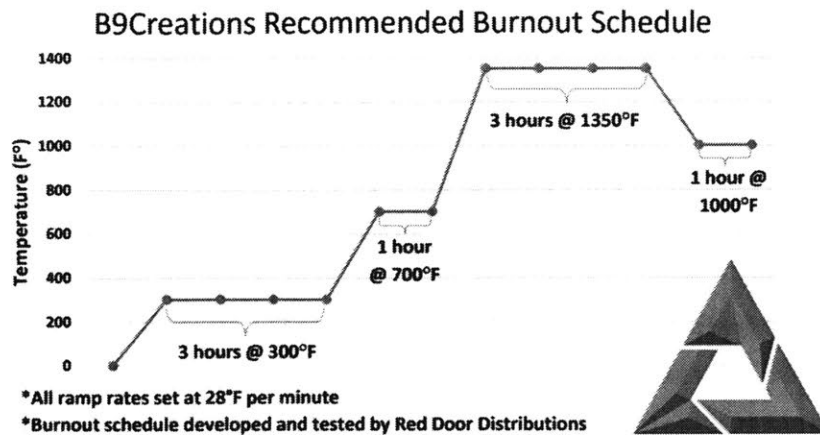
Figure 9 B9 Emerald resin burnout schedule [95].

printing, the parts were sequentially dipped in a 90% isopropyl alcohol and ultrasonic rinse for 30 s to remove uncured resin, followed by immersion in water with detergent, and finally rinsed in clean water for about 30 s. After the prints were dried with an air gun, post curing was performed at 45 °C for at least 120 minutes using a 405 nm light source. The supports were then carefully clipped off by hand, and sprues and runners are added to the master(s). After the wax superstructure is made, the casting process continues with mixing the pre-weighted investment with water (Figure 8 [91]). The water-to-investment powder ratio is in the range of 38:100-42:100 for this product [90]. If the water-to-powder ratio is too low, the investment would be difficult to pour, and the removal of the casted part would be difficult due to the compressive strength of the fully-fired ceramic; also, a high water-to-powder ratio may contribute to cracks or a rough surface finish [92], [93]. De-ionized water was mixed with the investment powder because it features a lower pH and conductivity, which reduce the variability in pour time, set time, and fluidity, making the investing process more consistent and reproducible [92], [94]. The investment powder was added to water instead of the other way around, as it would be difficult to mix and will affect the working time. The investment mix was then placed in a vacuum chamber, applying enough vacuum to cause a rapid outgassing and pour into the flask. The invested flask was vacuumed for ~1.5 min to release air bubbles, slightly vibrating or tapping the flask during this operation to assist air release. Afterwards, the flask was immediately transferred to a vibration-free storage area for initial hardening and bench curing for about 2-6 hours. The sprue base was then removed, and the flask was loaded in the burnout oven to burnout the resin following the schedule recommended by the vendor, shown in Figure 9 [95]. A centrifugal casting machine was used to fill-in the cavities left by the burning out of the wax master with sterling silver. Finally, the resulting metal parts were washed in an acid bath to remove residual oxides, and carefully polished.

2.4.3. Binder inkjet-printed SS 316L specimens

The binder inkjet-printed SS 316L samples used in this study were made with a DM P2500 printer (Digital Metal, Hollsopple, PA, USA) at room temperature; the printer is shown in Figure 10 and its specifications are summarized in Table 3 [96]. The printer uses a feedstock powder that contains 17% Cr, 12% Ni, and 2.2% Mo (Table 4 [97]) that is optimized to attain a high density in the printed material at the green state [86]. The tool has ~30 μm × ~30 μm in-plane pixels and prints in ~35 μm thick layers. The binder is a water-dissolved polymer glue that is digitally applied to agglomerate the powder in the designed shape with sufficient strength. There is no need for building support structures because the printed components are adequately held by the powder bed, which facilitates removal of powder during cleaning and reduces the need for post treatment. The printing process is performed without protective gas because there is no heat involved during printing. The green components can be produced with high detail level and tolerance because no melting takes place during the building of the object. After carefully removing the loose powder, the parts are annealed at ~1,360 °C in vacuum with a partial pressure of nitrogen applied to eliminate trapped air, obtain a final high density, and maintain good dimensional stability. Among the metals that compose the SS 316L alloy, chromium has significantly high vapor pressure at the annealing temperature and tends to vaporize [98]; however, conducting the annealing at nitrogen partial pressure reduces the surface chromium evaporation as the vaporizing Cr will collide with nitrogen molecules within the furnace, which is crucial to maintain the high corrosion resistance of austenitic Cr-Ni-steel [99]. The printed part shrinks during annealing due to the high porosity of the green component; however, because the amount of shrinkage is repeatable and can be measured, it can be compensated at the design stage. Finally, the parts are carefully polished.
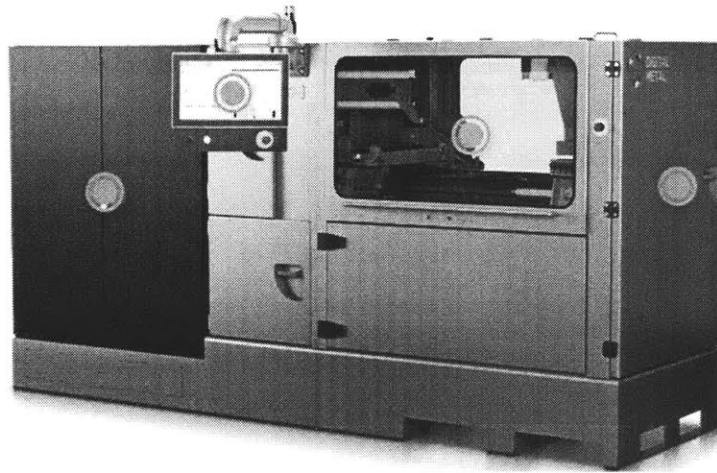
Figure 10 DM P2500 digital metal printer [96].

Table 3 DM P2500 Digital Metal process capabilities [96]

Effective Build Size (L×W×H)	203 mm × 180 mm × 69 mm
Layer Thickness (Typical)	Adjustable 0.02 - 0.08 mm
Build volume (scaled):	170 mm × 150 mm × 57 mm (L × W × H)
Build volume (unscaled):	203 mm × 180 mm × 69 mm (L × W × H)
Minimum length	1 mm
Maximum length	Preferably <50 mm
Corner radius	35 μm
Chamfer	Steps of 35 μm in z direction
Wall thickness	Preferably ≥ 300 μm. Minimum ≥ 150 μm
Resolution Maximum	35 μm in z direction
Holes	≥ 200 μm depending on hole length
Productivity	60 cm³/h scaled; 100 cm³/h unscaled

Table 4 Stainless Steel 316L Chemical Composition (%) [97].

	Fe	Cr	Ni	Mo
316L	Bal	16-18	10-14	2-3

3. Sample Characterization Methods

3.1. Metrology

The Mitutoyo Quick Vision ACTIVE 202 (Mitutoyo America Corporation, Marlborough, MA, USA), shown in Figure 11 [100], offers a wide field of view with interchangeable objective zoom lenses to measure small to large features. The 8-step zoom lens can achieve a magnification between 0.5X and 7X while maintaining crisp image quality: with the 1X objective, the tool achieves a magnification between 0.5X and 3.5X with a working distance of 74 mm; with the 2X objective, the tool achieves a magnification between 1X and 7X. The illumination of the programmable LED stage, coaxial light and 4-quandrant LED ring light can be controlled independently in every direction, front and back, right and left, to configure highly variable lighting settings to match measurement locations. Reliable edge detection is achieved by selecting the optimal focus among surface focus, pattern focus, edge focus and laser auto focus according to each surface texture and measured features [101].

3.2. Scanning electron microscope (SEM)

An SEM is useful for observing the surface morphology of a specimen at high magnifications. Compared with optical microscope, an SEM offers a wider range of magnifications with greater focal depth. A brief description of the imaging formation is described here, more details can be found in SEM reference books and other materials [102], [103].

The main components of a typical SEM are the electron column, the scanning system, one or more detectors, the display, a vacuum system, and control electronics (Figure 12 [104]). The electron column of the SEM consists of an electron gun and two or more electromagnetic lenses operating in vacuum. The
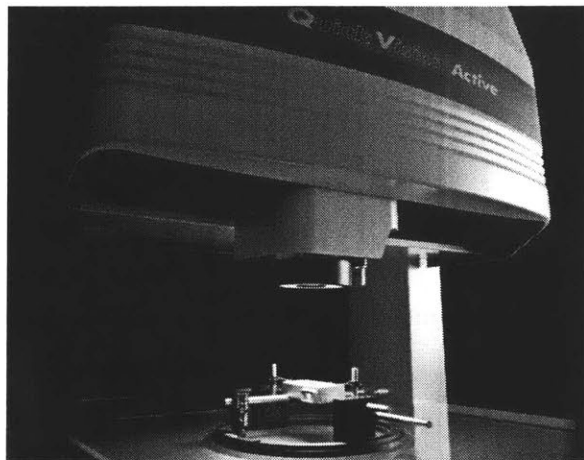
Figure 11 QV ACTIVE with optional Opti-fix clamping system [100].
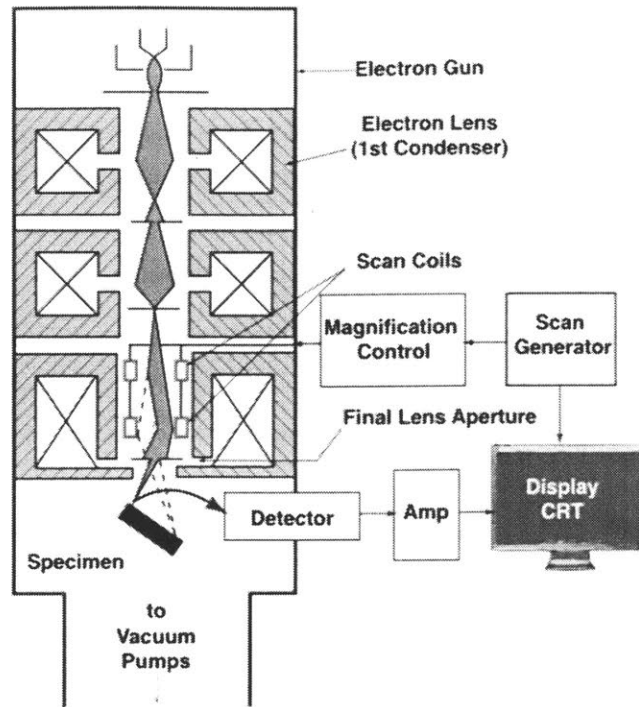
Figure 12 Schematic illustration of scanning system of the scanning electron microscope [104].

Figure 13 HITACHI High Technologies Tabletop Microscope TM3030 [105]

electron gun generates free electrons and accelerates these electrons to energies in the range of 1-40 keV in the SEM. The electron optics of the SEM provides the microscope with the capability of forming a beam at the specimen surface typically with spot size diameter in the range of 1 nm to 1 μm, beam current between pAs and μAs, and probe convergence angle between 10^{-4} to 10^{-2} radians. The electron beam enters the

specimen chamber and strikes the specimen at a single location; elastic and inelastic scatterings occur within the interaction volume. The scattering produces secondary (SE) and/or backscattered electrons (BSE) that are collected by a detector; the resulting signal is amplified and displayed on a computer monitor. SEs are produced near the sample surface and the SE image obtained reflects the fine topographical structure of the sample. BSEs are electrons that are reflected upon striking the atoms composing the sample whose number is dependent on the composition (average atomic number, crystal orientation, etc.) of the sample; therefore, a BSE image reflects the compositional distribution on the sample surface.

Scanning is usually accomplished by driving electromagnetic coils arranged in sets consisting of two pairs for deflection in the X and Y directions, respectively. A typical double-deflection scanning system, as shown in Figure 12, has two sets of scan coils, located in the bore of the final (objective) lens, which first drive the beam off-axis and then back across the optical axis, with the second crossing of the optical axis taking place in the final aperture, hence sampling the specimen at a controlled succession of points.

The HITACHI High Technologies Tabletop Microscope TM3030 (Figure 13) was employed in this study [105]. The TM3030 can observe BSE images using high-sensitive semiconductor 4-segment BSE detector incorporated in FE-SEM and VP-SEM. The magnification is adjusted in the range of 15X to 60,000X. The chamber can accommodate samples up to 70 mm diameter, travelling ±17.5 mm in the X- and Y-directions. When a non-conductive sample is imaged, detectors are operated under low-vacuum conditions with the charge-up reduction mode.

3.3. Scanning confocal microscope surface texture characterization

Surface texture reflects the local deviations of a surface from its ideal shape. Surface texture can cause variations in the physical and chemical properties of a material. Roughness is one of the most critical surface texture parameters; it plays an important role in determining how an object will interact with its environment, e.g. the initial points of cracks or corrosion. Measurement of the surface texture is important in many disciplines, in particular, in the machining of precision parts and assemblies that contain mating surfaces or that must be operated under high pressure.

There are several instruments, based on various techniques, that can be used to characterize surface texture. The measurement techniques can be divided into *contact* and *non-contact* methods; in each category, the optimal method is chosen based on the prior knowledge of aspects such as the range of the surface roughness, and reflectance of the examined surface. Contact methods involve tracing a stylus across the surface of the specimen, such as stylus profilometer for nano to micron meter range roughness, and the atomic force microscope (AFM) for nanometer roughness. Non-contact methods, also known as optical methods, include white light interferometry for roughness smaller than a quarter of the wavelength of green

light, and confocal microscopy (nanometer to micrometer range). Optical methods can perform fast, high-accuracy and, most importantly, non-destructive characterization of surface texture. Besides, it makes the construction of topography maps possible, enabling the determination of the whole surface under test.

A laser confocal microscope is a light-based microscopy system that uses a laser passing through the confocal optical path for image formation. In conventional light microscopy, the image is formed simultaneously for all observed points of the entire field of view; in contrast, a laser confocal microscope forms the image pixel by pixel using photomultipliers or CCD. The resolution of a stylus profilometer is governed by the tip diameter and shape selected for surface analysis. The tip radius of a general contact-type stylus is about 2 to 10 µm, which causes the roughness data to be "filtered". In contrast, with a diminutive laser spot, a laser confocal microscope can measure surface roughness of micro geometries at higher resolution than a contact-type stylus, including mapping shapes that the stylus cannot reach. Moreover, in roughness measurements across an area in which line scanning across an arbitrary rectangular range is required, a laser scanner can provide a finer lateral separation with a reasonable evaluation time. A laser scanning confocal microscope (LSCM) configured with confocal aperture can compile a series of 2D images captured at step size through a specimen into a 3D data set, providing pixel intensity and sub-micron spatial information adequate for the quantitative surface measurements that were conducted in this study.

Unlike a conventional wide-field microscopes where the entire specimen is illuminated and viewed, the method of image formation in a confocal microscope is achieved by scanning one or more focused beams of light, usually from a laser, across the specimen [106], [107]. In LSCM (Figure 14 [108]), the point source produced by a pinhole placed in front of a laser source is focused by an objective lens into the specimen, and light reflected by the surface is focused by the same objective lens and passed through a second pinhole located in front of the detector and confocal with the first pinhole. Any light that passes through the second pinhole strikes a low-noise photomultiplier, which produces a signal that is directly proportional to the brightness of the light. The second pinhole prevents light from above or below the plane of focus from striking the photomultiplier which is the key to the confocal approach, eliminating the ambient light and out-of-focus light from the specimen by spatial filtering –enhancing both lateral and axial spatial resolution by significantly improving image contrast [109], [110]. This reflection arrangement eliminates the considerable problem of aligning the two objective lenses in the transmitted light version since a single o objective lens is used for both the excitation and the emission paths. In a LSCM the vertical resolution of the measurement depends on the resolution of the microscope used, i.e., the depth of focus *DOF* [111]
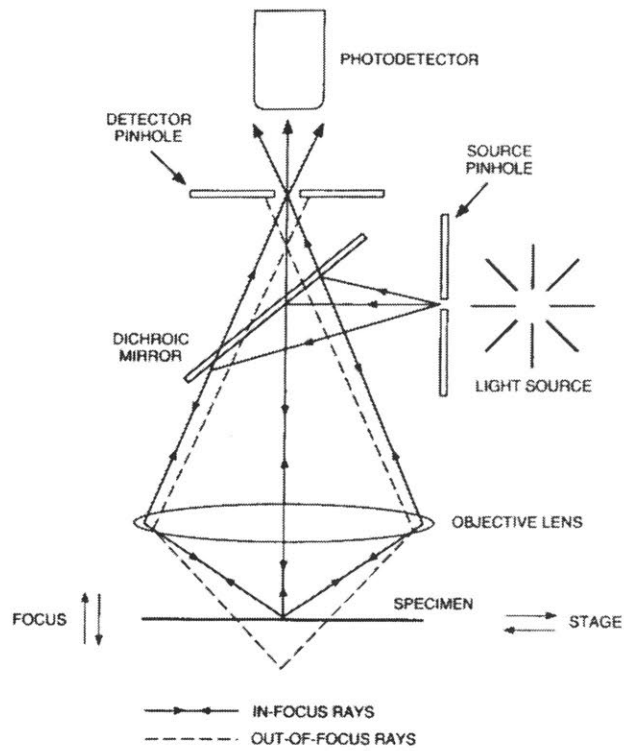
Figure 14 The light path in a typical LSCM.
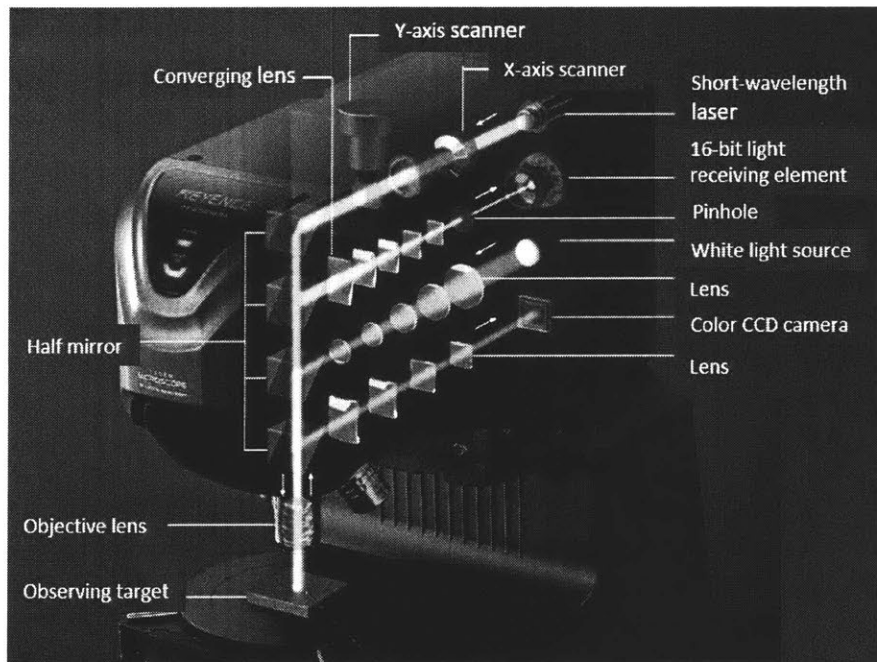
Figure 15 Principle of measurement and observation of Keyence VK-X250 [176].

$$DOF = \frac{\lambda}{4n\left(1-\sqrt{1-\left(\frac{NA}{n}\right)^2}\right)},$$ (3-1)

where λ is the wavelength of the light source, n is the reflective index of the medium, and NA is the numerical aperture of the objective lens. From an optical point of view, height variation smaller than the depth of focus is not detectable by the photo multiplier tube because it cannot detect the variation in the reflected light intensity. Lateral resolution, according to the Rayleigh formula, is determined by the NA of the objective lens and the wavelength of the illumination [19]

$$\varepsilon = 0.61\frac{\lambda}{NA},$$ (3-2)

which indicates the level of in-plane details actually observed in the specimen.

Surface texture of the printed samples was examined with a point scanning confocal microscope Keyence VK-X250 (Figure 15) with illumination provided by 0.95 mW laser, generating a monochromatic 408 nm light beam with 0.2 μm spot size. Reflection from sample surfaces was collected with 20X lens ($NA = 0.46$, working distance $\{WD\} = 3.1$ mm) or 50X lens ($NA = 0.95$, $WD = 0.35$ mm), and received by a high-sensitivity 16-bit photomultiplier that captures the weakly reflected laser light –enabling nanoscale measurements. The X-Y scanning repeats for each Z position within the field-of-view by dividing the region into up to 2048 × 1536 pixels, generating height and color data. Image stacks with the optimal number of sections for maximal z-resolution (for the lens) were transformed into topographical images for measurements. For the two lenses used in this work, the axial resolution is limited to 0.910 μm and 0.148 μm for 20X and 50X, respectively, and the lateral resolution are 0.541 μm and 0.261μm, respectively, according to Eq. (3-1) and Eq.(3-2). Therefore, in theory, although the optimal scanning pitch should be equal or larger than the depth of focus in function, even with a fine scanning pitch, the axial resolution is still limited by the characteristics of the objective lens. However, in this instrument, a linear scale module is included in which the sensor that measures dimensions uses two scales to convert movement and displacement into electrical signals, improving the Z-resolution of the objective lens to 0.5 nm with 10 nm increments of the Z drive and with X and Y step size 10 nm, resulting in a resolution as high as 1 nm.

3.4. Characterization of thermal diffusivity

The method used for measuring thermal diffusivity employed in this study is a laser flash. The technique assumes an infinite slab specimen of dense material having a thickness L_c that is initially at a uniform temperature, which is then subjected to an instantaneous, spatially uniform impulse of radiant energy at its front surface, leading to a measurable temperature increase at its opposite rear face. The specimen is assumed to be opaque, thermally insulated, homogeneous, and isotropic [112], and the thermophysical

properties and density of the test material are constant within the temperature excursion induced by the impulse (usually 2-10 °C). With these assumptions, the heat flow is treated as one-dimensional, occurring throughout the thickness of the slab, i.e., the z direction (i.e., there are no heat losses). The transport of heat through the sample causes a transient temperature rise, $T(z,t)$ on the rear (or top) surface of the specimen (i.e., $z = L_c$) which is expressed as [113]

$$T(L_c, t) = \frac{Q}{\rho c_p L_c}\left[1 + 2\sum_{n=1}^{\infty}(-1)^n \exp(\frac{-n^2\pi^2\alpha t}{L_c^2})\right],$$
(3-3)

where Q is the radiant pulse energy per unit surface area, t is time, and c_p, ρ, and α are the specific heat, mass density, and thermal diffusivity, respectively, of the material being analyzed. By dimensionalizing the temperature in terms of the maximum excursion temperature at the rear surface after an impulse, i.e., $T_m = Q/(\rho c_p L_c)$, and rewriting the time as $\omega = \frac{\pi^2\alpha t}{L_c^2}$, the temperature at $z = L_c$ can be written as

$$V(L_c, \omega) = 1 + 2\sum_{n=1}^{\infty}(-1)^n \exp(-n^2\omega).$$
(3-4)

The thermogram plot from Eq. (3-4) is shown in Figure 16, with $t_{0.5}$ representing the half-rise time, i.e., the time required for the rear-face temperature to reach half the maximum [114]. The precision of the flash method depends on how the experimental conditions resemble the assumptions formulated as the initial and boundary conditions of the analytical model. Of course, the samples used in the actual experiments have finite in-plane dimensions, causing possible heat loss by radiation or conduction at the sample, potentially invalidating the one-dimensional heat flow assumption. Besides, since the sample is not perfectly insulated, the radiative heat losses on the normal surfaces is unavoidable. Furthermore, as the laser impulse is not infinitely short in duration, the heat input is not instantaneous, leading to possible overlap with the characteristic rise time of the rear-face temperature caused by heat transport through the sample. Non-uniform heating is another issue that affects the experiment, which stems from the nonuniform laser-beam energy profile, as well as non-uniform absorption of the radiation energy over the front face surface. However, the last two phenomena are mostly encountered in measuring thin, high-diffusivity materials [112].

The thermal diffusivity of the samples used in this study were measured with the laser flash technique using the instrument NETZSCH LFA 457 MicroFlash. Compared with conductivity measurements using other products from NETZSCH, e.g., the GHP (Guarded Hot Plate), the HFM (Heat Flow Meter), or the TCT (Thermal Conductivity Tester), the LFA is configured to handle much smaller sample sizes and the investigations generally take much less time, while HFM, GHP and TCT are those primarily used for inhomogeneous sample materials (insulation materials) considering their relatively large sample capacities.
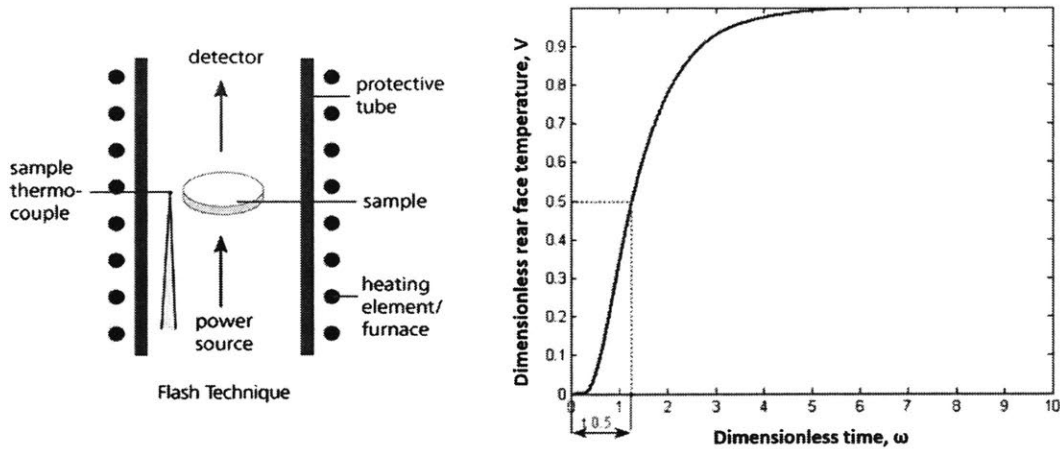
Figure 16 (a) Schematic of the laser flash method for thermal diffusivity; (b) Dimensionless plot of the theoretical rear surface temperature.

Table 5 Sample geometry suitable for LFA, GHP, HFM and TCT techniques [115].

	LFA	GHP	HFM*	TCT
Sample shape	Round or rectangular	Square	Round or rectangular	Rectangular (cuboid)
Number of pieces per sample	1	2	1	2
Diameter and/or edge lengths (mm)	6 - 25.4	300 × 300	150 × 150 - 300 × 300 or 305 × 305 - 610 × 610	≥200 × 100 (Standard: 230 × 114)
Max. thickness (mm)	6	100	100 or 200	76
Min. thickness (mm)	0.01, dependent on sample	~ 1, dependent on sample	~ 5	50
Applicable temperature (°C)	-120 – 2800 or -125 - 1100 or -100 - 500	-160 - 250	-30 - 90	RT - 1500

* Two models of HFM are available for different sample sizes.

An overview of different methods of suitable sample and the temperature ranges are summarized in Table 5 [115].

The NETZSCH LFA 457 MicroFlash, shown in Figure 17, can measure thermal diffusivities between 0.01 mm^2/s and 1000 mm^2/s (i.e., thermal conductivities between 0.1 W/(m·K) and 2000 W/(m·K)). The thermal diffusivity is determined with ±3% accuracy and the specific heat capacity can be directly determined with ±5% accuracy for most materials [116]. The 1054 nm Nd: Glass laser in the system has a
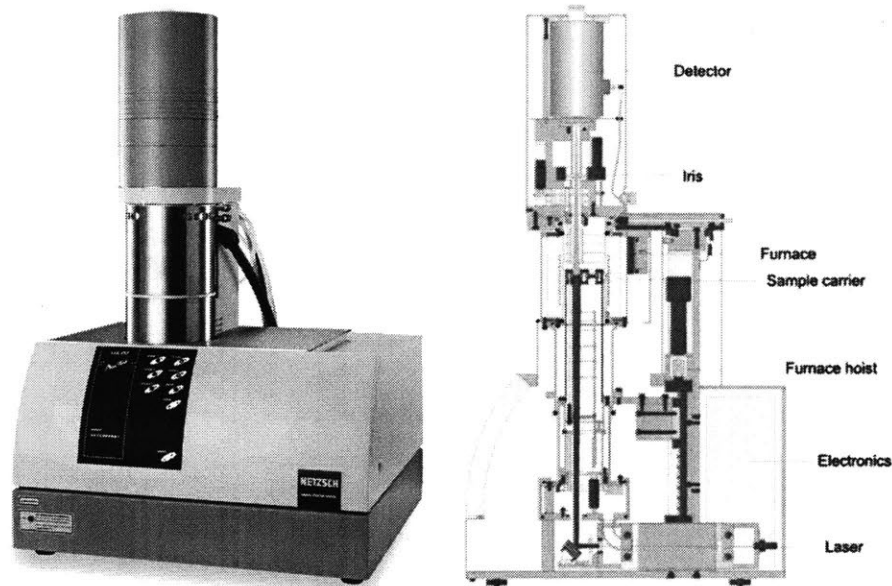
Figure 17 LFA 457 MicroFlash (a) Apparatus; (b) Schematic diagram [116].

maximum pulse energy of 18 J and a uniform pulse width over the entire pulse duration of 0.3 ms, producing sharp and defined peaks with negligible tailing. Two interchangeable detectors are available to cover different temperature ranges, with the standard InSb (Indium Antimonide) detector designed for the high-temperature range, and the highly sensitive MCT (Mercury Cadmium Telluride) IR-detector for the lower temperature range between -125 °C and 500 °C. To conduct a measurement, the lower surface of a plane parallel sample is first heated by a short energy pulse; the resulting temperature change on the upper surface of the sample is then measured with an infrared detector.

3.5. Electrical resistivity characterization

When estimating the resistance of switch or relay contacts, a common multimeter often produces high, almost meaningless resistance readings due to the very low currents involved in the measurement. Typical off-the-shelf multimeters offer a low resistance measurement on the order of 200 Ω full scale with a resolution of 0.1 Ω, which is inadequate for conducting these measurements. For quantitative measurements of components like switches and relay contacts, the resistance is typically 1 Ω or less and needs to be determined with a resolution on the order of mΩ.

The specifications on some handheld 2-wire meters indicate a 200 mΩ range with 1 mΩ sensitivity. The lead resistance (typically 10-100 mΩ) [117] could be zeroed out, but the uncertainty of the contact
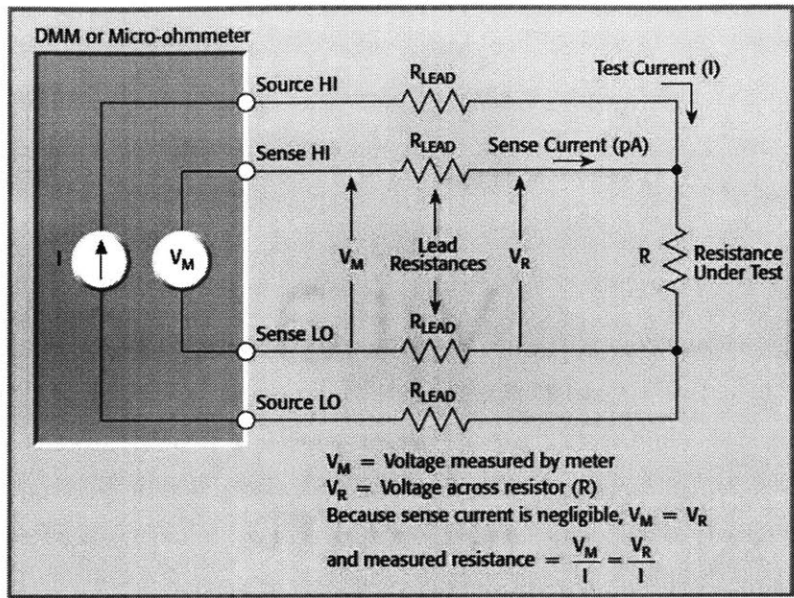
Figure 18 Four-Wire Resistance Measurement [177].
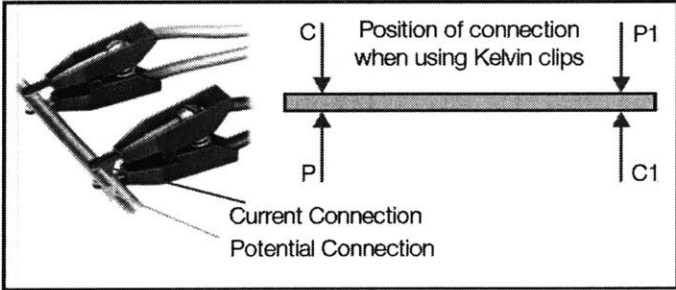
Figure 19 Kelvin clips for four wire terminal connection [178].
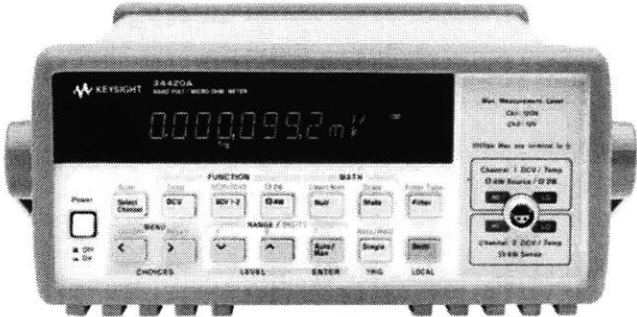
Figure 20 Hewlett Packard 34420A Micro-Ohm Meter [179].

resistances is left and can change with each measurement. Contact resistance values may be in the 35 mΩ

range at each probe and can vary with the temperature of the material under investigation. The two-wire test method is best used for readings above 10.00 Ω up to 1.0 to 10.0 MΩ [118].

Due to the limitations of the two-wire method, the four wire (Kelvin) connection method, shown in Figure 18, is generally preferred for low-resistance measurements. With this configuration, the test current I is forced through the test resistance R through one set of test leads, while the voltage V_M across the resistance under test is measured through a second set of leads called *sense leads*. Although small, pA-level current may flow through the sense leads, it is usually negligible and can generally be ignored for all practical purposes. The voltage drop across the resistance of the sense leads R_{LEAD} is negligible, so the voltage measured by the meter V_M is essentially the same as the voltage V_R across R. Consequently, the resistance value can be determined much more accurately than with the two-wire method. Note that the voltage-sensing leads should be connected as close to the resistor under test as possible to avoid including the resistance of the test leads in the measurement. The terminals used in the circuit are Kelvin clips instead of crocodile clips (Figure 19), where each jaw of the Kelvin clip is insulated from the others. The current lead is connected to one jaw and the potential lead to the other, providing separate current and potential connections.

In this study, the electrical resistances of the specimens were measured with a Hewlett Packard 34420A $\mu\Omega$ Meter (Figure 20) using insulated gold Kelvin clips. This meter features a resistance sensitivity of 100 nΩ and a DC voltage sensitivity of 100 pV. The reading noise is down to 8 nV$_{pp}$ as the meter is configured with low-noise input amplifiers and a highly tuned input protection scheme.

3.6. Vacuum outgassing characterization

Outgassing in a vacuum system refers to gas that is released from the surfaces inside the system that are exposed to vacuum –it is effectively a desorption process. In general, outgassing does not become a factor until the pressure in the system is 0.1 mbar (75 mtorr) or less, although the outgassing greatly varies depending on the materials involved. The intrinsic outgassing rate of a solid or liquid is the quantity of gas leaving per unit time and per unit of exposed geometric surface, or per unit mass of the sample, at a specified time after the start of evacuation. The outgassing rates of materials decrease with time exposed to vacuum, as gas is progressively removed from the material. With most materials, the outgassing rate reaches a plateau after approximately 4 hours under vacuum. Various methods such as the throughput method and its two variants, the conductance modulation method and the two-path method, the gas accumulation method, and the mass-loss measurements are available for outgassing rate measurement [119]. For measuring outgassing rates lower than 10^{-8} mbar.l/s.cm^2, the gas accumulation method and the conductance modulation method are widely used. When the former method is used to measure small outgassing rate, the test chamber is pumped to its ultimate pressure before the isolation valve is closed and the rate of pressure

rise is measured. In the latter method, the pressure difference is measured via the known conductance of the pumping orifice to obtain the outgassing rate of a sample. In this study the second method is used in the measurement, and the chamber was evacuated by a turbo pump. The gas flow and then the actual outgassing rate q_A (mbar. $l/(s.cm^2)$) are related to the pumping rate following equations

$$q_A = \frac{P_{gas}}{A} \cdot S, \tag{3-5}$$

where S is the pumping speed of the pump (L/s), P_{gas} is the partial pressure of gas species (mbar); A is the geometric surface area of the sample (cm^2).

A custom test rig at Edwards Vacuum was used in the characterization of the outgassing rate, which features a 200 mm-wide, ultra-high vacuum (UHV)-compatible SS cube chamber fitted with a 200 amu mass range reduced gas analyzer capable of measuring partial pressures as small as 1×10^{-14} mbar.

3.7. Mechanical characterization via cantilever deflection

To characterize the elastic performance of cantilevers printed using different technologies, bending tests were carried out using a Hysitron Triboindenter TI 950 (Figure 21) fitted with a 10 µm radius cono-spherical diamond tip. The instrument is capable of applying a force up to 10 mN with 1 nN resolution and measuring a vertical displacement up to 5 µm with a 0.02 nm resolution. The tests were conducted in the elastic region with a linear relationship between applied force and vertical deflection with a slope denoted as k_0

$$k_0 = F/\delta = 3E \cdot I_{cs}/L^3, \tag{3-6}$$

Figure 21 Hysitron Triboindenter TI 950

in which δ is the deflection with force F loaded at position L. E is Young's modulus, I_{cs} denotes the moment of inertia of the cross section of the beam (assumed to be constant across the beam) about the neutral axis [120]. L couldn't be measured precisely due to the difficulty of locating the cantilever roots [121]; therefore, the Young's modulus E of the 3D printed samples was calculated as

$$E = 1/(3I_{cs} \cdot b^3), \tag{3-7}$$

where b is the gradient of k_0 from the force-deflection curves produced at two or more different loading positions; this approach requires well-known relative positions of the different points of measurement.

3.8. Material characterization via uniaxial tensile tests

Uniaxial tension tests provide a simple and effective way to characterize a material's response to loading. By subjecting a sample to a controlled tensile displacement along a single axis, the change in dimensions and resulting load can be recorded to calculate a stress-strain profile. From the obtained curve, elastic and plastic material properties can then be determined. We performed tensile tests on stainless steel samples and calculated their Young's modulus, yield stress, ultimate tensile strength, and elastic strain energy density. The uniaxial tensile tests were conducted using a PASCO Materials Testing Machine (ME-8236). The built-in strain gauge transducer is capable of measuring up to 7100 N of force with a 1 N resolution, and the displacement of the load bar is measured by the optical encoder module with a resolution of 1 μm. Force data from the load cell and displacement data from the encoder module are recorded with PASCO Data Collection Software Capstone.

3.9. SEM sample preparation

Sectioning of the test samples was carefully performed to avoid altering or destroying the structure of the material. A Buehler IsoMet™ Low-Speed Precision Cutter [122], shown in Figure 23(a), capable of cutting with a ±5 μm precision, was used to section the cantilever samples to review the surface along the longitudinal direction. The tool uses gravity-fed cutting force to reduce deformation on delicate samples: the weight is applied to the work in increments of 25 grams by proper selection of the four weights supplied with the unit –the heavier the load, the greater the surface damage to the specimen. The angular speed of the spindle can be set in the 0-300 rpm range; analogous to using heavier weights, faster speeds tend to damage the specimen surface. Weight and rotation rate are chosen to provide a smooth, clean surface with optimal cutting efficiency. The IsoMet™ employs the "drag" principle of lubrication with the lubricant carried to the sample on the periphery of the blade to keep the sample cool [123]; moreover, it reduces cutting time and produces superior quality cuts as effective lubrication allows the diamond particles to cut cleanly by minimizing blade loading with the formation of discrete chips, enabling a clean release from the
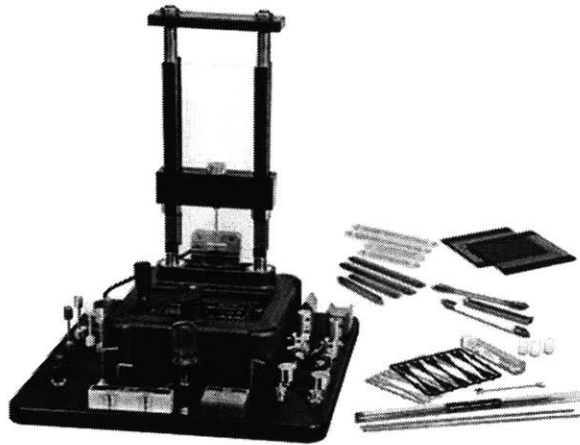
Figure 22 Pasco Materials Testing System.

blade and work surface. The small amount of possible deformation occurred on the sample surface was removed during subsequent sample preparation steps.

After the specimen is sectioned to a convenient size, it is mounted in a plastic or epoxy material to facilitate handling during the grinding and polishing steps —mounting metallographic samples helps to protect and preserve the edges during metallographic preparation, which is crucial to evaluate the surface for structural integrity [124]. Given that SS specimens are not susceptible to heat or pressure, compression mounting using Buehler Simplimet 4000 Mounting Machine (Figure 23(b)) is employed; the tool uses a mounting press to apply heat and pressure to encapsulate the sample in a mounting compound. The mounting technique provides excellent edge retention that protects and preserves the edges during the preparation process. Green PhenoCure powder is chosen as the mounting media, considering the compatibility of in terms of hardness and abrasion resistance. With the addition of copper filler, the electrical conductivity under SEM examination is ensured. The mount is allowed to cool down to room temperature under pressure before removing it from the mounting press to minimize shrinkage and improve edge retention.

The next step in sample preparation is grinding (Struers Rotopol, Figure 24 (a)) with abrasive used for each succeeding grinding operation —one or two grit sizes smaller than what was used in the preceding step to achieve a flat, smooth and scratch-free surface. The polishing step is required to remove the surface damage that occurred during sectioning and during the previous grinding step. Wet grinding with water is used to minimize specimen heating, and to prevent the abrasive from becoming loaded with metal removed from the specimen being prepared. Proper grinding removes damaged or deformed surface material, while
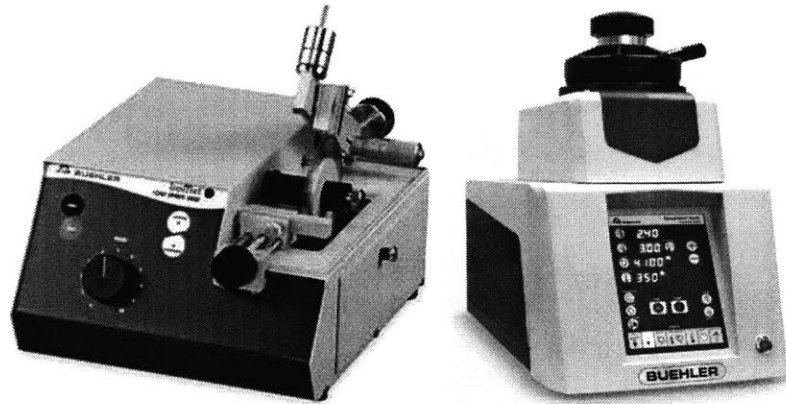
Figure 23 (a) Buehler IsoMet™ Low Speed Precision Cutter [123]; (b) Buehler Simplimet 4000 Mounting Machine [124].

Figure 24 (a) Struers RotoPol-21 polishing machine; (b) Buehler AutoMet 250 Polisher.

limiting the amount of additional surface deformation, such as enlarging or deforming the pores. The grinding process began with 240 grit silicon dioxide paper to remove burrs from sectioning and progressed through 1200 grit silicon dioxide paper for finer polishing. Much care was taken during the grinding and polishing process to not over polish or use worn out paper. Paper was changed frequently, and pressure forced on the samples was monitored. One-direction grinding was used to maintain flatness.

Mechanical polishing was performed on Buehler AutoMet 250 Polisher (Figure 24 (b)) as the final polishing step to remove any remaining thin layer of deformed metal, resulting in a smooth, reflective surface. The procedure leaves a properly prepared sample ready for examination of the unetched characteristics, such as porosity. The cloth used is magnetically attached to a rotating wheel, and the applied abrasive particles are finer successively (starts with 9 μm diamond, then continues with 3 μm diamond, and

concludes with 0.05 μm alumina in the final polishing step, listed in Table 6 [125]). Between each step of grinding and polishing, the samples are sonicated to remove abrasive and debris from the opened pores to avoid contaminating the next polishing step.

Table 6 3-Step Polishing Method for Stainless Steel [126].

Surface	Abrasive / Size	Load - lbs [N] / Specimen	Base Speed [rpm]	Relative Rotation	Time [min:sec]
UltraPad	9μm MetaDi Supreme Diamond	6 [27]	150		5:00
TriDent	3μm MetaDi Supreme Diamond	6 [27]	150		3:00
ChemoMet	0.05μm MasterPrep Alumina	6 [27]	150		2:00
= Platen = Specimen holder *Plus MetaDi Fluid Extender as desired					

4. Characterization of 3D Printed Metal Samples

Clearly, there is a need for better understanding of the properties of metal components produced via AM technologies. Therefore, we conducted a comprehensive characterization of the properties of the 3D printed samples, with the aim to identify the best manufacturing method for vacuum-compatible, detail-rich, freeform mesoscaled components. Dimensional accuracy and surface finish are the cornerstones of metal AM, especially when producing functional products that satisfy practical applications: for example, post-machining of mesoscale parts to a tight tolerance and additional polishing to a smooth surface would be time-consuming and expensive, wiping out the advantages of AM over conventional production methods. Thermal and electrical conductivities are heavily influenced by porosity and cracks; therefore, measuring these physical properties could help verify the capability of printing technologies to create relatively pore-free parts and provide insight into the manufacturing process. Given that 3D printing is and additive process, it is possible that small voids in the print, created as layers are formed, could trap gases and later gradually vent into vacuum, making the part unsuitable for high vacuum environments. Mechanical properties of 3D printed parts could be different from those of the conventional machined parts due to the complex thermal history involved in their creation. The data from this analysis demonstrate that binder inkjet printing of SS 316L has associated the smallest in-plane offset, out-of-plane offset, and eccentricity of nominally symmetric features, while showing ultra-high-vacuum compatibility and intrinsic electrical and thermal properties close to those of bulk metal.

4.1. Dimensional accuracy, minimum feature size

Geometry characterization is critical for quality control and to assess whether the deviations from the CAD design meet the required tolerance. The accuracy a printer can reach is not only determined by the printing process parameters (e.g., the size of the feedstock, the minimum diameter of the laser source or the binder jet), but also by the dimensions and geometry of the part that is printed. Here, we characterize the minimum feature size (MFS), precision, and repeatability of the printers using vertical cylinders spanning a range of diameters and heights; each of these structures is called a *resolution matrix*. The fabricated resolution matrices from each technology are shown in Figure 25 –a top view of a selected pillar with nominal diameter of 450 μm from binder inkjet printing and 500 μm from the other printing techniques is included. The heights of the substrate and the pillars are designed to be integer multiples of the layer thickness of each printer. For the DMLS SS 316L resolution matrices, the pillar diameter was varied between 300 μm and 1,600 μm in steps of 100 μm, while the pillar height was varied between 300 μm and 2,200 μm in steps of 100 μm; similarly, for the binder inkjet-printed SS 316L resolution matrices the pillar diameter was varied between 360 μm and 1,530 μm in steps of 90 μm, while the pillar height was varied between 360 μm and 2,070 μm in steps of 90 μm; likewise, for the lost-wax casted sterling silver resolution
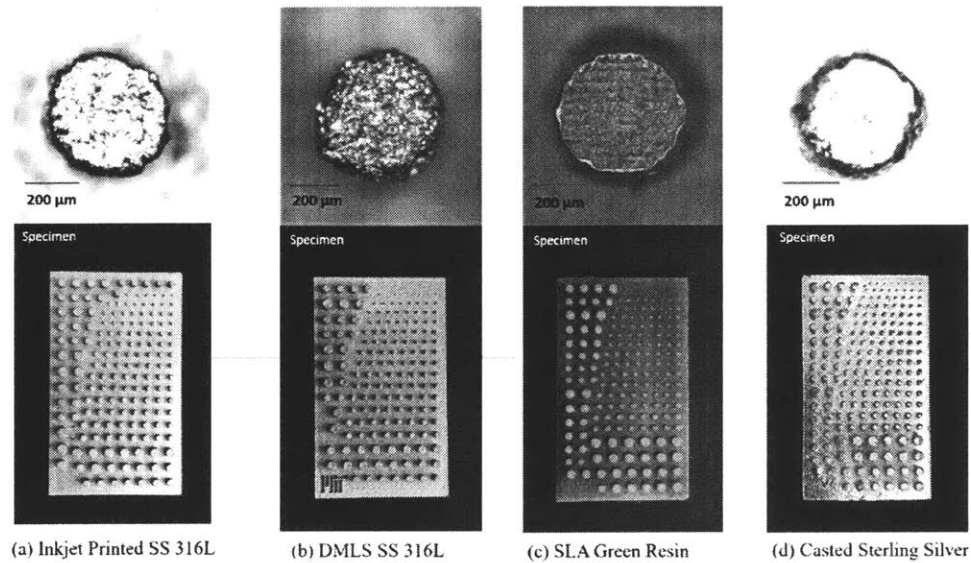
Figure 25 Fabricated resolution matrices from each technology.

matrices the pillar diameter was varied between 350 μm and 1,550 μm in steps of 75 μm, while the pillar height was varied between 350 μm and 2700 μm in steps of 90 μm. Features with dimensions larger than 200 μm were measured using a Mitutoyo Quick Vision ACTIVE 202, while smaller heights were characterized by a Leica Microsystems' research-grade microscope incorporated with the Renishaw Invia Reflex Raman Confocal Microscope system that is equipped with a motorized stage for area mapping with step sizes of 100 nm (X/Y) and 16 nm (Z). Metrology of the B9 Creator Emerald wax masters is included in the characterization to decouple the resolution issues due to the printing of the wax masters from those due to the lost-wax casting, a 3% volumetric shrinkage is accounted for during printing. In-plane dimensions are measured in two directions corresponding to the maximum and minimum diameters respectively to assess the roundness of the pillar, and results are illustrated in Figure 26. Out-of-plane dimensions refer to the height of each pillar are shown in Figure 27.

The relatively large deviation of features in the objects printed with DMLS is related to the heat transfer during printing process. After the laser source passes a spot, it returns back before the heat from the previous pass could dissipate since the part is small. The small pillars will reach a higher peak temperature during melting than a larger pillar given the constant laser power and scan speed. Besides, when printing small pillars, the material underneath is not sufficient to conduct the heat away, which further aggravates the overheating problem, leading to larger shrinkage in smaller features as illustrated in Figure 26 (b) –the
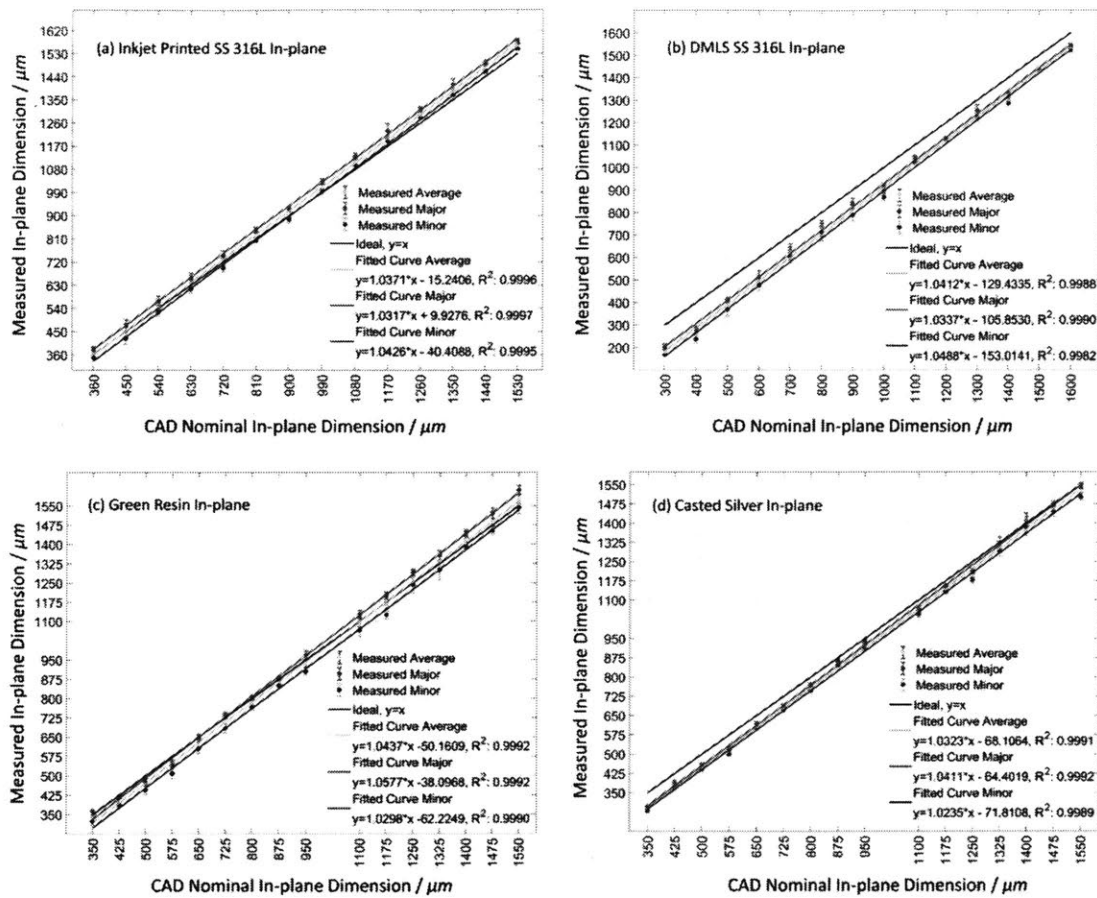
Figure 26 In-plane dimension characterization of (a) inkjet printed SS 316L; (b) DMLS SS 316L; (c) SLA green resin; (d) casted sterling silver.

deviation tends to be suppressed for larger feature sizes. In addition, the energy concentration increases the relative scale of molten pool, resulting in a less sharply defined edge. The increase in height is possibly related to the setup of the machine to prevent the shape error. Due to the strong dependence of the dimensional deviation on the feature size, compensation based on the experimental measurement of all features would be needed, which would significantly complicate the procedure to improve the dimensional accuracy of a general part as different shrinkage compensation factors would be required for each section of the CAD model.

In the casted samples of SLA-printed resolution matrix masters, the height is undersized by around 270 μm regardless the height of the pillars. Taken into account the 3% shrinkage, 10 layers are likely missing, which might be caused by the calibration of the printer. Since the height of the pillars are rather small, it is relatively easy to achieve high dimensional accuracy of the casted part in the vertical direction. In the plane

44
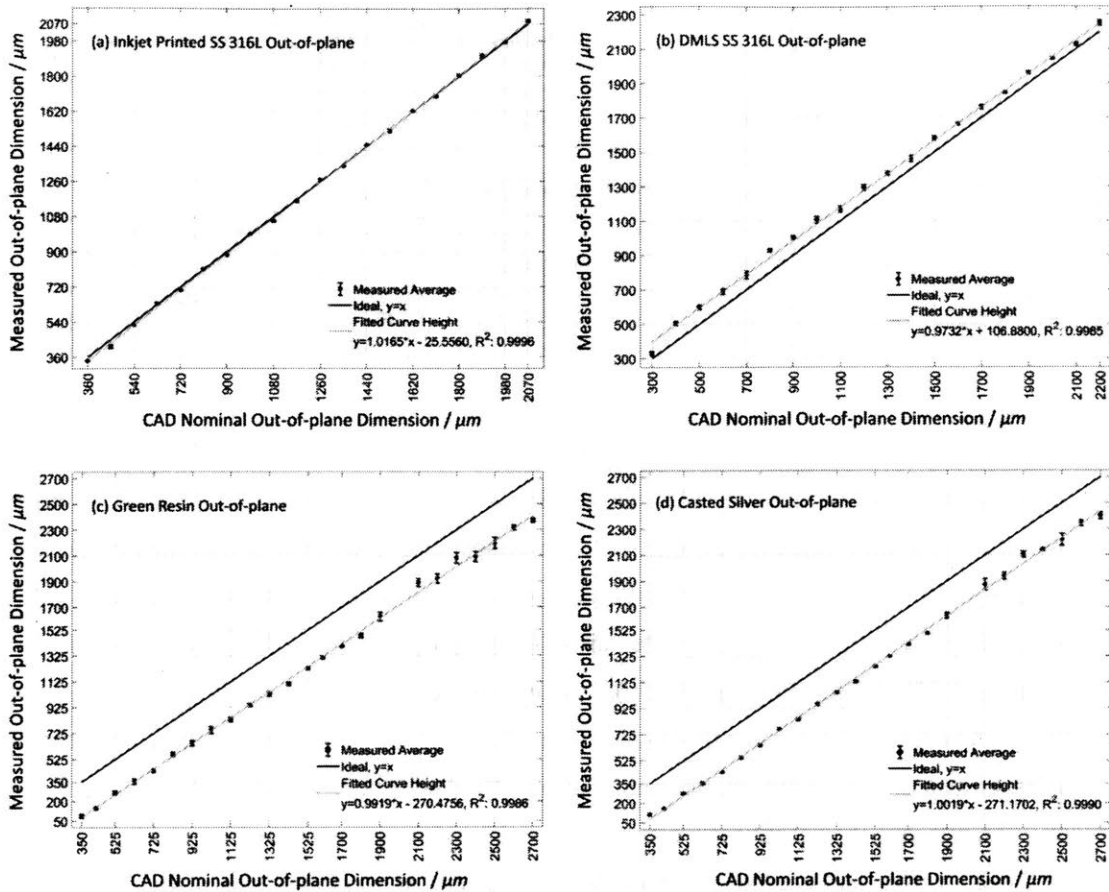
Figure 27 Out-of-plane dimension characterization of (a) binder inkjet-printed SS 316L; (b) DMLS SS 316L; (c) SLA-printed B9 green resin; (d) lost-wax casted sterling silver.

parallel to the layers, the edge of the casted pillars is severely rounded off as illustrated by the single pillar in the Figure 26(d) –the bright circle is the edge of the top surface of the pillar, while the outer rim of the dark circle is the top view of the side surface.

Binder inkjet printing displays a very high dimensional accuracy and the dimensional parameters stay within a tight deviation across the full range of dimensions included in the matrices (Figure 27 (a)). The shape of cylinders is well conformed with a straight side wall and relatively flat top surface (Figure 25(a)). In conclusion, binder inkjet printing succeeded in building accurate fine features, which is of great importance for components fabricated from stainless steel 316L since feature post-sizing becomes increasingly difficult for materials with hardness exceeds 150HV [127].

45

Table 7 Summary of Metrology 3-D Printed resolution matrices

Printing method	Material	Printed in-plane offset	Printed in-plane eccentricity	Printed in-plane MFS	Printed out-of-plane offset
DMLS	SS 316L	~1 pixel (~100 μm)	(0.294±0.133)	185 μm	~3 slices (~100 μm)
Binder inkjet	SS 316L	~0.5 pixels (~10 μm)	(0.297±0.080)	366 μm	~1 slice (~25 μm)
DLP-SLA	B9 green resin	~2 pixels (~60 μm)	(0.228±0.032)	287 μm	~9 slices (~270 μm)
Lost-wax	Sterling silver	~1.5 pixels (~40 μm)	(0.330±0.056)	340 μm	~9 slices (~270 μm)

A summary of key findings from the metrology characterization is provided in Table 7. For all printing methods characterized, the coefficients of determination of the least-squares fits suggest a linear correspondence between the printed dimensions and the corresponding CAD dimensions; also, the printed out-of-plane dimensions are closer to the corresponding dimensions of the CAD files than the in-plane dimensions (the in-plane and out-of- plane printed dimensions are on average 3.6% off and 1.7% off than the corresponding CAD dimensions, respectively). The average eccentricity across all samples is ~0.29, i.e., the cross-section of the pillars is very close to the ideal circular shape (in an ellipse with an eccentricity of 0.29, the major axis is ~2% longer and the minor axis is ~2% shorter than the radius of a circle with the same center). The data also show that binder inkjet printing of SS 316L has associated the smallest in-plane offset, out-of-plane offset, and eccentricity (variation considered) of nominally symmetric features; in addition, the cylinders made with this technique had straight sidewalls and fairly flat top surfaces. Although the DMLS technique produced smaller features due to the significantly larger offset, the edges of the printed parts were less sharply defined compared to the samples made with binder inkjet printing. The values in Table 7 for the lost-wax micromolded parts and the DLP-SLA wax masters are about the same, suggesting that the lost-wax process minimally distorts the CAD geometries after the changes caused by the wax masters; however, unlike the wax samples, the edge of the lost-wax micromolded pillars was severely rounded off (due to surface tension, the solidifying metal is not fully conformed to the sharp corners defined in the mold by the wax master; in addition, heat concentrates at the small volume of molten material located in the corners, limiting the heat transfer from the melted metal to the mold, creating localized areas with low solidification rate).

4.2. Electrical and thermal characterization

For metals, the thermal and electrical conductivities are heavily influenced by porosity and cracks in the microstructure. Therefore, characterizing these physical properties on printed samples could provide

insights into the internal structure of the printed materials. Also, in many cases, the applications that can be satisfied with a given AM method strongly depend on how close the intrinsic values of the printed material are to those of the bulk material.

4.2.1. Electrical resistivity characterization

The electrical resistivity ρ_e of the printed metal rods was calculated from the slope of the resistance vs. length data plot via

$$R = \rho_e \cdot l/A_c + R_0,$$

(4-1)
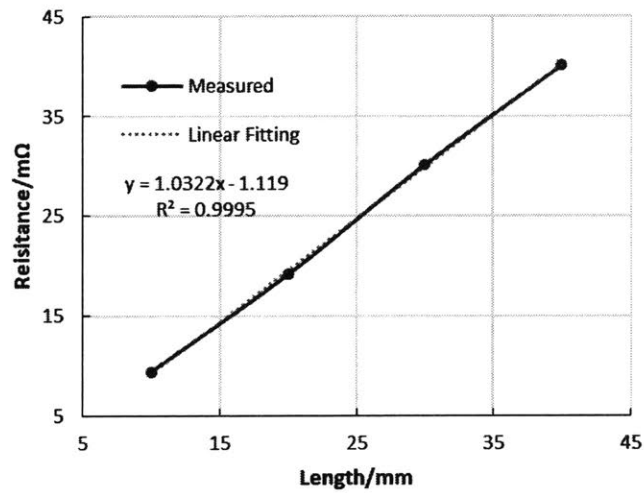
Figure 28 $R - l$ Curve of an inkjet binder-printed SS 316L rod.

Table 8 Electrical resistivity of SS 316L and sterling silver samples.

Sample		Electrical Resistivity ($\mu\Omega\cdot$cm)
SS 316L	ESPI	72.593±0.039
	DMLS	72.096±0.516
	Binder inkjet	78.356±1.456
Sterling silver	ESPI	2.128±0.067
	Lost-wax	4.801±0.215

where A_c, l, and R are equal to the area of the cross-section of the rod samples, the length of the rod samples, and the resistance of the rod samples, respectively, and R_0 is equal to the contact resistance. R was directly

measured with the 4-wire Kelvin apparatus previously described using a Hewlett Packard 34420A nV, $\mu\Omega$ meter. The printed rods had 1 mm diameter and were 45 mm, 65 mm, and 60 mm long for binder inkjet-printed, DMLS, and lost-wax casted samples, respectively; the electrical resistivity of the bulk material was measured for comparison using 1 mm diameter and 65 mm long rod samples (ESPI metals, Ashland, OR, USA). To eliminate the influence of the contact resistance from the mating connectors on the estimate of the electrical resistivity, resistance measurements at different clip separations were made using each rod. The R - l curve of the inkjet binder-printed SS 316L rod sample is shown in Figure 28, while the experimental results are summarized in Table 8. The electrical resistivity of the printed SS 316L samples is close to the bulk value, suggesting that the DMLS and binder inkjet-printed SS 316L samples are relatively free of internally porosity and cracks. In contrast, the electrical resistivity of the lost-wax sterling silver sample is twice that of the bulk metal; this result is surprising, it was expected that the lost-wax process would yield pore-free samples with near-bulk properties. The reason for the large discrepancy needs to be further studied as experiments showed no significant decrease in mass density, or contamination of the samples.

4.2.2. Thermal conductivity characterization

Conducting a direct measurement of the thermal conductivity of a metal sample is relatively difficult because we need to know very well the heat flux across the sample; however, measuring thermal diffusivity is comparatively less challenging [116]. The thermal conductivity κ as a function of the thermal diffusivity α is given by

$$\kappa = \alpha \cdot c_p \cdot \rho, \tag{4-2}$$

where c_p is the specific heat and ρ is the mass density. The thermal conductivity at room temperature of metal printed samples was estimated by measuring α via the laser flash technique described in Chapter 3 with a Netzsch LFA 457 MicroFlash. The 2 mm-thick and 12.4 mm diameter samples were pre-coated with graphite to increase heat absorption; for comparison, α of the bulk material was also characterized using similarly shaped samples (ESPI metals, Ashland, OR, USA). The experimental estimates of the thermal conductivity of the samples are summarized in Table 9; in these estimates, c_p was assumed equal to published values, and ρ was estimated by measuring the weight and volume of each sample with a precision balance and a micrometer, respectively. The thermal conductivity of printed SS 316L is roughly the same for both printing technologies and comparable to the bulk value. However, the thermal conductivity of lost-wax sterling silver is slightly lower to that of the bulk material, which may be related to the low conductivity of the graphite coating. Since the spot of laser is smaller than the specimen, the porosity distribution plays

Table 9 Measured Thermal Conductivity of SS 316L and sterling silver samples.

Sample		Thermal Conductivity (W/(m*K))
SS 316L	Nominal	16.2
	ESPI	16.911
	DMLS	13.568±0.281
	Inkjet Printed	14.689±0.184
Sterling silver	Nominal	361
	ESPI	307.391
	Casted	290.870±12.930

a role in measuring the thermal diffusivity –further studies should be conducted to elucidate whether the porosity distribution is correlated with the thermal conductivity estimates.

4.3. Vacuum outgassing characterization

The vacuum outgassing of samples made with the three studied AM methods was characterized to assess the suitability of these manufacturing technologies for vacuum applications. Several of the MEMS applications satisfied by mesoscale metal structures require vacuum to operate, e.g., mm-wave vacuum amplifiers, THz wave generators, and mass filters [17], [18], [128]. Porosity is a common concern in metal AM [41]; it is possible that small voids within the printed part could trap gases, which later, gradually, vent into vacuum, increasing the background pressure.

The vacuum outgassing of DMLS-printed SS 316L, binder inkjet-printed SS 316L, and lost-wax casted sterling silver samples was measured using a custom testing rig. The system is pumped by a 68 l/s dry rough pump/turbo combo capable of reaching 10^{-10} mbar ultimate pressure (if baked). The samples tested are printed flat plates with nominal surface area equal to 96 cm^2 for SS 316L and 80 cm^2 for sterling silver. Measurement of the outgassing rates was conducted every ten minutes for over 10 hours. The residual gas analysis at 10 hr are shown in Figure 29, and a summary of the experimental results at 1 hr and 10 hr are provided in Table 10. As expected, most of the outgassing is water (the samples were not baked in vacuum). The outgassing rate of DMLS SS 316L is the smallest of the three samples, followed by lost-wax sterling silver (~1×10^{-10} mbar.l/(s.cm^2) and 4×10^{-10} mbar.l/(s.cm^2), respectively, after subtracting the contribution

of water vapor in the outgassing). Nonetheless, the water-free outgassing rate of binder inkjet-printed SS 316L is adequate for UHV applications [129].

(a) Inkjet printed SS 316L

(b) DMLS SS 316L
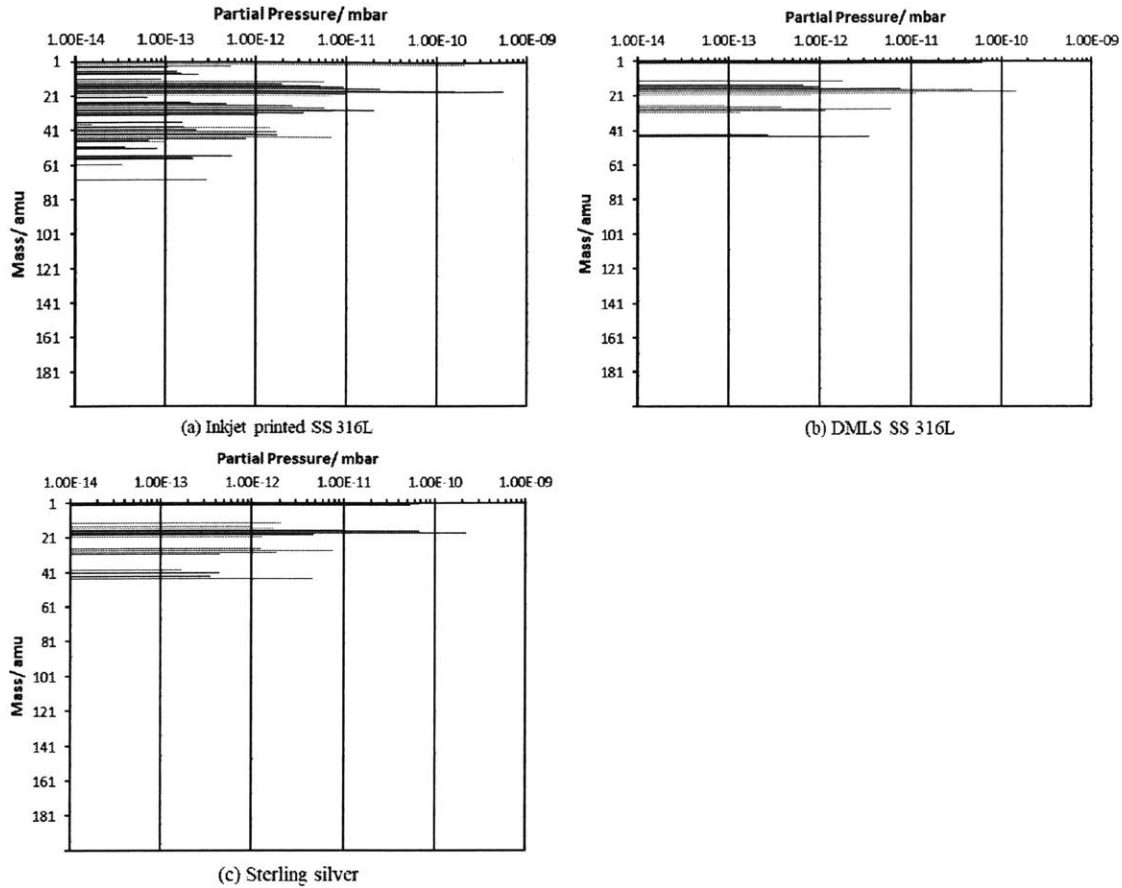
(c) Sterling silver

Figure 29 Residual gas analysis of materials in the chamber after pumping down for 10 hours, (a) binder inkjet-printed SS 316L; (b) DMLS printed SS 316L; (c) lost-wax casted sterling silver.

Table 10 Outgassing rate of 3-D Printed metal samples

| Sample | Outgassing rate $\times 10^{-9}$ mbar.l/(s.cm^2) | | | | | |
| | 1 hour | | | 10 hours | | |
	Total	H_2O	C_xH_y	Total	H2O	C_xH_y
Binder inkjet (SS 316L)	54	37	0.26	7.2	3.5	0.018
DMLS (SS 316L)	14	5.3	0.15	1.3	1.2	0.0044
Lost-wax (sterling silver)	27	15	0.18	2.8	2.4	0.004

4.4. Mechanical and surface texture characterization

To assess the capability of the three metal AM techniques studied to creating free-standing structures, cantilevers were produced; their surface morphology and Young's modulus were measured to evaluate the influence of printing orientation on dimensional accuracy, surface roughness and mechanical properties. Cantilevers are transducers commonly used in miniaturized systems for sensing [130], switching [131], vibration energy harvesting [132] and other applications. Fabrication of overhanging structures layer by layer often surfers the problem of deformation caused by residual stress [133] and the layer-wise manufacture of the part often leads to inherent anisotropy [134], [135]. Besides, as stated by Niendorf[136], for feature sizes smaller than 650 μm, sample geometry and the overall sample dimension have pronounced influences on the evolution of the microstructure due to heat flow phenomena, strongly affecting the mechanical performance. There are reports in the literature of 3-D printed metal MEMS cantilevers. For example, Lam and Schmidt reported 50 μm to 100 μm wide, 2.8 μm tall, and 500 μm long cantilevers made by inkjet printing of silver nanoparticles, followed by laser trimming [137]. Also, Park et al. demonstrated MEMS mechanical switches based on 100 μm wide, 1.6 μm tall, and 500 μm long inkjet-printed silver nanoparticle cantilevers [138].

Cantilevers with length equal to 5 mm, height between 450 μm and 675 μm, and width between 300 μm and 630 μm were fabricated in SS 316L via binder inkjet printing. The specimens were printed in two directions, that is, the neutral axis of the cantilever was either parallel (i.e., *horizontally printed*) or perpendicular (i.e., *vertically printed*) to the printed layers. The cantilevers were printed monolithically attached to a rigid frame. The horizontally printed cantilevers were oriented upside down to eliminate the need for support structures (in other words, the tops of the horizontally printed cantilevers directly touched the build plate). The surfaces of the DMLS specimens were left in as-printed condition due to limited polishing path caused by the severe wrap. Binder inkjet-printed SS 316L specimens were post treated with blasting using small and gentle media, while lost-wax casted sterling silver specimens were slightly tumble polished.

4.4.1. Cantilever neutral axis deviation characterization

The deflection of the neutral axis of the cantilever specimens was characterized with a Mitutoyo Quick Vision ACTIVE 202, the findings are summarized in Table 11. The significant wrap-up (bending towards the laser beam) of the DMLS cantilever beams is due to the residual stress introduced by the steep temperature gradients [139] due to the rapid heating up of the interaction spot and low heat conduction of the material. Given that the expansion of the upper layer is restricted by the underlying material, the heated top layer would be plastically compressed. During the cooling process, the plastically compressed upper layer starts to shrink and finally the thin beam is angled towards the building direction [139]. The printing

Figure 30 SEM micrographs of cantilevers: binder inkjet-printed, SS 316L, horizontal neutral axis, lateral side (a) and top side (b); binder inkjet-printed, SS 316L, vertical neutral axis, unpolished lateral side (c) and top side (d); binder inkjet-printed, SS 316L, vertical neutral axis, polished lateral side (e) and top side (f); DMLS, SS 316L, horizontally printed, unpolished lateral side (g) and top side (h); DMLS, SS 316L, vertically printed, unpolished lateral side (i) and top side (j); lost-wax casted sterling silver, polished lateral side (k) and top side (l).

Table 11 Deviation of cantilever neutral axis at the tip of the cantilever

Sample		Deviation (mm)
Binder inkjet 316L	Horizontal, polished	0.1969±0.0494
	Vertical, unpolished	0.2321±0.0383
	Vertical, polished	0.2166±0.0350
DMLS 316L	Horizontal, unpolished	0.3401±0.0475
	Vertical, unpolished	0.4189±0.0700
Casted sterling silver	Vertical SLA resin mold, polished	0.3572±0.0467

DMLS printed samples have a higher distortion attributing to the lack of support when scanning a large number of layers. Furthermore, scanning track reduction results in a quick reheat of previously molten tracks and rapid exposure of the entire beam layer, which causes the temperature of the upper layer to remain high. Given that heat transfer directly down to the solidified underlying layers is more likely to occur than to the surrounding loose powders, the small size of the solidified underlying layers makes the cantilever less resistant to thermal shock, which could magnify the effect. As for sterling silver cantilevers, besides the high malleability and ductility of sterling silver, the curl of sterling silver cantilevers partially stems from the warping of the resin mold as a result of the non-uniform internal stresses developed during the formation of the polymer bond and the exothermic chemical reaction during photo-polymerisation [73]. Binder inkjet-printed samples display a much lower deformation (~2° angular deviation) because no differential temperature is applied during printing process, and the heating occurs to the whole part during the sintering.

4.4.2. SEM inspection

SEMs (Tabletop Microscope TM3030) of the lateral and top surfaces of cantilevers made with each of the AM methods studied are shown in Figure 32. For SS 316L printed samples in the as-fabricated condition, the layering and the hatching line are not visually apparent on the lateral surfaces (Figure 32 (d), (g), (j)) and top surfaces (Figure 32 (c), (h), (i)). Discrete bumps and surface voids are noticeable within the conglomeration of sintered SS particles (Figure 32 (c), (d)). After polishing, it is obvious that both the size and amount of defects in vertically inkjet binder-printed sample (Figure 32 (f)) are greater than the horizontally built sample (Figure 32 (b)) which arise from the interlayer pores; however, the edges and corners of the vertically printed cantilevers are clearly sharper. DMLS-printed surfaces display different features: a coarsely scaled texture where many pores linked together forming microcracks, and the corners

of the cantilever's cross-section are rounded. Sharp edges could not be resolved when casting in sterling silver (Figure 32 (k), (l)). This could be explained as follows: heat concentrates at the small volume of mold media located at the corner, limiting the heat transfer from the melted metal to the mold, creating localized areas with low solidification rate; due to surface tension, the solidifying metal is not fully conformed to the sharp corners. Of all the printing methods and neutral axis orientations, vertical inkjet binder-printed SS
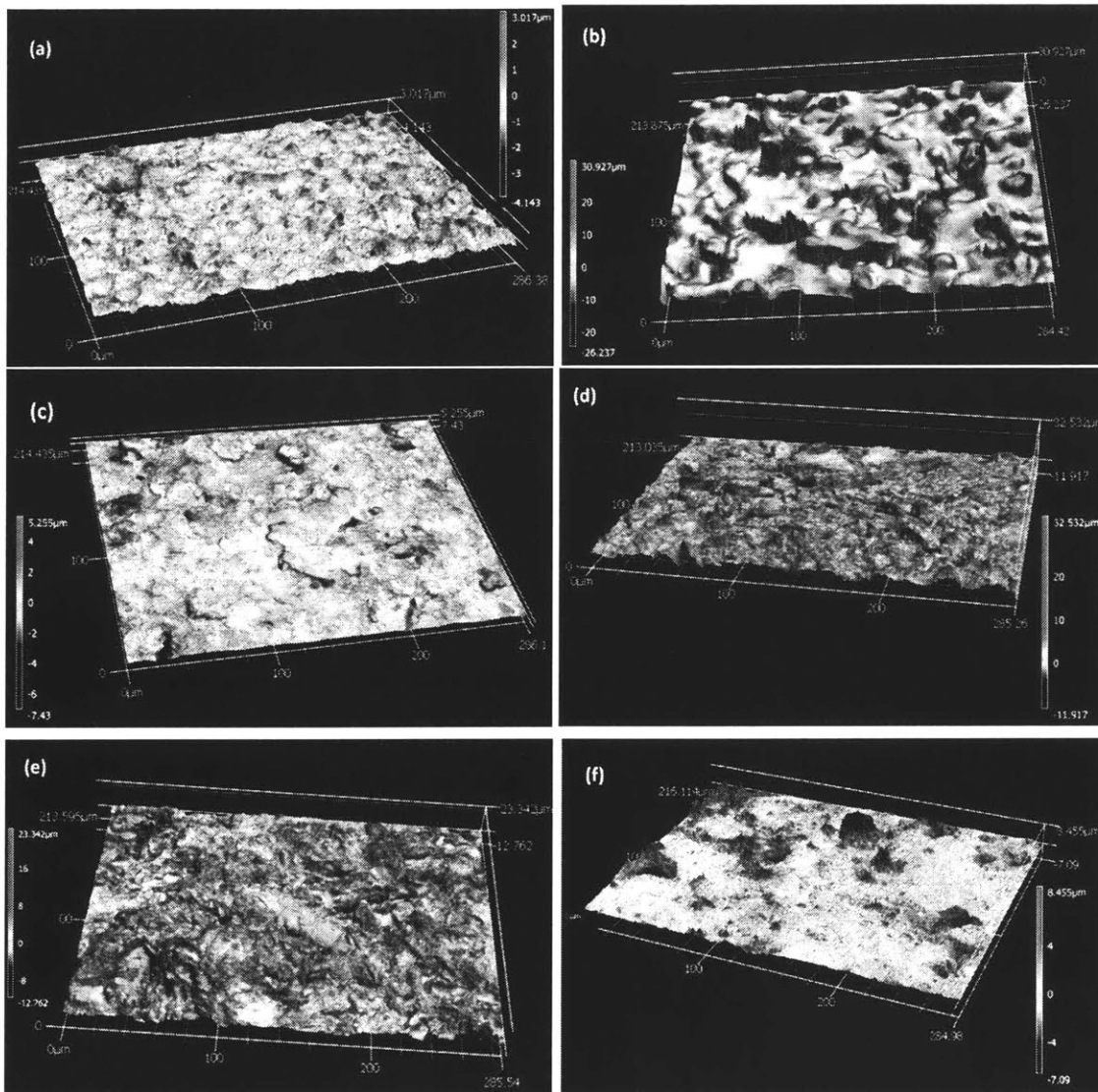
Figure 31 3D topography of 3D printed cantilevers: horizontally inkjet printed, polished (a); vertically inkjet printed, unpolished (b); vertically inkjet printed, polished (c); horizontally DMLS, unpolished (d); vertically DMLS, unpolished (e); sterling silver casted from vertically printed mold, polished (f).

Table 12 Surface roughness of 3D printed metal cantilevers: arithmetic average roughness and root mean square height.

Sample		Sa (μm)	Sq (μm)
Binder inkjet	Horizontal, polished	2.299	3.015
	Vertical, unpolished	6.483	7.705
	Vertical, polished	2.584	3.577
DMLS	Horizontal, unpolished	6.112	7.744
	Vertical, unpolished	6.663	8.386
Lost-wax casted	Vertical SLA resin mold, polished	6.034	9.287
	Smooth portion picked for bending test	2.141	2.869

316L cantilevers had the straightest faces (Figure 32 (d)) with the most precise rectangular cross sections with crisp corners (Figure 32 (c)).

4.4.3. Surface texture characterization

The surface roughness of the cantilevers was measured following ISO 25178-2 [140] using a 3D Laser Scanning Confocal Microscope VK-X250 with Nikon 20X objective lens. The whole surface of each cantilever was sampled to conduct the analysis of surface roughness. Table 12 gives the mean values of surface roughness in terms of the arithmetic average roughness S_a and the root mean square roughness S_q. 3D images under Nikon 50X objective lens of the typical surface profiles for each category are shown in Figure 31. In the as-fabricated condition of the vertically binder inkjet-printed specimen, high points are evident amid the nodular sintered powder particles; polishing effectively smooths high points, but the low pooled regions are still evident compared with the horizontally built specimen, which may relate to the insufficient fusion between layers, and this leads to slightly higher roughness of vertically built cantilevers. Discrete and small-scale bumps are more obvious on horizontally built cantilevers; the vertical counterpart has more linked, coarsely scaled sintered powders. Most of the materials appeared to be completely fused, with no laser traces or segregated beads of powders evident on the surface. Vertically and horizontally printed DMLS specimens displayed similar features with pores linked together forming microcracks. Higher surface roughness from the vertically fabricated samples could be attributed to the *staircase shape effect* during the DMLS process [141].

4.4.4. Defects characterization

Defects in AM components are hard to avoid, which to a great extent deteriorate the materials' mechanical properties and vacuum compatibility. In the binder inkjet printing process, the organic additives present in the binder that momentarily holds together the green part are complete burned out during sintering, causing the solid particles to stick together and consolidate into a rigid body. Sintering is a thermal process that creates inter-particle welds; sintering of the green parts that are binder inkjet -printed is a solid-phase sinter process, i.e., bonding of particles occurs at a temperature below the melting point by solid-state atomic transport events [142]. Specifically, particles are sintered by atomic motions driven by the release of high surface energy associated with the particle surface area [142]. During the sintering progresses, the contact points between particles enlarge and merge to form grain boundaries, which grow to replace the solid-vapor interface –lowering the total free energy of the system. Prolonged sintering causes sintered particles to coalesce. Several variables influence the porosity after sintering, including the tap density, particle dimension distribution, particle shape, sintering atmosphere, temperature, time, and heating rate [142], while the final coalescence of all the sintered particles is seldom reached.

In this characterization, we examined several defects including unmelted particles, pores, cracks, and layer separation in the samples. The appearance of these defects depends on their orientation with respect to the printing direction. In this study, defects characterization is carried out on polished longitudinal surfaces, i.e., sectioned along the axis of the cantilever beam; the bulk area on the right- and left-hand side of the cantilever are included for comparative study. Since the cantilevers are too thin to remain in their original shape after cutting, the section was done on a bulk area parallel to the axis of the beam, and the longitudinal surface was revealed by subsequent grinding the mounted sample. The polishing was done following the method discussed in Section 3.9; great care was paid during the preparation of the samples since the pores can easily carry abrasives and be smeared. It is of great importance to open the smeared pores via polishing to reveal their true shapes and amounts [143]. The polished surfaces were examined using a Tabletop Microscope TM3030.

Unmelted particles can form in between the melt pool boundaries and at the edges of the melt pools. However, in this research no unmelted particles were found. Cracks are another possible defects – especially in DMLS. Cracks may arise from residual thermal internal stresses due to the large temperature gradients and fast cooling rates during sintering. Moreover, cracks can form at the melt pool edges or at the boundaries of melt pools because during laser sintering, the melt pool is in liquid state and the boundary or edges are in solid/liquid state, which leads to thermal mismatch due to different shrinkage rate of the melt solidification and the surrounding powder matrix, causing these cracks. However, these micro-cracks are

not formed in the examined specimens. The most prominent defects in the binder inkjet-printed and DMLS-
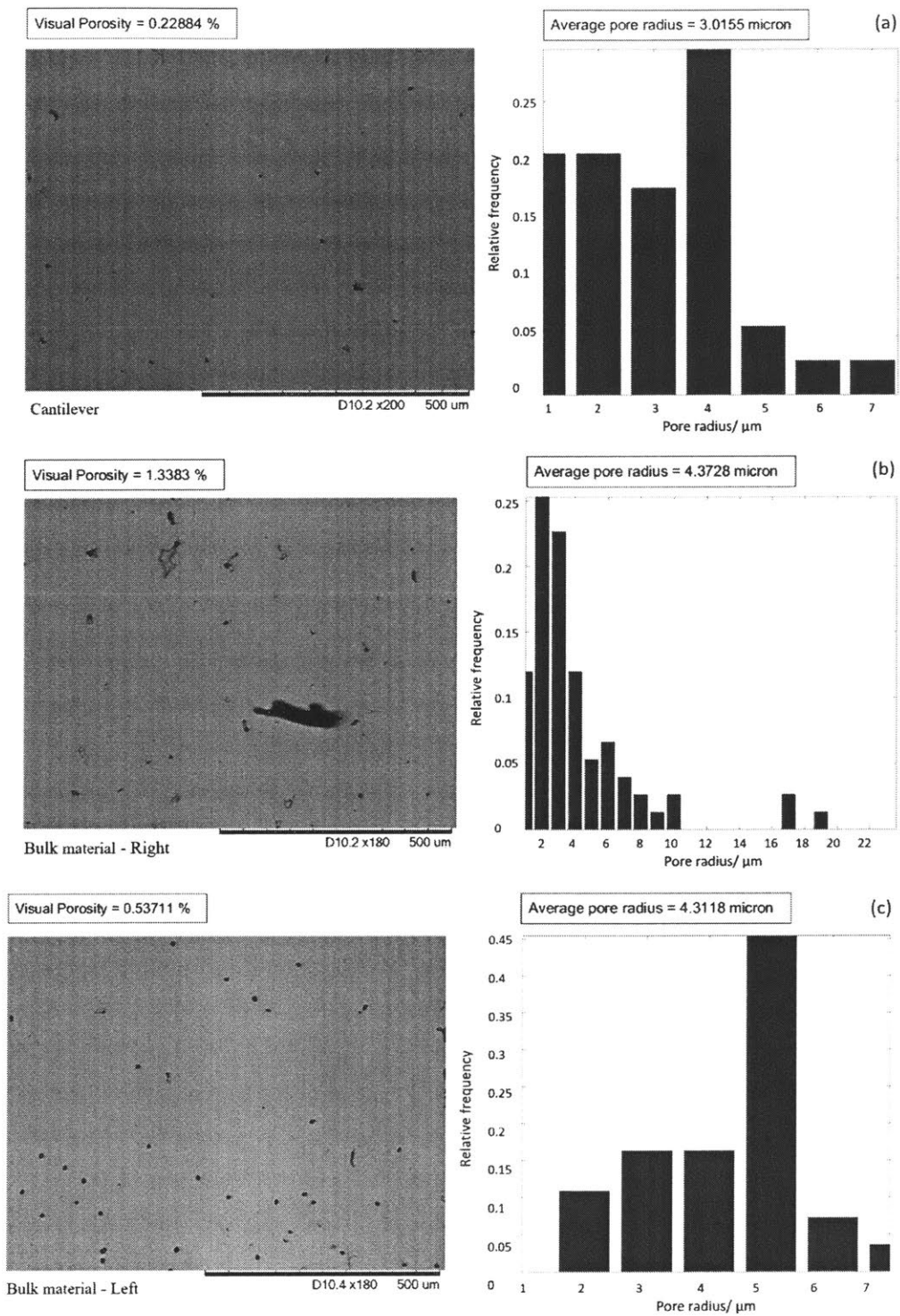
Figure 32 Pore morphology and distribution of the longitudinal surface of binder inkjet-printed SS 316L samples.

printed samples in this research are porosity and unfilled voids.
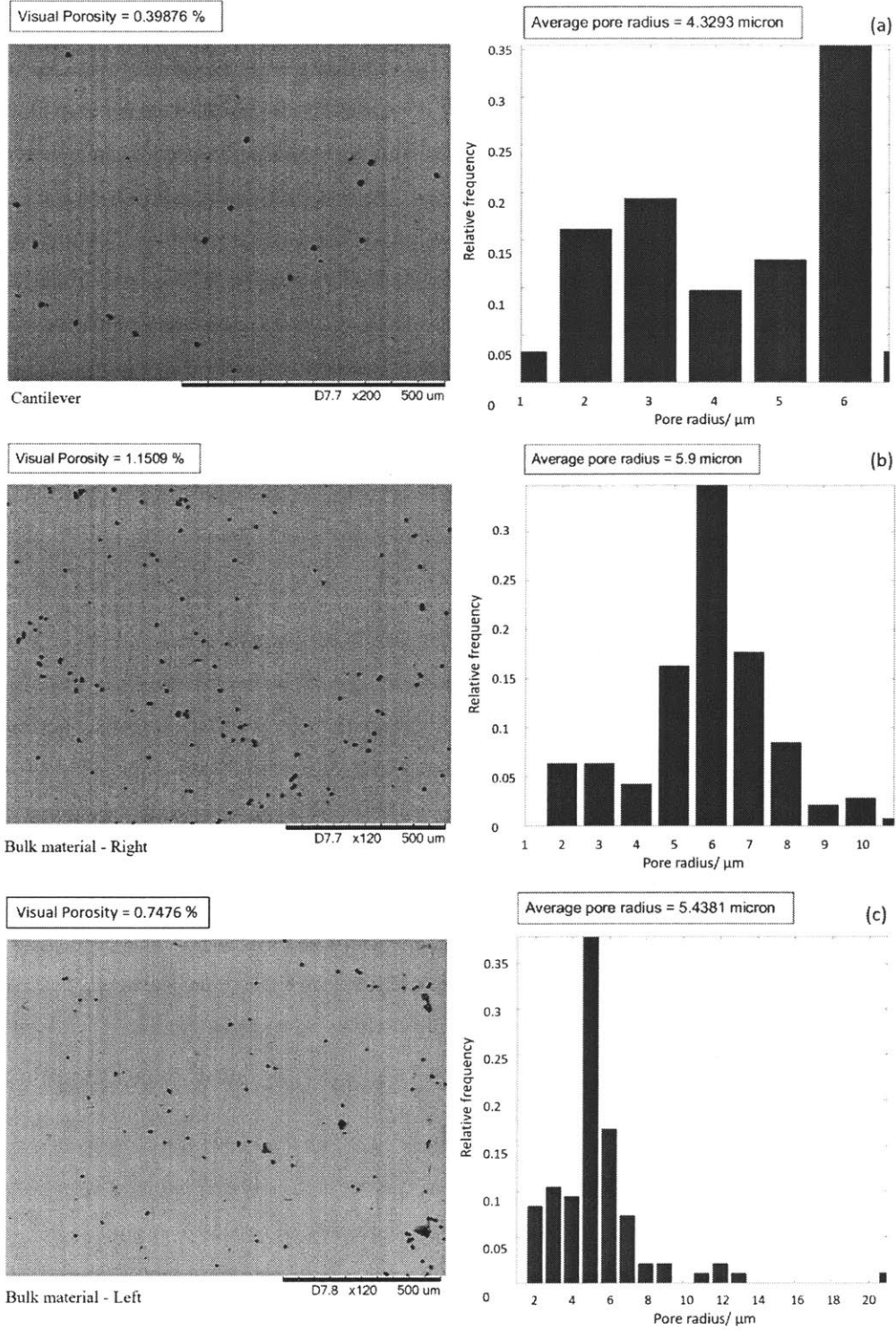
Figure 33 Pore morphology and distribution of the longitudinal surface of DMLS SS 316L samples.

Table 13 Porosity fraction and average pore size of specimens fabricated via binder inkjet printing and DMLS printing.

Specimens			Fraction of porosity (%)	Average pore radius (μm)
Cantilever beam		Binder inkjet-printed SS 316L	0.217 ± 0.094	3.454 ± 0.629
		DMLS-printed SS316L	0.376 ± 0.388	3.758 ± 0.382
Bulk area	Right	Binder inkjet-printed SS 316L	0.376 ± 0.388	3.386 ± 0.600
		DMLS-printed SS316L	1.035 ± 0.544	5.498 ± 0.526
	Left	Binder inkjet printed SS 316L	0.932 ± 0.757	4.579 ± 0.218
		DMLS-printed SS316L	0.737 ± 0.347	5.160 ± 0.441
	Average	Binder inkjet-printed SS 316L	0.654 ± 0.134	3.983 ± 0.101
		DMLS-printed SS316L	0.856 ± 0.087	5.295 ± 0.096

The surface porosity characterization was carried out in MATLAB using the city-block distance function and the watershed segmentation algorithm assuming pores as spheres and throats as cylinders [144]. The distance function expressed in city-block forms creates angular and cubical contours that intersect with curved pore walls in explicit boundaries, leading to better and clearer pore-throat differentiation; after median filtering for noise removal, segmentation was performed using the watershed algorithm to detect throats and consequently to differentiate pores, thus generating the pore network. The overall porosity and the pore size distribution are shown for binder inkjet-printed and DMLS-printed SS 316L specimens in Figure and Figure 33, respectively. Voids, as those shown in Figure (b), can originate from hard agglomerates inside the starting powder and/or insufficient powder packing before the melting process. Some of the pores are formed in between each powder granule, establishing closed pores and connected pores, i.e., open porosity as can be seen in Figure 33 (c).

The area fraction of porosity and pore size are summarized in Table 13. The bulk area, in general, has higher porosity ratio and larger pore size, and pore clusters are easily formed on the bulk areas of DMLS surfaces. Inkjet binder-printed samples have less pores compared with DMLS samples, but the pore sites are preferentially distributed on one side of the bulk samples which is abnormal. In both cases the pores are relatively small and spheroid is shape, and are unevenly distributed overall polished section; there are areas free of any visible defects.

4.4.5. Young's modulus characterization via cantilever deflection

To characterize the mechanical performance of the cantilevers printed with different technologies, bending tests were carried out using a Hysitron Triboindenter TI 950 fitted with a 10 μm radius cono-
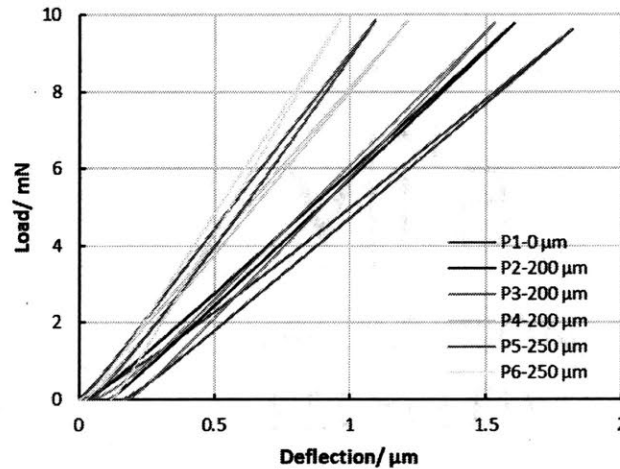
Figure 34 Load-deflection curve of the binder inkjet-printed SS 316L cantilever beam with a nominal 450×360 μm cross-section, the separation between loading positions is 200 μm, 200 μm, 200 μm, 250 μm, and 250 μm, respectively. The slope k_o is calculated as the average of the loading and unloading slopes.
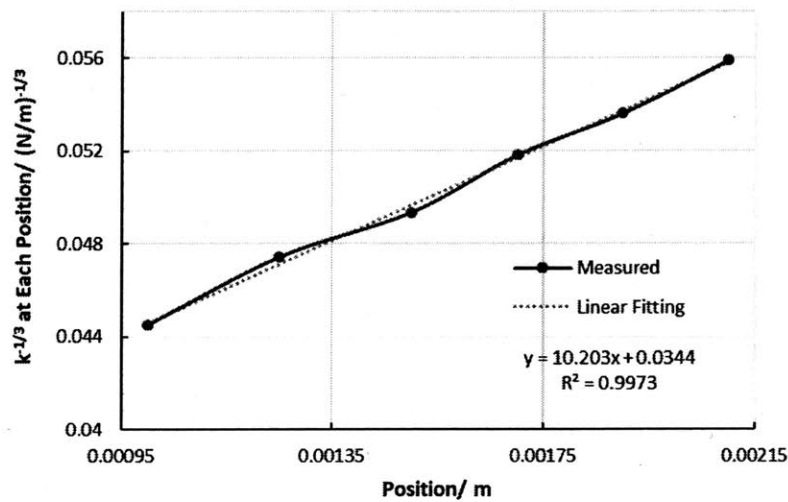
Figure 35 Inverse of cubic root of spring constant vs. distance of application of the load for a SS 316L binder inkjet-printed cantilever with 450 μm × 360 μm cross-section; starting at a point about 1 mm from the fixed end of the beam, the separation between each loading position is 200 μm, 200 μm, 200 μm, 250 μm, and 250 μm, respectively. From the slope of the linear, value of E determined from the averaged slope is 179.4 GPa.

spherical diamond tip. For each printed method, three specimens were tested, loading force at several positions along the central axis of the beam with well-known relative separations. The experiments were conducted under an open-loop mode with a 20 s loading-unloading cycle. Due to the distortion of the cantilever beams with respect to the horizontal plane (Table 11), on each point where the load was applied the zero-deflection height was reset. The scale of the roughness is very small compared to the dimensions of the beam, so the effects on the extraction of Young's modulus due to the deviation of the moment of inertia of the cross-section is negligible. No acceptable data were captured for the unpolished DMLS and unpolished vertically binder inkjet-printed cantilevers because the resetting of the zero-deflection height proved challenging and because the complex topography of their surfaces lead to tip sliding. The significant distortion of the DMLS beams posed difficulties in polishing the surface, making the bending test inapplicable; from this point of view, binder inkjet printing is preferable when manufacturing intricate contours like overhanging beams in the micro and mesoscales. For the lost-wax casted sterling silver cantilevers, although the overall surface roughness is high (Table 12), there is a small relatively smooth portion near the free end of the cantilevers on which the bending tests were conducted.

For the relatively smooth samples, a typical force-bending diagram is shown in Figure 34, which clearly shows a linear relationship between applied force and vertical deflection with a slope denoted as k_0, I_{cs} is assumed to be constant across the beam [120]. The tests were conducted in the elastic region because the deflection is recovered after unloading. The length of the cantilevers couldn't be measured precisely due to the difficulty of locating their root [121]; therefore, the Young's modulus of our 3D printed samples was extracted from the gradient b of the spring constant k_0 from the force-deflection characteristics produced at different loading positions with well-known relative separations. The determination of the

Table 14 Measured Young's modulus (GPa) of binder inkjet-printed SS 316L and lost-wax casted sterling silver cantilever beams

Sample		Young's modulus (GPa)
SS 316L	Nominal [180]	193
	Horizontally Inkjet Printed	185.35±1.89
	Vertically Inkjet Printed	174.40±1.98
Sterling silver	Nominal [181]	75
	Casted	58.63±8.97

gradient b is shown in Figure 35 for each k_0 obtained from Figure 34. The average measured Young's moduli for each printing technology are listed in

Table 14. The actual moment inertia obtained from SEM images was used in the calculation, the cross-section was approximated by a rectangle with rounded corners for specimens without sharp corners.

Specimens produced in the vertical orientation via binder inkjet printing demonstrated an elastic modulus (174.40 GPa) slightly lower than that of the beams fabricated in the horizontal orientation (185.35 GPa), but both are close to the bulk value (193 GPa). Vertically produced cantilevers are subjected to bending stresses perpendicular to the build planes, and the process of building massive number of thin, discrete layers is prone to form more interior microcracks. The intrinsically low strength between layers is believed to be responsible to the drop. Lower Young's modulus in the sterling silver samples could be explained by the nonuniformity of I_{cs} along the beam. In our calculations I_{cs} is derived from the area of the end surface, which has the largest cross-section along the beam, thus generating I_{cs} higher than the actual moment inertia. Larger data spread due to specimen-to-specimen variations shown in sterling silver test pieces arises from the geometrical inaccuracy of the beams.

4.4.6. Mechanical characterization of DMLS-printed samples via uniaxial tensile tests

In order to complete the mechanical characterization of the printed samples, we conducted uniaxial tensile tests on the DMLS parts using a PASCO Materials Testing Machine (ME-8236). Three tensile bars with 1.3 mm thick, 2 mm wide and with an initial gauge length of 26.5 mm were printed directly and not cut from a block of DMLS material. Those specimens were built flat in the X/Y-orientation, so all the tensile tests were performed in the direction of the layers. Mechanical polishing was performed before the tensile test. Tests were executed with a displacement rate of approximately 10 mm/min.
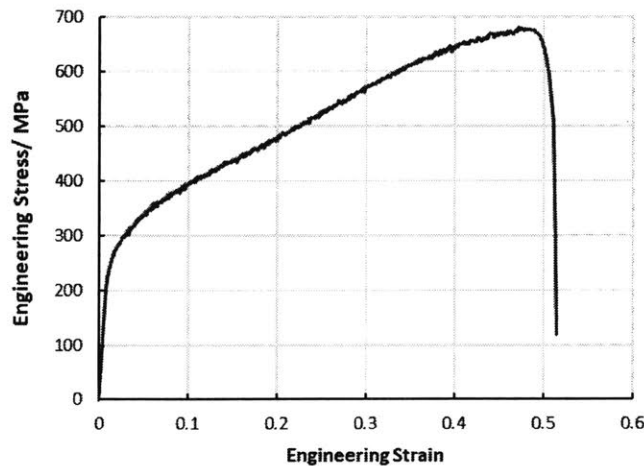
Figure 36 Typical engineering stress-strain curve of a DMLS-printed SS 316L specimen.
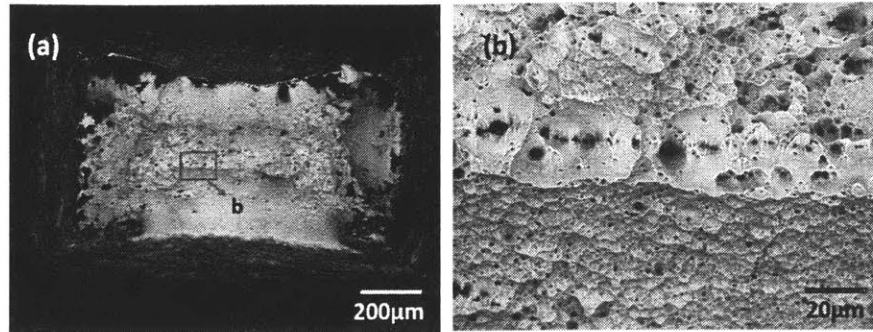
Figure 37 Failure surfaces of a DMLS-printed SS 316L uniaxial tensile test specimen: (a) apparent necking; (b) dimples can be seen, indicating ductile fracture.

Table 15 Mechanical properties of DMLS-printed specimens

Mechanical Property	Annealed [145]	DMLS
Yield Strength (MPa)	290	273.93±27.81
Young's Modulus (GPa)	193	24.47±0.97
Ultimate Tensile strength (MPa)	627	711.31±26.79
Elongation at break (%)	55	53.03±3.02

A representative engineering stress-strain curve of the DMLS specimens is shown in Figure 37. DMLS-printed SS 316L appears much less stiff, revealing a Young's modulus an order of magnitude lower than the bulk material. DMLS-printed SS 316L specimens experienced gradual yielding in response to tensile deformation, and exhibited extensive elongation before fracture –similar to annealed SS 316L [145]; the DMLS-printed SS 316L samples hardened and reached an ultimate tensile strength (UTS) higher than that of the typical annealed material; finally, the samples failed producing nearly the same ductility of bulk metal. Apparent thinning of the cross-section is accompanied with the failures of the specimens during uniaxial tensile testing, as shown in Figure 38 (a); the area of the built samples (2.512 ± 0.007 mm^2) reduced after the tensile tests to 0.582 ± 0.020 mm^2. The failure surfaces exhibited high ductility, which can be clearly observed at a higher magnification (Figure 38 (b)) from the dimple-like surface morphology along with the microscopic voids formation, growth, and eventual coalescence due to the large plastic deformation. The mechanical properties are summarized in Table 15, in which we listed the standard 0.2% offset yield stress. One aspect that should be emphasized is that DMLS is known to considerably reduce the difference between the yield point and the ultimate tensile strength [134]; DMLS is also known to

produce high-strength parts, as the grain growth is restricted due to the rapid cooling. Whereas the alteration of this strength ratio in our case is marginal. One possible explanation is the relatively large residual stresses induced during fabrication, especially by the lack of preheating of the building platform [146],[60] which acts as internal tensile strength encouraging the initiation of plastic deformation, and this also partially accounts for the low elastic Young's modulus. The low stiffness is also related to the isolated voids and cracks at the boundary between powder granule and between two unfused layers. The high UTS is probably due to the strengthening from the small grains. Due to the epaxial growth of the grain, the direction of load is parallel to the columnar grains, which contributes to the large elongation. Further microstructure and residual stress analyses should be conducted to provide a thorough explanation to the tensile behavior of these samples.

5. Examples

The experimental results obtained in this study demonstrate that binder inkjet printing of SS 316L outperforms DMLS printing of SS 316L and lost-wax micromolding of sterling silver in terms of resolution and fidelity to the CAD file; in addition, binder inkjet-printed SS 316L is UHV compatible, has thermal and electrical conductivities close to bulk values, and has a near-isotropic Young's modulus close to bulk values. In this section, two examples of 3-D printed, freeform, fine-featured metal structures part of compact systems are presented, i.e., a multi-electrode harmonized Kingdon ion trap, and MEMS corona discharge ionizer arrays.

5.1. Miniaturized advanced Kingdon ion trap

Mass spectrometers (MS) are used to quantitatively determine the composition of a sample by ionizing the sample and using electrical and/or magnetic fields to sort the ions based on their mass-to-charge ratio [147]. For over thirty years, researchers have actively pursued the development of compact MS systems to be able to do, anywhere in-situ, the chemical analysis currently only feasible in brick-and-mortar labs [148], [149]. A significant portion of this research effort has focused in developing miniaturized electrical mass filters, i.e., devices that sort out ions using electric fields; examples of these devices include quadrupoles [128], ion traps [150], and time-of-flight filters [151]. The fabrication of compact mass filters is inherently difficult because of the absolute tolerances required to achieve satisfactory performance (e.g., mass resolution) [152].

Besides precise electrode alignment, high-fidelity fabrication of complex shapes is essential to implement electrodes that can generate with great accuracy the electric fields needed for efficient species sorting. For example, the ideal quadrupole mass filter has hyperbolic rods; however, due to fabrication complexity, the great majority of miniaturized (and non-miniaturized) quadrupoles have circular rods, which introduces higher order fields, resulting in distortion of the peak shape, peak broadening (loss of resolution), and mass shifts [153]. Moreover, quadrupole electrode geometries compatible with standard batch microfabrication, e.g., square rods [26], greatly degrade the peak shape, further reducing the performance of the filter. Consequently, a typical non-miniaturized quadrupole has a mass resolution (ratio between the mass of the peak and its width) on the order of thousands or more, while a typical MEMS quadrupole has at least a mass resolution an order of magnitude smaller.

AM has recently been explored as a means to reach better performance in miniaturized mass filters by fabricating with high fidelity the correct electrode shapes for efficient species sorting; reported work includes linear ion traps [154], [155] and quadrupoles [156]. However, these devices are made in polymer and coated with a thin layer of metal, which creates problems such as outgassing, incompatibility with hard

baking, mechanical deflection, and lifetime; in addition, RF mass filters (e.g., quadrupoles, ion traps) could have issues with skin depth and heating of the metal layer caused by the driving signals.

The development of miniaturized MS instruments with greatly improved resolution would decisively help mass spectrometry become ubiquitous, as device portability would not be achieved at the expense of performance. Kingdon traps [157] are electrostatic mass filters based on a harmonic axial field that are capable of up to 140,000:1 mass resolution and high mass accuracy [158]. Cassinian ion trap mass analyzers are Kingdon traps, characterized by high mass resolution and high mass accuracy [159]; the state-of-art Cassinian trap, called Orbitrap Elite, was fabricated with the stringent refinement of the existing precision manufacturing techniques, featuring an outer barrel-like electrode of maximum radius equal to 10 cm and a central spindle-like electrode of maximum radius 5 cm [160], [161]. However, the Orbitrap cannot capture the ions created inside; therefore, it can only be used in conjunction with another trap (e.g., C-trap in [162]) or a pulsed ion source. The use of an additional radio frequency trap with a complex system of deflectors to inject the ions to the Orbitrap, as well as the use of a high-voltage pulsed power supply, significantly increases the energy consumption of the device, and greatly complicates its implementation as a portable device. In addition, the electrode shapes of a Cassinian trap are very complex; therefore, there is a clear need to simplify the manufacture process to fabricate electrodes with high mechanical accuracy and high-vacuum compatibility that generate the ideal electric fields for optimal performance of the mass analyzer.

It is possible to implement compact multi-electrode harmonized Kingdon traps that hold the ions created inside them and allow measuring their masses [159], [163]. Using modeling and simulations, our collaborators recently identified a novel multi-electrode harmonized Kingdon trap that has low sensitivity to distortions in geometry and/or misalignment of the electrodes [164] (Figure 39 (a), (b))); such a trap is an excellent candidate for AM because the shapes of the electrodes are intricate, smoothly varying, and finely detailed. The general form of the electric potential φ inside the trap is in the form of

$$\varphi(x,y,z) = c \left(z^2 - \frac{cx^2 + dy^2}{2}\right) + ln[((x+a)^2 + (y+b)^2)((x+a)^2 + (y-b)^2)] + ln[((x-a)^2 + (y+b)^2)((x-a)^2 + (y-b)^2)], \tag{5-1}$$

where z is the coordinate along the axis of the mass filter, and a, b, and c are constants; the combination of a quadrupole and logarithmic potential is beneficial for ion injection at stable voltages due to the difference in trapping motion mechanism [158]. A thorough explanation of the design is beyond the scope of this thesis; however, the following are the highlights of the design: (i) the shape of the matched outer and central electrodes are designed to follow the equipotential surface expressed as a combination of a quadrupole and a logarithmic potential, (ii) the outer electrode is split into halves to measure the differentially amplified image current; (iii) the geometry of the trap was optimized to improve the sensitivity and reduce higher
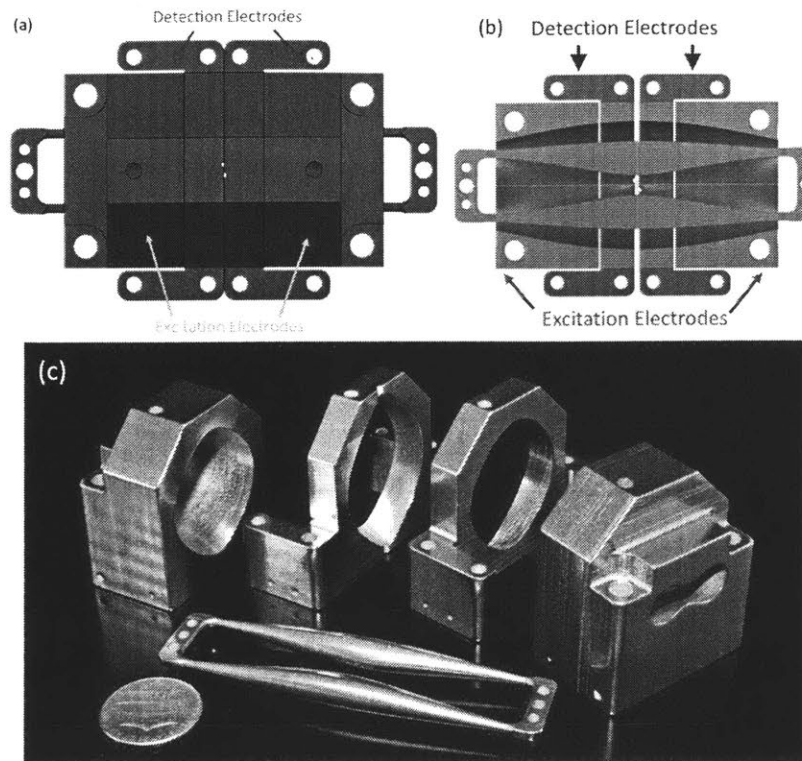
Figure 38 (a) Top view schematic of second order Kingdon trap; (b) cross section of the trap; (c) corresponding binder inkjet-printed SS 316L electrodes.

harmonics; (iv) the ion motion along the central axis is harmonic and the trajectory of trapped ions adopted in this design is the radial motion between the inner electrodes; (v) unlike the orbital trapped motion in the Orbitrap, the radial motion of the ions inside this advanced trap is one-dimensional, making possible to trap ions with almost no initial kinetic energy.

Based on the results of the characterization of the three AM technologies, the advanced Kingdon trap was fabricated with SS 316L via binder inkjet printing (Figure 39 (c)). To characterize the geometrical accuracy, the surface of each component was mapped using a Keyence VR3200 Wide-Area 3D Measurement System. The mapped surface profiles were compared with the CAD design; Figure 40 (a) shows the height deviation of the central electrode vs. CAD file values, while the height deviation of the central electrode scanned along the central axes of the arms of the electrode is shown in Figure 40 (b) and (c). The instrument used to measure the electrodes can only reliably measure a side angle smaller than 65°; this incapability leads to the larger deviations in some of the edges of the printed part in Figure 40 (a), and at the ends of the linear scans shown in Figure 40 (b) and (c). However, most of the height deviation field
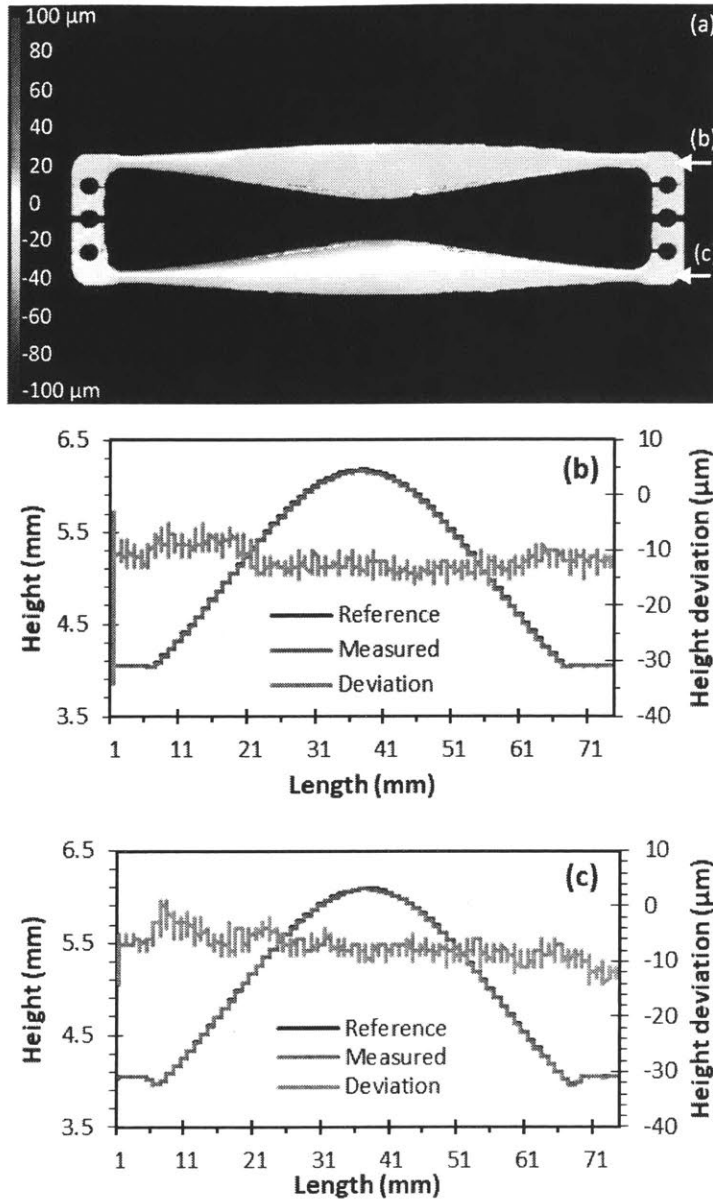
Figure 39 Height deviation of fabricated central electrode vs. CAD file values: (a) 3D mapping; (b) height deviation along a horizontal line lying on the central axis of the upper arm of the electrode; (c) height deviation along a horizontal line lying on the central axis of the lower arm of the electrode.

falls within 15 μm, consistent with the metrology of the resolution matrices used in this work. The upper bound for the deviation of about 1 slice, consistent with other AM methods [2].

5.2. MEMS corona discharge ionizer arrays

A corona discharge is an ionized gas discharge that occurs between a sharp electrode (corona electrode), typically a needle or a wire, and a blunt electrode (collector electrode) such as a plate or a cylinder with the high curvature of the corona electrode intensifying the local electric field. Once the local electric field is higher than a certain threshold start-up value, ionization is initiated and the tip(s) of the corona electrode are surrounded by a faint glow; from this point, as the applied bias voltage increases, the corona discharge becomes stronger with growing ionization zone, resulting in higher corona discharge current. If the applied bias voltage reaches the breakdown threshold, arcing between the corona electrode and the collector electrode takes place; this phenomenon is initiated by spark coronas across the electrodes at a very high voltage, leading to huge corona discharge current, and the possibility of damaging the electrodes [165], [166].

DC corona discharges can be operated in both positive and negative polarity, depending on whether the bias voltage on the corona electrode is higher or lower than the bias voltage on the collector electrode. If the bias voltage of the corona electrode is positive with respect to the collector electrode, a positive corona will occur; similarly, if the bias voltage of the corona electrode is negative with respect to the collector electrode, a negative corona will be generated. The work reported in this section was conducted on negative DC corona discharges. Negative coronas generally propagate by impact ionization of the gas molecules, caused by free electrons leaving the active zone; collision of the electrons transform neutral gas molecules into negative ions that exhibit a substantially reduced mobility, which is continually lessened as the ions travel to the collector electrode because the electric field decreases proportionately between the corona electrode and the collector electrode. The corona electrode also attracts positive ions, generating secondary emission from the electrode through ion bombardment, which help sustain the glow corona discharge. This also leads to the generation of new secondary electrons that travel outward with relatively high mobility (electrons are far more mobile than ions), causing an even, high space charge density across the gap between the corona electrode and the collector electrode. Thus, negative coronas generate a high population of negative ions with high charge density because an increasing proportion of the electrons escape attachment under the increasing electric field in the active zone, resulting in great excitation and dissociation of neutral molecules across the gap [165]. The mobility of ions in a negative corona is more vulnerable to the effect of temperature, causing a larger decrease in current than in the positive corona [167]. Negative corona discharge produces a higher ozone concentration due to the presence of a higher number of electrons.

Corona discharge ionizers have received interest as fast response, noiseless pumps without moving parts that can transport liquid [168] or gaseous media for applications such as air propulsion [169] and electronics cooling [168]. Given that electrical field enhancement is increased by scaling down the tip

69
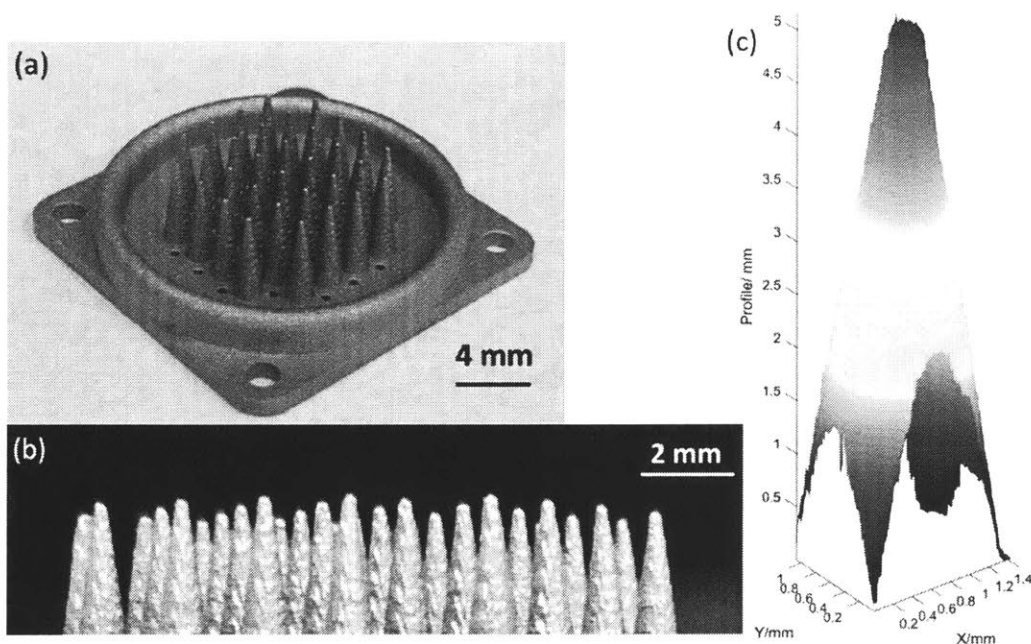
Figure 40 A binder inkjet-printed SS 316L planar array of 32 high aspect-ratio tips (a) with near-front view of the of the tips (b) close-up of the tips; (c) 3D profile of a typical tip characterized with Keyence scanning confocal microscope.
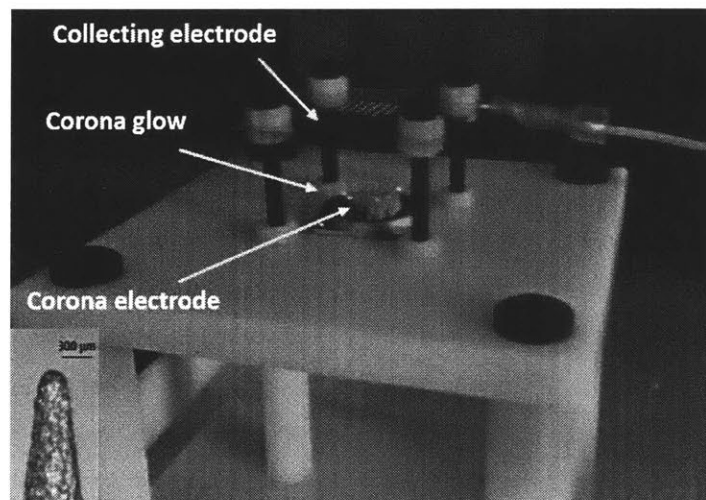
Figure 41 Steady-glow corona generating a visible purple haze around the high-curvature tips of the collector electrode. A close-up of one of the tips of the corona electrode is shown.

diameter and increasing its aspect-ratio, researchers have looked into developing MEMS corona discharge ionizers [170], [171]; these devices could have start-up voltages as small as 1.25 kV and tip currents as high

as 16 µA. However, the reported devices are unideal because the metallization is only ~20 µm thick and made of electroplated metals that are soft and not sputtering resistant (e.g., Cu), which could lead to reliability problems; also, the devices need to be assembled in a pick-and-place fashion to create from planar microfabricated components the three-dimensional structures needed for fluid pumping. Here, we report monolithic binder inkjet-printed SS 316L planar arrays of high-aspect-ratio conical tips and characterize them as corona discharge ionizers. The devices have a 1.7-mm diameter at the base, and have 5, 9 and 32 emitters respectively that are 5 mm tall, with 300 µm tip diameter at the top, and the tip-to-tip separations are 6mm, 4mm, 3mm, 2mm, respectively. A 32-tip emitter is shown in Figure 41, metrology done with Tabletop SEM TM3030 shows that the average diameter of the tip is 283.37 ± 6.49 µm, with Keyence scanning confocal microscope VK-X250 we get the average areal surface roughness as 4.627 ± 1.829 µm. An image of the corona discharge in steady glow state of one of these devices is shown in Figure 42.

Devices with different number of emitters were tested using as collector electrodes perforated metal grids 100 µm thick with 5.5 mm, 3.5 mm and 1.5 mm diameter apertures, centered relative to the tip of the emitters; the spacing between the edges of adjacent holes were equal among different collecting electrodes (0.5 mm). The collector electrode was grounded, and the tip array was biased at a negative voltage supplied by a 20 W, 1 mA high-voltage power supply (Gamma, Ormond Beach, FL, USA); the current was measured via the RS232C interface of the power supply and with a Keithley 485 picoammeter (Keithley Instruments,
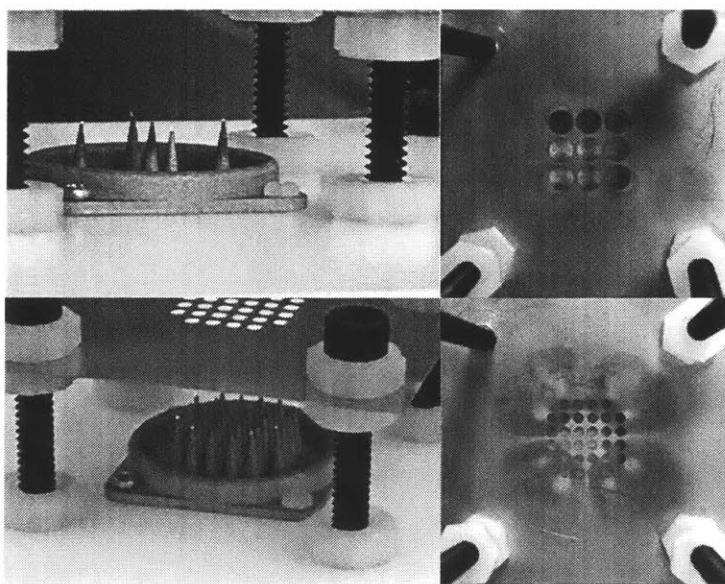
Figure 42 Evidence that support the fact that no corona discharge generation took place at the central tips due to electric field shielding: left hand-side pictures show arrays in operation, right hand-side pictures show the collector electrode after the experiments.

Table 16 Onset voltage of negative corona discharge generated by 5-emitter, 9-emitter, and 32-emitter devices at different electrodes separations

Device	Parameters		Values			
5-emitter	Gap spacing/mm		17.47	14.30	11.12	7.95
	Onset voltage/kV	Experimental	10.08	9.56	7.80	6.92
		$I/V - V$ curve	9.740	8.996	7.507	6.587
9-emitter	Gap spacing/mm		17.47	14.30	11.12	7.95
	Onset voltage/kV	Experimental	11.2	10.48	8.48	7.24
		$I/V - V$ curve	10.599	9.735	7.947	6.947
32-emitter	Gap spacing/mm		17.47	14.30	11.12	7.95
	Onset voltage/kV	Experimental	15	13.68	11.56	9.4
		$I/V - V$ curve	14.573	12.783	10.930.8	8.887

Cleveland, OH, USA) through a high-voltage 5 MW resistor. The separation between the corona electrode and the collecting electrode was controlled by stand-offs. The onset voltage (the minimum bias voltage required to generate a current larger than $1\mu A$) vs. separation is summarized in Table 16 –these values are for the array, not for each of the tips that make up the array. From images taken during the experiment and the collector electrode after the experiment (Figure 43), we concluded that the internal tips of the corona electrodes didn't generate any corona discharge as their onset voltage is larger than the bias voltages used in the experiments. This can be explained by the shielding effect in which the electrostatic field along the emitter's axis near the outer needles is higher than that for the central needles; the shielding effect is more pronounced with smaller tip separation (i.e., for devices with larger number of needles).

Corona current-vs.-bias voltage characteristics were collected for devices with 5, 9, and 32 needles at varying gap spacing (tip-to-collector electrode separation), shown in Figure 44. It is clear that the corona current decreases with the increase of gap spacing, which is caused by the decrease of the electric field on the tips. In addition, a smaller gap spacing can easily lead to arcing. Results of current-voltage measurements of devices with different number of emitters at same gap distance are shown in Figure 45. For needles with smaller tip-to-tip separation, the total corona current is significantly smaller at the same gap spacing; this is because the decrease of the tip-to-tip spacing leads to a decrease of the local electric field on the tips, which also increases the onset voltage. This reason can also explain the steeper slope of
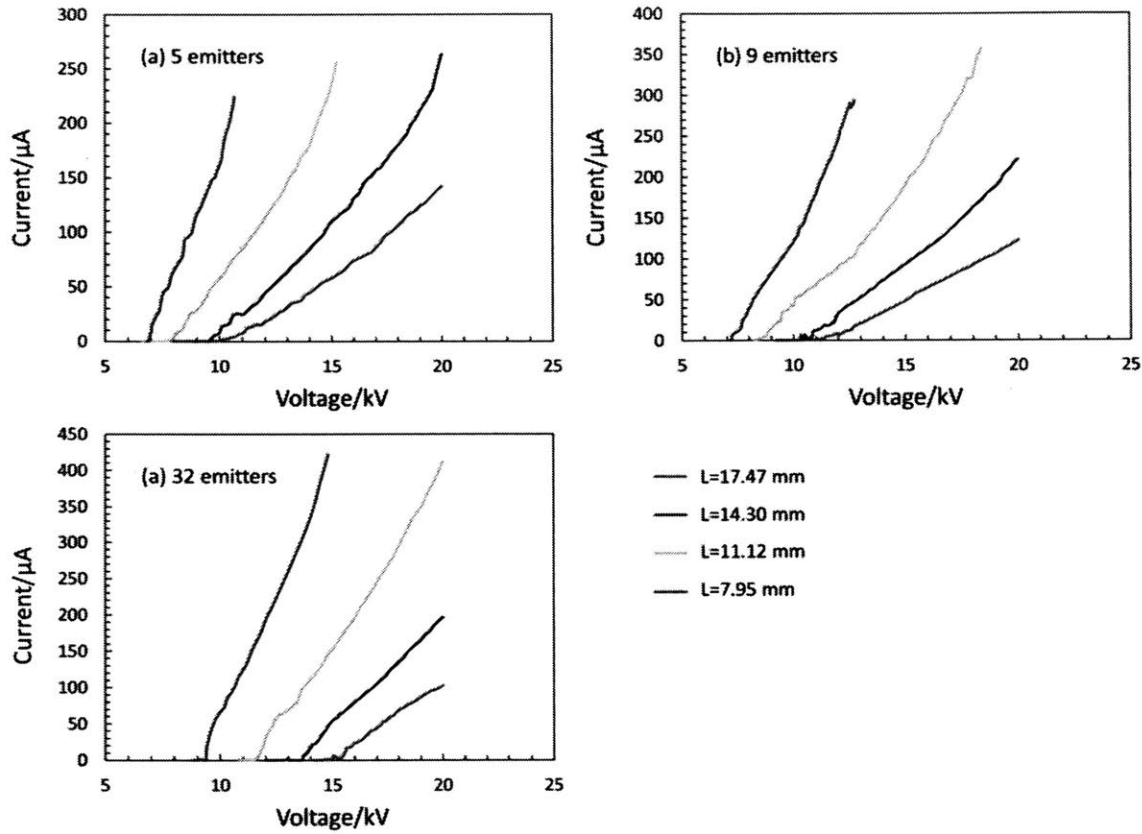
Figure 43 Current-voltage characteristics at different tip-to-collector separations for devices with 5 emitters (a), 9 emitters (b), and 32 emitters (c). A downward monotonic trend of current over gap spacing is present.

the current-voltage curve with increasing number of needles (for these devices, larger emitter array size is equivalent to smaller tip-to-tip separation). It was observed during the experiments that the corona appears first on the outermost electrodes and as the bias voltage gradually increases, corona discharge starts to appear on the inner needles.

Further, the voltage-current $(V - I)$ characteristic of a steady state corona discharge can be approximated by Townsend's discharge relation [172]

$$I = kV(V - V_0), \tag{5-2}$$

where I is the current, V is the applied voltage, V_0 is the onset voltage, and k is a constant which is a function of the geometric parameters such as radius of the corona source and the gap distance; k also depends on the properties of the interstitial gas which determines the mobility of ions. According to Eq.(5 2), I/V is linearly
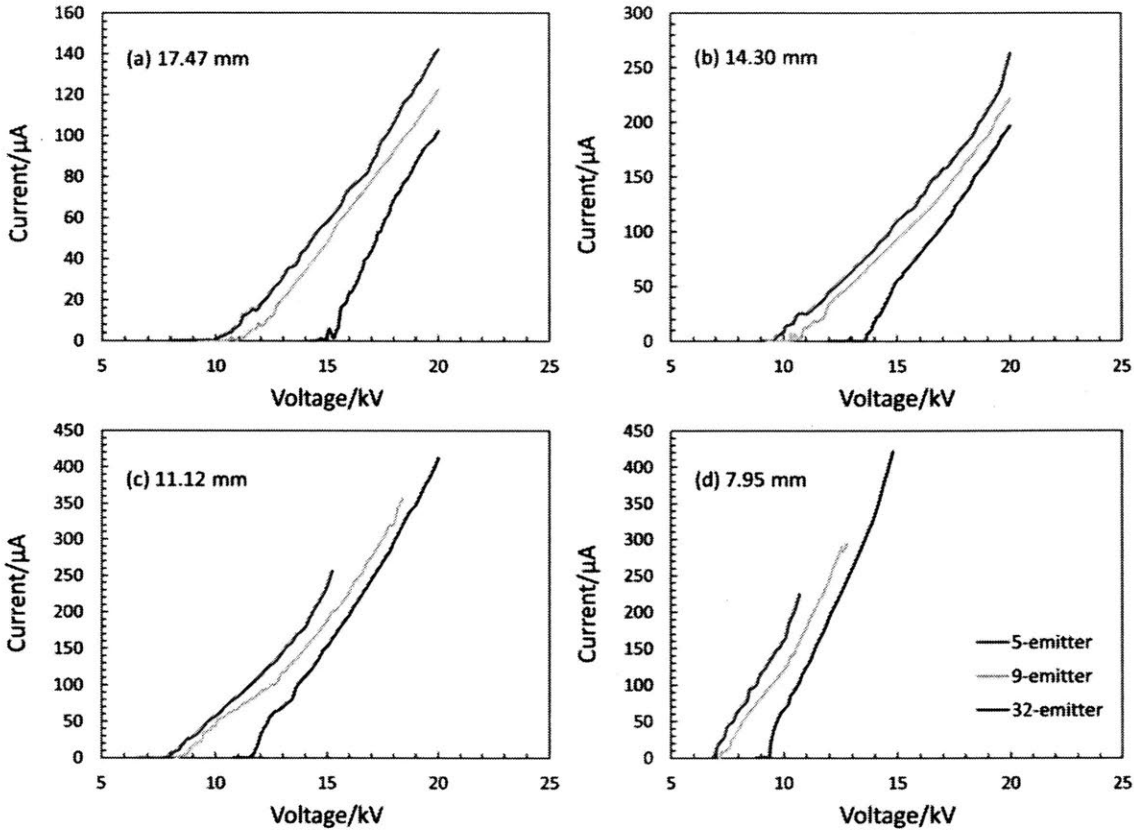
Figure 44 Current-voltage characteristics of devices with different number of emitters at gap distance of 17.47 mm (a), 14.30 mm (b), 11.12 mm (c), and 7.95 mm (d).

related to the applied voltage V, which is plotted in Figure 46 to show its validity in the scenario of multi-tip corona discharge. As observed from the plots, the relationship holds true for multi-emitter discharge even with shielding effects, while for smaller gaps, there are more fluctuations, but the curves still follow the linear fits.

The onset voltage V_0, as explained above, is determined experimentally observing the voltage at which currents jump from noise levels in nA to μA range. Townsend's discharge relationship expressed in Eq.(5-2) can also be used to obtain V_0 from the intercept of the linear fit in Figure 46, and the results are compiled in Table 16, which match well with those from experimental observations.
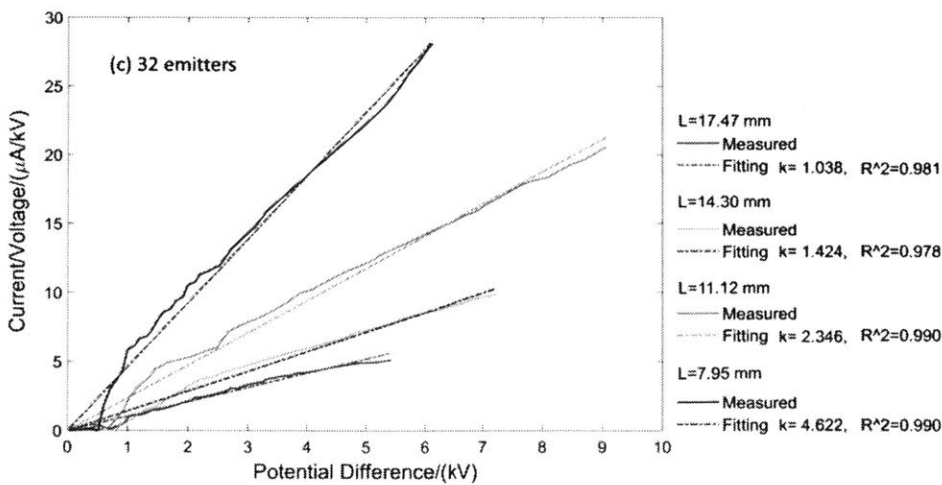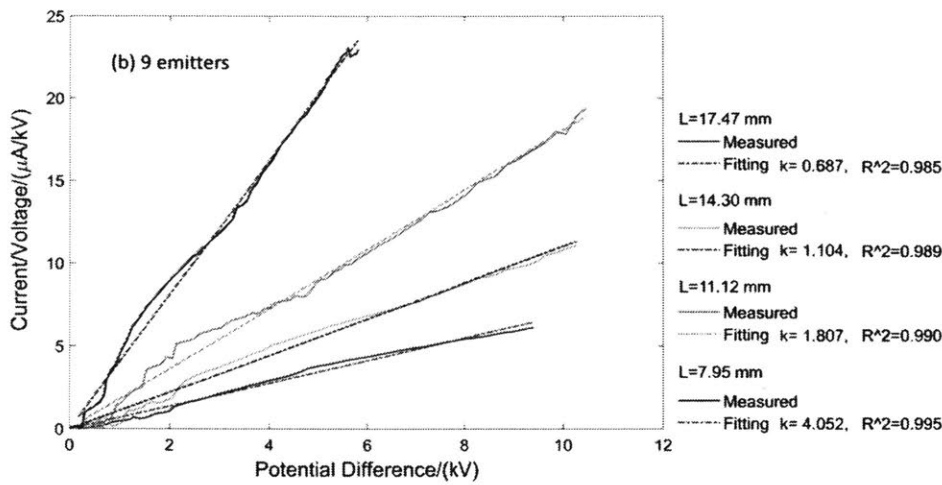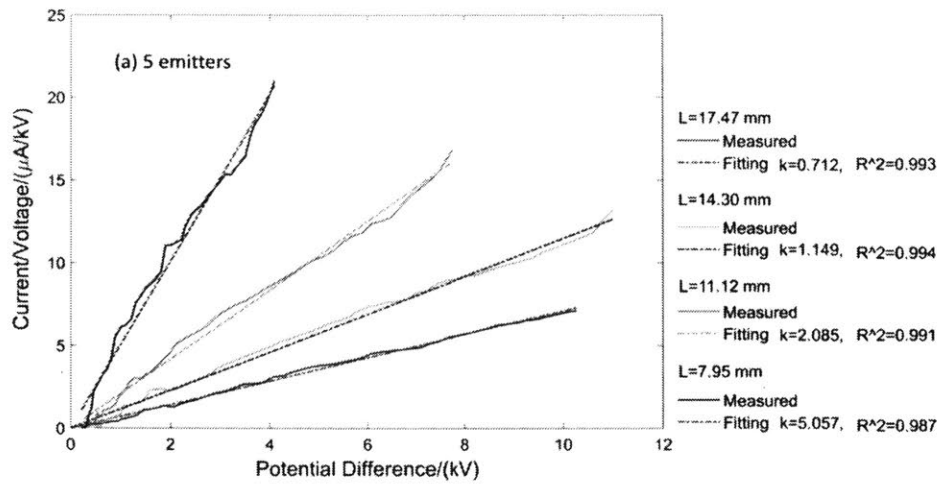
Figure 45 I/V as a function of V for device with (a) 5 emitters; (b) 9 emitters; (c) 32 emitters.

6. Conclusion

This study compares three metal additive manufacturing methods with associated feedstock, i.e., lost-wax casting of sterling silver using stereolithography-printed wax masters, binder inkjet printing of SS 316L, and DMSL printing of SS 316L, for the microfabrication of freeform, finely featured, mesoscaled metal structures part of compact systems. The data show that binder inkjet printing of SS 316L creates printed parts with high fidelity to the CAD file, having associated the smallest in-plane offset, out-of-plane offset, and eccentricity of nominally symmetric features, with minimum feature sizes around 300 μm; in addition, the data show that binder inkjet-printed SS 316L structures are UHV compatible, and have electrical resistance, thermal conductivity and elastic properties close to those of the bulk metal. 3D printed MEMS cantilevers were characterized to understand the surface morphology and defects of the imprints, and to estimate the mechanical properties of the material produced by different technologies. Two examples of 3-D printed, freeform, fine-featured metal mesoscaled structures were presented, i.e., MEMS corona discharge ionizer arrays, and compact, advanced Kingdon ion traps.

The results of this study suggest that is feasible to implement a wide range of binder inkjet-printed SS 316L devices including high-temperature microfluidics, vacuum devices, mass filters, ionizers, actuators, pumps, and vibration energy harvesters. Binder inkjet printing decouples the printing process (at room temperature) and the consolidation process (in inert atmosphere at high temperature), enabling independent optimization of the two processes to manufacture final parts with high dimensional accuracy. Binder inkjet printing of SS 316L is also capable of fabricating mesoscaled overhanging structures with well-defined geometries, which is highly beneficial for surface post-processing; polished smooth surfaces could be functionally relevant, e.g. increasing the fatigue life of cantilevers and other printed actuators.

7. Future Outlook

In terms of the characterization of the printed materials, an open question that remains is what causes the high density of the binder inkjet-printed parts. DMLS involves liquid phase sintering, which in general enhances densification. In liquid phase sintering, the powder constituent with lower melting temperature forms the liquid phase, which coexists with the solid phase of the high melting temperature constituents at the sintering temperature; the liquid will then flow along the interparticle channels to wet the particles due to capillarity. The capillary pull the solid particles together and induce particle rearrangement [173]; with continued heating, the solid phase dissolves into the liquid and the amount of liquid grows until it is saturated with the solid component. In addition, the liquid gives rapid mass transport at the sintering temperature and enhances densification. However, counter-intuitively, this study shows that binder inkjet printing outperforms DMLS in terms of porosity, i.e., a lower fraction of porosity and smaller pore size are obtained. A possible explanation is that the laser used to print in DMLS only heats up a small volume of powder at a time, which generated a short-lived small area of liquid phase, which hindered the densification of the DMLS material, resulting in high porosity. In addition, microstructure characterization of binder inkjet-printed and DMLS samples needs to be conducted, and comparison between printed bulk and printed fine feature could be an interesting direction to explore.

In terms of the applications presented, the advanced Kingdon trap needs to be experimentally validated; we are currently working with external collaborators to collect mass spectra data. Also, more research is needed to improve the performance of the MEMS corona discharge devices. The morphology of the array (spatial tip distribution) should be modified to counteract electric field shielding; in addition, the morphology of the tips needs to be studied to maximize per-emitter current emission for a given bias voltage; moreover, it should be explored ways to uniformly sharpen the tips to achieve dimensions smaller than the minimum feature size obtain with the printing method. Other directions of interest include studying the emission in the positive polarity and experimenting with varying the nature of the bias voltage (DC, pulse, or AC). Cross-validation between the finite element analysis and experimental results should be pursued. Finally, applications of the developed 3D printed MEMS corona discharge technology, such as electronic cooling and ionic wind pumping, should be explored.

References

[1]   D. I. Wimpenny, P. M. Pandey, L. Jyothish, and K. Editors, "Advances in 3D Printing & Additive Manufacturing Technologies," in *1st International Conference on 3D Materials Science*, 2012, pp. 19–24.

[2]   I. Gibson, D. W. Rosen, and B. Stucker, *Additive manufacturing technologies: 3D Printing, Rapid Prototyping, and Direct Digital Manufacturing*, 2nd ed. Springer, 2014.

[3]   M. Vaezi, H. Seitz, and S. Yang, "A review on 3D micro-additive manufacturing technologies," *International Journal of Advanced Manufacturing Technology*, vol. 67, no. 5–8. pp. 1721–1754, 2013.

[4]   "Additive Manufacturing, DMLS, 3D Metal Printing, i3D News." [Online]. Available: https://www.i3dmfg.com/i3d-news-press/. [Accessed: 11-Mar-2018].

[5]   S. Waheed *et al.*, "3D printed microfluidic devices: enablers and barriers," *Lab Chip*, vol. 16, no. 11, pp. 1993–2013, 2016.

[6]   H. Gong *et al.*, "High density 3D printed microfluidic valves, pumps, and multiplexers," *Lab Chip*, vol. 16, no. 13, pp. 2450–2458, 2016.

[7]   D. Olvera-Trejo and L. F. Velásquez-García, "Additively manufactured MEMS multiplexed coaxial electrospray sources for high-throughput, uniform generation of core–shell microparticles," *Lab Chip*, vol. 16, no. 21, pp. 4121–4132, 2016.

[8]   M. A. Skylar-Scott, S. Gunasekaran, and J. A. Lewis, "Laser-assisted direct ink writing of planar and 3D metal architectures," *Proc. Natl. Acad. Sci. U. S. A.*, vol. 113, no. 22, pp. 6137–6142, May 2016.

[9]   T. Takai, H. Nakao, F. Iwata, 11 K Matsuda, S. Takahashi, and K. Takamasu, "Three-dimensional microfabrication using local electrophoresis deposition and a laser trapping technique," vol. 22, no. 23, 2014.

[10]   J. Hu and M.-F. Yu, "Meniscus-confined three-dimensional electrodeposition for direct writing of wire bonds.," *Science*, vol. 329, no. 5989, pp. 313–6, Jul. 2010.

[11]   J. H. Yu, S. Y. Kim, and J. Hwang, "Effect of viscosity of silver nanoparticle suspension on conductive line patterned by electrohydrodynamic jet printing," *Appl. Phys. A*, vol. 89, no. 1, pp. 157–159, Aug. 2007.

[12]   V. Tasco *et al.*, "Three-dimensional nanohelices for chiral photonics," *Appl. Phys. A*, vol. 122, no.

4, p. 280, Apr. 2016.

[13]   Y. S. Kornbluth, R. H. Mathews, L. Parameswaran, L. M. Racz, and L. F. Velásquez-García, "Microsputterer with integrated ion-drag focusing for additive manufacturing of thin, narrow conductive lines," *J. Phys. D. Appl. Phys.*, vol. 51, no. 16, p. 165603, Apr. 2018.

[14]   L. Hirt, A. Reiser, R. Spolenak, and T. Zambelli, "Additive Manufacturing of Metal Structures at the Micrometer Scale," *Adv. Mater.*, vol. 29, no. 17, p. 1604211, May 2017.

[15]   T. A. Dow and R. O. Scattergood, "Mesoscale and Microscale Manufacturing Processes: Challenges for Materials, Fabrication and Metrology," in *American Society for Precision Engineering, 2003 Winter Topical Meeting - Volume 28*, 2003, pp. 14–19.

[16]   R. Gohdssi, *MEMS Material an Processes Hand book*, 1st ed. Springer, Boston, MA, 2010.

[17]   Y. M. Shin *et al.*, "Microfabrication of millimeter wave vacuum electron devices by two-step deep-etch x-ray lithography," *Appl. Phys. Lett.*, vol. 88, no. 9, p. 091916, Feb. 2006.

[18]   C. D. Joye *et al.*, "Microfabricated 233 GHz traveling wave amplifier," in *2016 IEEE International Vacuum Electronics Conference (IVEC)*, 2016, pp. 1–2.

[19]   M. Geear, R. R. A. Syms, S. Wright, and A. S. Holmes, "Monolithic MEMS quadrupole mass spectrometers by deep silicon etching," *J. Microelectromechanical Syst.*, vol. 14, no. 5, pp. 1156–1166, Oct. 2005.

[20]   J.-F. Dufault et al., "Fabrication and demonstration of planar microreactors for solar steam methane reforming," in *Technical digest PowerMEMS 2017, Kanazawa, Japan, November 14 - 17, 2017*.

[21]   E. R. Parker, M. P. Rao, K. L. Turner, C. D. Meinhart, and N. C. MacDonald, "Bulk Micromachined Titanium Microneedles," *J. Microelectromechanical Syst.*, vol. 16, no. 2, pp. 289–295, Apr. 2007.

[22]   E. Larrañeta, R. E. M. Lutton, A. D. Woolfson, and R. F. Donnelly, "Microneedle arrays as transdermal and intradermal drug delivery systems: Materials science, manufacture and commercial development," *Mater. Sci. Eng. R Reports*, vol. 104, no. 104, pp. 1–32, Jun. 2016.

[23]   Y. Zhang, L. Liu, Y. Chen, and J. Ouyang, "Characteristics of ionic wind in needle-to-ring corona discharge," *J. Electrostat.*, vol. 74, pp. 15–20, 2015.

[24]   A. Dompierre and L. G. Frechette, "A wafer-level process for bulk tungsten integration in MEMS vibration energy harvesters and inertial sensors," in *2017 19th International Conference on Solid-State Sensors, Actuators and Microsystems (TRANSDUCERS)*, 2017, pp. 2127–2130.

[25]   A. Srivastava, "Microfabricated Terahertz Vacuum Electron Devices: Technology, Capabilities and

Performance Overview," *Eur. J. Adv. Eng. Tech.*, vol. 2, no. 5, pp. 54–64, 2015.

[26] K. Cheung, L. F. Velásquez-García, and A. I. Akinwande, "Chip-Scale Quadrupole Mass Filters for Portable Mass Spectrometry," *J. Microelectromechanical Syst.*, vol. 19, no. 3, pp. 469–483, Jun. 2010.

[27] L. F. Velásquez-García, K. Cheung, and A. I. Akinwande, "An Application of 3-D MEMS Packaging: Out-of-Plane Quadrupole Mass Filters," *J. Microelectromechanical Syst.*, vol. 17, no. 6, pp. 1430–1438, Dec. 2008.

[28] C. Hauser, "Selective Laser Sintering of a Stainless Steel Powder, PhD Dissertation," University of Leeds, Leeds, UK, 2003.

[29] I. Tolosa, F. Garciandía, F. Zubiri, F. Zapirain, and A. Esnaola, "Study of mechanical properties of AISI 316 stainless steel processed by 'selective laser melting', following different manufacturing strategies," *Int. J. Adv. Manuf. Technol.*, vol. 51, no. 5–8, pp. 639–647, 2010.

[30] D. Gu, *Laser additive manufacturing of high-performance materials.* Springer, 2015.

[31] J. P. Kruth, L. Froyen, J. Van Vaerenbergh, P. Mercelis, M. Rombouts, and B. Lauwers, "Selective laser melting of iron-based powder," *J. Mater. Process. Technol.*, vol. 149, no. 1–3, pp. 616–622, Jun. 2004.

[32] Y. Zhong *et al.*, "Additive manufacturing of 316L stainless steel by electron beam melting for nuclear fusion applications," *J. Nucl. Mater.*, vol. 486, pp. 234–245, 2017.

[33] M. L. Griffith *et al.*, "Free form fabrication of metallic components using laser engineered net shaping (LENS)," in *Solid Freeform Fabrication Proceedings*, 1996, vol. 9, pp. 125–131.

[34] I. Gibson, D. Rosen, and B. Stucker, "Directed Energy Deposition Processes," in *Additive manufacturing technologies : 3D printing, rapid prototyping, and direct digital manufacturing*, 2015, pp. 245–268.

[35] B. E. Carroll, T. A. Palmer, and A. M. Beese, "Anisotropic tensile behavior of Ti–6Al–4V components fabricated with directed energy deposition additive manufacturing," *Acta Mater.*, vol. 87, pp. 309–320, 2015.

[36] B. Utela, D. Storti, R. Anderson, and M. Ganter, "A review of process development steps for new material systems in three dimensional printing (3DP)," *Journal of Manufacturing Processes*, vol. 10, no. 2. pp. 96–104, 2008.

[37] Y. Zhang *et al.*, "Additive Manufacturing of Metallic Materials: A Review," *J. Mater. Eng.*

Perform., no. Ref 32, pp. 1–13, 2017.

[38]   M. Prechtl, A. Otto, and M. Geiger, "Rapid Tooling by Laminated Object Manufacturing of Metal Foil," *Adv. Mater. Res.*, vol. 6–8, pp. 303–312, 2005.

[39]   R. J. Friel and R. A. Harris, "Ultrasonic Additive Manufacturing – A Hybrid Production Process for Novel Functional Products," *Procedia CIRP*, vol. 6, pp. 35–40, 2013.

[40]   "Standard Terminology for Additive Manufacturing -- General Principles -- Terminology." International Organization for Standardization, ISO/ASTM 52900:2015 (ASTM F2792), Geneva, Switzerland, pp. 1–19, 2015.

[41]   W. J. Sames, F. A. List, S. Pannala, R. R. Dehoff, and S. S. Babu, "The metallurgy and processing science of metal additive manufacturing," *Int. Mater. Rev.*, vol. 61, no. 5, pp. 315–360, 2016.

[42]   L. E. Murr *et al.*, "Metal Fabrication by Additive Manufacturing Using Laser and Electron Beam Melting Technologies," *J. Mater. Sci. Technol.*, vol. 28, no. 1, pp. 1–14, Jan. 2012.

[43]   W. E. Frazier, "Metal Additive Manufacturing: A Review," *J. Mater. Eng. Perform.*, vol. 23, no. 6, pp. 1917–1928, Jun. 2014.

[44]   "3D Printing - DM3D." [Online]. Available: http://www.dm3dtech.com/index.php?option=com_content&view=article&id=194&Itemid=817. [Accessed: 03-Sep-2017].

[45]   "Metal 3D Printers LENS Systems - Additive Manufacturing." [Online]. Available: https://www.optomec.com/3d-printed-metals/lens-printers/. [Accessed: 03-Sep-2017].

[46]   D. R. White, "Ultrasonic consolidation of aluminum tooling," *Adv. Mater. Process.*, vol. 161, no. 1, pp. 64–65, 2003.

[47]   P. F. Jacobs, *Rapid prototyping & manufacturing: fundamentals of stereolithography*. Society of Manufacturing Engineers, 1992.

[48]   S. H. Ko, "Chapter 18 - Advanced Inkjet Technology for 3D Micro-metal Structure Fabrication," *Micromanufacturing Eng. Technol.*, pp. 425–439, 2015.

[49]   R. Jianzhong, T. E. Sparks, and L. F. W. Zhiqiang Fan, Stroble Jacquelyn K., Panackal Ajay, "A Review of Layer Based Manufacturing Processes for Metals," in *Solid Freeform Fabrication Symposium, January 2006*, 2006.

[50]   M. Shellabear and O. Nyrhilä, "DMLS – Development History and State of the Art," in *LANE 2004 conferencee, Erlangen, Germany, Sept. 21-24*, 2004, pp. 1–12.

[51] EOS GmbH - Electro Optical Systems, "DirectMetal and DirectSteel materials for EOSINT M 250 Xtended," 2004. [Online]. Available: https://www.3axis.us/matetials/dmls/Direct Metal 20.pdf. [Accessed: 13-Apr-2018].

[52] J.-P. Kruth, G. Levy, F. Klocke, and T. H. C. Childs, "Consolidation phenomena in laser and powder-bed based layered manufacturing," *CIRP Ann.*, vol. 56, no. 2, pp. 730–759, Jan. 2007.

[53] J.-P. Kruth, B. Vandenbroucke, J. Van Vaerenbergh, and P. Mercelis, "Benchmarking of different SLS/SLM processes as Rapid Manufacturing techniques," in *Int. Conf. Polymers & Moulds Innovations (PMI), Gent, Belgium, April 20-23, paper 525*, 2005.

[54] J. -P. Kruth, P. Mercelis, J. Van Vaerenbergh, L. Froyen, and M. Rombouts, "Binding mechanisms in selective laser sintering and selective laser melting," *Rapid Prototyp. J.*, vol. 11, no. 1, pp. 26–36, Feb. 2005.

[55] D. Thomas, "The Development of Design Rules for Selective Laser Melting," PhD Dissertation, University of Wales, Cardiff, 2009.

[56] T. M. Mower and M. J. Long, "Mechanical behavior of additive manufactured, powder-bed laser-fused materials," *Mater. Sci. Eng. A*, vol. 651, pp. 198–213, Jan. 2016.

[57] W. E. Frazier, "Metal additive manufacturing: A review," *Journal of Materials Engineering and Performance*, vol. 23, no. 6. pp. 1917–1928, 2014.

[58] Wang L., "Study on the properties of parts fabricated by selective laser melting," PhD Dissertation, Huazhong University of Science and Technology, Wuhan, China, 2012.

[59] W. F. Hosford, "Freezing," in *Physical Metallurgy*, 2nd ed., CRC Press, Taylor & Francis Group, LLC, 2010, pp. 9–36.

[60] I. Yadroitsev, P. Krakhmalev, I. Yadroitsava, S. Johansson, and I. Smurov, "Energy input effect on morphology and microstructure of selective laser melting single track from metallic powder," *J. Mater. Process. Technol.*, vol. 213, no. 4, pp. 606–613, 2013.

[61] K. Abd-elghany, D. L. Bourell, and K. Abd-Elghany, "Property evaluation of 304L stainless steel fabricated by selective laser melting," *Rapid Prototyp. J.*, vol. 18, no. 3, pp. 420–428, 2012.

[62] A. Sachdeva, S. Singh, and V. S. Sharma, "Investigating surface roughness of parts produced by SLS process," *Int. J. Adv. Manuf. Technol.*, vol. 64, no. 9–12, pp. 1505–1516, Feb. 2013.

[63] L. E. Murr *et al.*, "Microstructures and properties of 17-4 PH stainless steel fabricated by selective laser melting," *J. Mater. Res. Technol.*, vol. 1, no. 3, pp. 167–177, 2012.

[64]   J. Jhabvala, E. Boillat, T. Antignac, and R. Glardon, "On the effect of scanning strategies in the selective laser melting process," *Virtual Phys. Prototyp.*, vol. 5, no. 2, pp. 99–109, 2010.

[65]   S. F. S. Shirazi *et al.*, "A review on powder-based additive manufacturing for tissue engineering: Selective laser sintering and inkjet 3D printing," *Science and Technology of Advanced Materials*, vol. 16, no. 3. pp. 1–20, 2015.

[66]   H. Gu, H. Gong, D. Pal, K. Rafi, T. Starr, and B. Stucker, "Influences of Energy Density on Porosity and Microstructure of Selective Laser Melted 17- 4PH Stainless Steel," in *Solid Freeform Fabrication Proceedings*, 2013, vol. 37, pp. 474–489.

[67]   L. B. Hunt, "The long history of lost wax casting," *Gold Bull.*, vol. 13, no. 2, pp. 63–79, Jun. 1980.

[68]   "The Lost Wax Casting Process." [Online]. Available: https://cantorfoundation.org/resources/the-lost-wax-casting-process/. [Accessed: 13-Mar-2018].

[69]   S. Corbel, O. Dufaud, and T. Roques-Carmes, "Chapter 6 Materials for Stereolithography," in *Stereolithography: Materials, Processes and Applications*, P. J. Bártolo, Ed. Springer US, 2011, pp. 141–159.

[70]   S. Kalpakjian and S. Schmid, *Manufacturing Processes for Engineering Materials*, 5th ed. Pearson education, 2008.

[71]   S. Montserrat, F. Roman, and P. Colomer, "Vitrification and dielectric relaxation during the isothermal curing of an epoxy-amine resin," *Polymer (Guildf).*, vol. 44, no. 1, pp. 101–114, Jan. 2002.

[72]   W. X. Zukas, "Torsional braid analysis of the aromatic amine cure of epoxy resins," *J. Appl. Polym. Sci.*, vol. 53, no. 4, pp. 429–440, Jul. 1994.

[73]   C. W. Hull, S. T. Spence, C. W. Lewis, W. B. Vinson, W. S. Freed, and D. R. Smalley, "Stereolithographic curl reduction," WO Patent, WO1989010801A1, Nov 16 1989.

[74]   S. Jayanthi, M. Keefe, and E. Gargiulo, "Studies in stereolithography: influence of process parameters on curl distortion in photopolymer models," in *Proceedings of the Solid Freeform Fabrication Symposium, 250–258, 1994, Solid Freeform Fabrication Symposium, Austin, Texas.*, 1994, pp. 250–258.

[75]   Laurel A. Hanesian, "Parameter optimization for curl distortion in building parts using 3-D laser stereolithography," Master thesis, New Jersey Institute of Technology, Newark, NJ, 1998.

[76]   T. H. Pang, "Stereolithography Epoxy Resins SL 5170 and SL 5180: Accuracy, Dimensional

Stability, and Mechanical Properties," in *5th Symposium, Solid freeform fabrication, Austin, TX,* 1994, pp. 204–224.

[77]   J. Eschl, T. Blumenstock, and P. Eyerer, "Comparison of the curing process of epoxy and acrylate resins for stereolithography by means of experimental investigations and FEM-Simulation," in *10th, Solid freeform fabrication symposium, Austin, TX,* 1999, pp. 453–460.

[78]   "Frequently Asked Questions | Formlabs." [Online]. Available: https://formlabs.com/support/faq/#Form-2. [Accessed: 13-Mar-2018].

[79]   M. Horáček, *Accuracy of investment castings,* vol. 5, no. 15. PAN – Katowice PL, 2005.

[80]   "Potential causes of casting defects." [Online]. Available: www.ransom-randolph.com. [Accessed: 18-Mar-2018].

[81]   P. K. D. V Yarlagadda and T. S. Hock, "Statistical analysis on accuracy of wax patterns used in investment casting process," in *Journal of Materials Processing Technology,* 2003, vol. 138, no. 1–3, pp. 75–81.

[82]   S. Taşcıoğlu, B. İnem, and N. Akar, "Conversion of an investment casting sprue wax to a pattern wax by the modification of its properties," *Mater. Des.,* vol. 25, no. 6, pp. 499–505, Sep. 2004.

[83]   H. P. Bhavsar and A. Kumar Kaviti, "Optimization of Wax Tank Parameter to Improve the Quality of Wax Pattern in Investment Casting," *Int. J. Eng. Res. Dev.,* vol. 8, no. 12, pp. 2278–67, 2013.

[84]   O. Bemblage and D. B. Karunakar, "A Study on the Blended Wax Patterns in Investment Casting Process," in *Proceedings of the World Congress on Engineering 2011,* vol. I, July 6.

[85]   G. Baumeister, R. Ruprecht, and J. Hausselt, "Replication of LIGA structures using microcasting," in *Microsystem Technologies,* 2004, vol. 10, no. 6–7, pp. 484–488.

[86]   B. Verlee, T. Dormal, and J. Lecomte-Beckers, "Density and porosity control of sintered 316L stainless steel parts produced by additive manufacturing," *Powder Metall.,* vol. 55, no. 4, pp. 260–267, Sep. 2012.

[87]   T. Do, P. Kwon, and C. Seop Shin, "Process development toward full-density stainless steel parts with binder jetting printing," *Int. J. Mach. Tools Manuf.,* pp. 1–11, 2017.

[88]   "Farsoon Technologies – Open for Industry." [Online]. Available: http://en.farsoon.com/solution_list02_detail/productId=38.html. [Accessed: 15-Mar-2018].

[89]   "Farsoon Technologies – Open for Industry." [Online]. Available: http://en.farsoon.com/solution_list02cl_detail/productId=47.html. [Accessed: 15-Mar-2018].

[90] "Plasticast with BANDUST." [Online]. Available: https://www.gesswein.com/p-11026-rr-plasticast-with-bandust-50-lb.aspx. [Accessed: 15-Mar-2018].

[91] "Investment Mixing & Burnout Instructions." [Online]. Available: https://www.ishor.com/investment-mixing-and-burnout-instructions. [Accessed: 18-Mar-2018].

[92] R. Carter, "Casting Investment Powder Performances - Ganoksin Jewelry Making Community." [Online]. Available: https://www.ganoksin.com/article/casting-investment-powder-performances/. [Accessed: 18-Mar-2018].

[93] D. Ott, "Properties and testing of investment," in *Proc. of the Santa Fe Symposium on Jewelry Manufacturing Technology 1988, Met-Chem Research Inc.*, 1989, pp. 47–62.

[94] Ralph Carter, "Effects of Water Quality and Temperature," in *Proc. of the Santa Fe Symposium on Jewelry Manufacturing Technology 2000, Met-Chem Research*, 2000, pp. 1–27.

[95] "B9 Emerald Casting Resin - Redresins." [Online]. Available: https://www.redresins.com/resin/129-b9-emerald-casting-resin.html. [Accessed: 15-Mar-2018].

[96] "DIGITAL METAL ® DM P2500." [Online]. Available: https://digitalmetal.tech/wp-content/uploads/2018/02/Digital-Metal-DM-P2500_feb2018_2168HOG_screen.pdf. [Accessed: 19-Mar-2018].

[97] "Additive Manufacturing of Small and Complex Parts Rapid 3D Printing," 2018. [Online]. Available: https://digitalmetal.tech/wp-content/uploads/2018/02/Additive-manufacturing_feb2018_-2169HOG_screen.pdf. [Accessed: 19-Mar-2018].

[98] B. Edenhofer, J. W. Bouwman, and D. H. Herring, "Vacuum Heat Processing," in *Steel Heat Treatment Equipment and Process Design*, 2006, pp. 240–274.

[99] P. Beiss, "Control of Protective Atmospheres during Sintering," in *Proceedings Euro PM*, 2000, pp. 147–157.

[100] "QV-Active_PR-image.jpg (2935×1654)." [Online]. Available: https://www.mitutoyo.com/wp-content/uploads/2016/05/QV-Active_PR-image.jpg. [Accessed: 15-Mar-2018].

[101] "CNC Vision Measuring System QUICK VISION." [Online]. Available: http://www.measuringsolutions.com/wp-content/uploads/2013/02/1953_QuickVision.pdf. [Accessed: 15-Mar-2018].

[102] L. Reimer, *Scanning Electron Microscopy — Physics of Image Formation and Microanalysis*, 3rd ed. Springer, 1998.

[103] D. R. Tobergte and S. Curtis, *Scanning Electron Microscopy and X-Ray Microanalysis*, 3rd ed. Springer, 2007.

[104] E. Kim, E. Iroaga, and B. Murmann, "Brief Introduction to Scanning Electron Microscopy (SEM)," *Http://Cfamm.Ucr.Edu/Documents/Sem-Intro.Pdf*, 2004. [Online]. Available: https://cfamm.ucr.edu/documents/sem-intro.pdf. [Accessed: 20-Mar-2018].

[105] "Tabletop Microscope (Benchtop SEM) | Tabletop Microscope TM3030 : Hitachi High-Technologies GLOBAL." [Online]. Available: https://www.hitachi-hightech.com/global/tm/products/tm3030/. [Accessed: 22-Mar-2018].

[106] N. S. Claxton, T. J. Fellers, and M. W. Davidson, "Laser scanning confocal microscopy," *Department of Optical Microscopy and Digital Imaging, Florida State University, Tallahassee*, 2006. [Online]. Available: https://pdfs.semanticscholar.org/53d4/dc9a18be32f8f0196138e7f85fe4387376c7.pdf. [Accessed: 22-Mar-2018].

[107] S. W. Paddock and K. W. Eliceiri, "Chapter 2 Laser Scanning Confocal Microscopy: History, Applications, and Related Optical Sectioning Techniques," in *Confocal Microscopy: Methods and Protocols, Methods in Molecular Biology*, vol. 1075, 2014, pp. 9–47.

[108] Stephen W Paddock, "Principles and Practices of Laser Scanning Confocal Microscopy," *Mol. Biotechnol.*, vol. 16, pp. 127–149, 2000.

[109] S. Inoué, "Foundations of confocal scanned imaging in light microscopy," in *Handbook of Biological Confocal Microscopy: Third Edition*, Boston, MA: Springer US, 2006, pp. 1–19.

[110] R. Oldenbourg, T. H. Terada, and S. Inoue, "Image sharpness and contrast transfer in coherent confocal microscopy," *J. Microsc.*, vol. 172, no. 3, pp. 1–39, 1993.

[111] I. T. Young, R. Zagers, L. J. Van Vliet, J. Mullikin, F. Boddeke, and H. Netten, "Depth-of-Focus in Microscopy," in *SCIA '93, Proc. 8th Scandinavian Conference on Image Analysis, Tromso, Norway*, 1993, pp. 493–498.

[112] L. Vozár and W. Hohenauer, "Flash method of measuring the thermal diffusivity. A review," *High Temp. Press.*, vol. 35/36, no. 3, pp. 253–264, 2003.

[113] W. J. Parker, R. J. Jenkins, C. P. Butler, and G. L. Abbott, "Flash Method of Determining Thermal Diffusivity, Heat Capacity, and Thermal Conductivity," *J. Appl. Phys.*, vol. 32, no. 9, pp. 1679–1684, Sep. 1961.

[114] R. E. Taylor, J. Gembarovic, and K. D. Maglic, "Thermal Diffusivity by the Laser Flash Technique," in *Characterization of Materials*, Hoboken, NJ, USA: John Wiley & Sons, Inc., 2002, pp. 1–10.

[115] L. F. A. Sample *et al.*, "Which Method is the Best Suited to my Particular Sample ?" [Online]. Available: https://www.netzsch-thermal-analysis.com/us/landing-pages/which-method-is-the-best-suited-to-my-particular-sample/. [Accessed: 19-Mar-2018].

[116] D. I. of M. Research, "LFA - Laser Flash Apparatus," 2015. [Online]. Available: https://dcyd0ggl1hia3.cloudfront.net/media/thermal-analysis/brochures/LFA_457_MicroFlash_en_web.pdf?1488186739&Policy=eyJTdGF0ZW1lbnQ iOlt7IlJlc291cmNlIjoiaHR0cHM6XC9cL2RjeWQwZ2dsMWhpYTMuY2xvdWRmcm9udC5uZX RcL21lZGlhXC90aGVybWFsLWFuYWx5c2lzXC9icm9jaHVyZXNcL. [Accessed: 19-Mar-2018].

[117] D. Cigoy, "Accurate Low-Resistance Measurements Start with Identifying Sources of Error," 2010. [Online]. Available: http://studylib.net/doc/18307427/accurate-low-resistance-measurements-start-with-identifying.

[118] B. Nuckolls, "Practical Low Resistance Measurements," *The AeroElectric Connection.* 2004.

[119] P. A. Redhead, "Recommended practices for measuring and reporting outgassing data," *J. Vac. Sci. Technol. A Vacuum, Surfaces, Film.*, vol. 20, no. 33, pp. 1667–21601, 2002.

[120] R. R. L. Archer Thomas J. and M. I. of T. D. of M. Engineering., *An introduction to the mechanics of solids.* New York : McGraw-Hill ; [S.l.] : Primis Custom Pub., c1999., 1999.

[121] T. J. Lu, "Young ' s modulus measurement of thin-film materials using micro-cantilevers," *J. Micromech.Microeng.*, vol. 16, pp. 1926–1934, 2006.

[122] "Low Speed Precision Cutting Machine - IsoMet™ | Buehler." [Online]. Available: https://www.buehler.com/isoMet-low-speed-cutter.php. [Accessed: 26-Mar-2018].

[123] A. Johnson, D. Fisher, and G. Vander Voort, "Solutions for Materials Preparation, Testing and Analysis." [Online]. Available: https://www.buehler.com/China/solutions/technotes/Vol_3_Issue_6.pdf. [Accessed: 26-Mar-2018].

[124] "Mounting application guide." [Online]. Available: https://www.buehler.com/Brochures/English/Mounting/FN01522_Mounting_Guide.pdf.

[125] "EcoMet™ /AutoMet™ Grinder-Polisher System." [Online]. Available: http://www.agarscientific.com/media/import/EcoMet-AutoMet.pdf.

[126] Buehler, *A Guide to Materials Preparation & Analysis*, 2nd ed. Lake Bluff, 2007.

[127] Höganäs, "Sintered Iron-Based Materials," in *Design and Mechanical Properties - Höganäs Handbook for Sintered Components*, 2015, pp. 45–90.

[128] M. Geear, R. R. A. Syms, S. Wright, and A. S. Holmes, "Monolithic MEMS quadrupole mass spectrometers by deep silicon etching," *J. Microelectromechanical Syst.*, vol. 14, no. 5, pp. 1156–1166, Oct. 2005.

[129] K. Jousten, *Handbook of vacuum technology, 2nd ed.* Weinheim, Germany : Wiley-VCH, 2016.

[130] N. V. Lavrik, M. J. Sepaniak, and P. G. Datskos, "Cantilever transducers as a platform for chemical and biological sensors," *Rev. Sci. Instrum.*, vol. 75, no. 7, pp. 2229–2253, 2004.

[131] H. U. Rahman, K. Y. Chan, and R. Ramer, "Cantilever beam designs for RF MEMS switches," *J. Micromechanics Microengineering*, vol. 20, no. 7, p. 075042, Jul. 2010.

[132] R. Elfrink *et al.*, "Vibration energy harvesting with aluminum nitride-based piezoelectric devices," *J. Micromechanics Microengineering*, vol. 19, no. 9, p. 094005, 2009.

[133] A. H. Nickel, D. M. Barnett, and F. B. Prinz, "Thermal stresses and deposition patterns in layered manufacturing," *Mater. Sci. Eng. A*, vol. 317, no. 1–2, pp. 59–64, Oct. 2001.

[134] L. Hitzler, J. Hirsch, B. Heine, M. Merkel, W. Hall, and A. Öchsner, "On the Anisotropic Mechanical Properties of Selective Laser-Melted Stainless Steel," *Materials (Basel).*, vol. 10, no. 10, p. 1136, Sep. 2017.

[135] P. Zhang, J. Liu, and A. C. To, "Role of anisotropic properties on topology optimization of additive manufactured load bearing structures," *Scr. Mater.*, vol. 135, pp. 148–152, 2017.

[136] T. Niendorf, F. Brenne, and M. Schaper, "Lattice structures manufactured by SLM: On the effect of geometrical dimensions on microstructure evolution during processing," *Metall. Mater. Trans. B Process Metall. Mater. Process. Sci.*, vol. 45, no. 4, pp. 1181–1185, 2014.

[137] E. Lam and M. A. Schmidt, "Characterizing metal nanoparticle films: A methodology using surface micromachining by direct printing," in *Solid- State Sens., Actuators, Microsyst. Workshop Tech. Dig.*, 2012, pp. 433–436.

[138] Eung Seok Park, Yenhao Chen, Tsu-Jae King Liu, and V. Subramanian, "Inkjet-printed micro-electro-mechanical switches," in *2011 International Electron Devices Meeting*, 2011, p. 29.2.1-29.2.4.

[139] P. Mercelis and J. Kruth, "Residual stresses in selective laser sintering and selective laser melting,"

Rapid Prototyp. J., vol. 12, no. 5, pp. 254–265, 2006.

[140] "Geometrical product specifications (GPS) -- Surface texture: Areal -- Part 2: Terms, definitions and surface texture parameters, ISO 25178-2:2012." .

[141] E. Yasa, O. Poyraz, E. U. Solakoglu, G. Akbulut, and S. Oren, "A Study on the Stair Stepping Effect in Direct Metal Laser Sintering of a Nickel-based Superalloy," *Procedia CIRP*, vol. 45, no. Supplement C, pp. 175–178, 2016.

[142] R. M. German, *Poweder Metallurgy Science*, 2nd ed. Princeton, New Jersey, USA: Metal Powder Industries Federation, 1994.

[143] G. F. Vander Voort, Ed., *ASM Handbook Volume 9: Metallography and microstructures*. ASM International, Ohio, USA, 2004.

[144] A. Rabbani, S. Jamshidi, and S. Salehi, "An automated simple algorithm for realistic pore network extraction from micro-tomography images," *J. Pet. Sci. Eng.*, vol. 123, pp. 164–171, Nov. 2014.

[145] "AK   Steel   316/316L   Stainless   Steel."   [Online].   Available: http://www.aksteel.com/pdf/markets_products/stainless/austenitic/316_3161_data_bulletin.pdf. [Accessed: 28-Sep-2017].

[146] A. A. and A. D. L. Sabina Luisa Campanelli, Nicola Contuzzi, "Capabilities and Performances of the Selective Laser Melting Process," in *New Trends in Technologies: Devices, Computer, Communication and Industrial Systems*, M. J. Er, Ed. Intech, 2010, pp. 233–252.

[147] J. H. Gross, *Mass Spectrometry: A Textbook*. Berlin, Germany: Springer-Verlag, 2006.

[148] R. R. A. Syms and S. Wright, "MEMS mass spectrometers: the next wave of miniaturization," *J. Micromechanics Microengineering*, vol. 26, no. 2, p. 023001, Feb. 2016.

[149] Z. Ouyang and R. G. Cooks, "Miniature Mass Spectrometers," *Annu. Rev. Anal. Chem.*, vol. 2, no. 1, pp. 187–214, Jul. 2009.

[150] A. Chaudhary, F. van Amerom, and R. T. Short, "Development of Microfabricated Cylindrical Ion Trap Mass Spectrometer Arrays," *J. Microelectromechanical Syst.*, vol. 18, no. 2, pp. 442–448, Apr. 2009.

[151] and T. J. C. R. J. Cotter, C. Fancher, "Miniaturized time-of-flight mass spectrometer for peptide and oligonucleotide analysis," *J. Mass Spectrom.*, vol. 34, no. 12, pp. 1368–1372, 1999.

[152] W. Xu, W. J. Chappell, R. G. Cooks, and Z. Ouyang, "Characterization of electrode surface roughness and its impact on ion trap mass analysis," *J. Mass Spectrom.*, vol. 44, no. 3, pp. 353–360,

Mar. 2009.

[153] J. R. G. and S. Taylor, "Prediction of quadrupole mass filter performance for hyperbolic and circular cross section electrodes," *Rapid Commun. Mass Spectrom.*, vol. 14, no. 18, pp. 1669–1673, 2000.

[154] M. Fico, M. Yu, Z. Ouyang, R. G. Cooks, and W. J. Chappell, "Miniaturization and geometry optimization of a polymer-based rectilinear ion trap," *Anal. Chem.*, vol. 79, no. 21, pp. 8076–8082, 2007.

[155] B. Brkić, S. Giannoukos, N. France, R. Murcott, F. Siviero, and S. Taylor, "Optimized DLP linear ion trap for a portable non-scanning mass spectrometer," *Int. J. Mass Spectrom.*, vol. 369, pp. 30–35, 2014.

[156] S. T. Boris Brkić, Neil France, Adam T.Clare, Chris J.Sutcliffe, Paul R.Chalker, "Development of Quadrupole Mass Spectrometers Using Rapid Prototyping Technology," *J. Am. Soc. Mass Spectrom.*, vol. 20, no. 7, pp. 1359–1365, Jul. 2009.

[157] K. H. Kingdon, "A Method for the Neutralization of Electron Space Charge by Positive Ionization at Very Low Gas Pressures," *Phys. Rev.*, vol. 21, no. 4, pp. 408–418, Apr. 1923.

[158] C. Köster, "Twin Trap or Hyphenation of a 3D Paul-and a Cassinian Ion Trap," *J. Am. Soc. Mass Spectrom*, vol. 26, pp. 390–396, 2015.

[159] C. Köster, "The concept of electrostatic non-orbital harmonic ion trapping," *Int. J. Mass Spectrom.*, vol. 287, pp. 114–118, 2009.

[160] A. Michalski *et al.*, "Ultra High Resolution Linear Ion Trap Orbitrap Mass Spectrometer (Orbitrap Elite) Facilitates Top Down LC MS/MS and Versatile Peptide Fragmentation Modes," *Mol. Cell. Proteomics*, vol. 11, no. 3, p. O111.013698, 2012.

[161] R. A. Zubarev and A. Makarov, "Orbitrap Mass Spectrometry," *Anal. Chem.*, vol. 85, no. 11, pp. 5288–5296, Jun. 2013.

[162] S. Eliuk and A. Makarov, "Evolution of Orbitrap Mass Spectrometry Instrumentation," *Annu. Rev. Anal. Chem.*, vol. 8, no. 1, pp. 61–80, 2015.

[163] Y. K. Golikov, N. K. Krasnovam, K. V. Soloviev, and D. V. Nikitin, "Integrable electrostatic ion traps," *Appl. Phys.*, vol. 5, pp. 50–57, 2006.

[164] Eugene (Evgeny) Nikolaev, G. Vladimirov, Y. Kostyukevich, O. Kharybin, and L. F. Velásquez-García, "Initial Characterization of 3D-printed HighResolution Low Weight and Low Power Consuming Fourier transform Mass Spectrometer Based on Cassinian Ion Trap," in *65th ASMS*

Conference on Mass Spectrometry and Applied Topics, 2017.

[165] M. Goldman, A. Goldman, and R. S. Sigmond, "The corona discharge, its properties and specific uses," *Pure Appl. Chem.*, vol. 57, no. 9, pp. 1353–1362, 1985.

[166] E. Nasser, *Fundamentals of gaseous ionization and plasma electronics*. Wiley-Interscience, New York, 1971.

[167] E. N. Wang *et al.*, "Micromachined Jets for Liquid Impingement Cooling of VLSI Chips," *J. Microelectromechanical Syst.*, vol. 13, no. 5, pp. 833–842, Oct. 2004.

[168] O. M. Stuetzer, "Ion drag pumps," *J. Appl. Phys.*, vol. 31, no. 1, pp. 136–146, 1960.

[169] E. A. C. and P. S. Moller, "Ion-Neutral Propulsion in Atmospheric Media," *AIAA J.*, vol. 5, pp. 1768–1773, 1967.

[170] A. Ongkodjojo Ong, "Electrohydrodynamic Microfabricated Ionic Wind Pumps for Thermal Management Applications," PhD Dissertation, Case Western Reserve University, Ohio, US, 2013.

[171] P. Ferrer and M. P. Tchonang, "Miniaturization of electrostatic ion engines by ionization and acceleration coupling," *J. Phys. D. Appl. Phys.*, vol. 44, no. 33, p. 335204, Aug. 2011.

[172] J. S. E. Townsend, *Electricity in gases*. Oxford, Clarendon Press, 1915.

[173] S. Magalhaes, "Surface composition and microstructure control during pressureless forming and sintering of ferrous powder metallurgy materials," PhD. Dissertation, Chalmers University and Technology, G¨oteborg, Sweden, 2003.

[174] G. Baumeister, J. Hauelt, S. Rath, and R. Ruprecht, "Microcasting," in *Microengineering of Metals and Ceramics: Part II: Special Replication Techniques, Automation and Properties*, D. Löhe and J. Haußelt, Eds. Wiley-VCH Verlag GmbH, 2008, pp. 357–393.

[175] "JUNCTION3D - U.S. Reseller for the Solus 3D Printer." [Online]. Available: http://www.junction3d.com/. [Accessed: 15-Apr-2018].

[176] "6-bit 3D laser scanning confocal microscope: VK-X250/X150/X120 series." [Online]. Available: http://www.ccmr.cornell.edu/wp-content/uploads/sites/2/2015/11/Keyence_VK-X250-Brochure.pdf. [Accessed: 22-Mar-2018].

[177] Keithley, *Low Level Measurements Handbook -- Precision DC Current, Voltage, and Resistance Measurements*, 7th ed. .

[178] "A Guide to Low Resistance Measurement," 2014. [Online]. Available: https://www.scribd.com/document/69170046/Cropico-Guide-to-Low-Resistance-Measurement.

[179] "Keysight   34420A   NanoVolt/Micro-Ohm   Meter."   [Online].   Available:
        https://literature.cdn.keysight.com/litweb/pdf/5968-0161EN.pdf?id=1000070096:epsg:dow.
        [Accessed: 20-Mar-2018].

[180] "Stainless Steel - Grade 316L - Properties, Fabrication and Applications (UNS S31603)." [Online].
        Available: https://www.azom.com/article.aspx?ArticleID=2382. [Accessed: 13-Sep-2017].

[181] "Sterling Silver, Cold Drawn then Annealed at 700°C (1290°F)." [Online]. Available:
        http://www.matweb.com/search/DataSheet.aspx?MatGUID=b87eb22d8c0a4662967a1f1756f8cdae
        &ckck=1. [Accessed: 13-Sep-2017].